Universität der Bundeswehr München
Fakultät für Luft- und Raumfahrttechnik
Institut für Thermodynamik

Numerical Simulation of Infrared Radiation from Aircraft Engine Exhaust Plumes

Alexander Sventitskiy

Vollständiger Abdruck der von der Fakultät für Luft- und Raumfahrttechnik der Universität der Bundeswehr München zur Erlangung des akademischen Grades eines

Doktor-Ingenieures (Dr.-Ing.)

genehmigten Dissertation

Vorsitzender: Prof. Dr.-Ing. habil. Markus Klein
1. Berichterstatter: Prof. Dr.-Ing. Christian Mundt
2. Berichterstatter: HDR Dr. Anouar Soufiani

Die Dissertation wurde am 22.03.2017 bei der Universität der Bundeswehr München eingereicht und durch die Fakultät für Luft- und Raumfahrttechnik am 01.09.2017 angenommen.
Die mündliche Prüfung fand am 09.10.2017 statt.

Acknowledgements

I wish to express my gratitude to my mentor, Prof. Dr. Christian Mundt. I am grateful for his finding time to reply to my questions, for being so kind as to show personal interest in my research and for giving of his valuable advice regarding the topic of my research.

I am happy to acknowledge Dr. Anouar Soufiani who kindly agreed to review my work and provided a valuable critique.

My special thanks to my family for being a constant source of motivation and inspiration.

And lastly, my grateful thanks to all colleagues who put their faith in me and provided me with a precious support.

Abstract

The present work deals with numerical modeling of radiative heat transfer in absorbing, emitting, and anisotropically scattering media. The emphasis is placed on simulations of infrared radiation from aircraft engine exhaust plumes. The study considers methods for the solution of the radiative transfer equation and for spectral modeling of radiation. A review of the present-day literature on plume thermal emission is given. Radiative transfer equation solution methods, such as the ray tracing method, the discrete ordinates method, and the most modern finite volume method, are considered. With respect to the spectral simulation of high-temperature gases, state-of-the-art narrow-band approaches are overviewed, namely statistical narrow-band models and the correlated-k method. The most commonly applied technique in prediction of radiation signatures is based on a one-dimensional radiation calculation performed independently along each line-of-sight through the plume using a statistical narrow-band model. It is, however, well known that the statistical narrow-band models are incompatible with scattering by particles. Additionally, when scattering occurs, the radiation transport becomes three-dimensional. This situation is treated in practice by making various approximations to the full radiative transfer equation. A new infrared signature predictive technique is therefore proposed in the present research. The new approach overcomes the incompatibility of transmissivity-based band models with scattering and it can readily be applied to three-dimensional scattering problems. In this approach, the finite volume method is assumed to be used for the calculation of the radiation intensity field within the plume's medium. In order to ensure an accurate modeling of gas mixture spectral behaviour, the narrow-band correlated-k model is coupled with the finite volume method. The finite volume solver implemented in this work is applied to the discretized radiative transfer equation in the primitive variable form and uses a marching technique that is consistent with the hyperbolic nature of the equation of transfer. The step scheme, which is unconditionally bounded and positive, is used as the spatial differencing scheme. Solutions for radiative heat flux and its divergence in three-dimensional enclosures containing participating media agree well with those available in the literature, thereby demonstrating the validity of the finite volume solver. A large number of calculations of directional infrared emissions from a realistic turbofan engine plume are carried out. A computer code named JERAD developed within the framework of the current work is employed. A comprehensive analysis of the calculation results is conducted to show that the proposed approach is capable of accurately predicting infrared signatures from absorbing-emitting-scattering jet exhausts.

Kurzfassung

Die vorliegende Arbeit befasst sich mit der numerischen Modellierung des Strahlungswärmeübergangs in absorbierenden, emittierenden und anisotropen Streumedien. Der Themenschwerpunkt liegt insbesondere auf der Simulation der Infrarotstrahlung von Flugzeugabgasstrahlen. Die Untersuchungen berücksichtigen Methoden zur Lösung der Strahlungstransportgleichung sowie der spektralen Modellierung der Strahlung. Eine Zusammenfassung der gegenwärtigen Literatur, über thermische Emissionen von Abgasstrahlen, wird einleitend gegeben. Transportgleichungslösungsverfahren für die Strahlung wie das Ray-Tracing Verfahren, das Diskrete-Ordinaten-Verfahren und das modernere Finite-Volumen-Verfahren werden dabei betrachtet. Hinsichtlich der spektralen Simulation von Hochtemperaturgasen werden modernste Schmalbandenansätze, wie die statistische Schmalbandenmodelle und die Correlated-k Methode diskutiert. Die am häufigsten angewandte Technik zur Vorhersage von Strahlungssignaturen basiert auf einer eindimensionalen Strahlungsberechnung, die entlang jeder einzelnen Sichtlinie durch den Abgasstrahl mit einem statistischen Schmalbandenmodell unabhängig durchgeführt wird. Es ist jedoch bekannt, dass die statistische Schmalbandenmodelle nicht mit der Teilchenstreuung kompatibel sind. Darüber hinaus wird der Strahlungstransport beim Auftreten einer Streuung dreidimensional. In der Praxis wird dieser Sachverhalt durch verschiedene Näherungen der vollständigen Strahlungstransportgleichung behandelt. Infolgedessen wird in der gegenwärtigen Forschung eine neue Infrarotsignatur-Vorhersagetechnik vorgeschlagen. Der neue Ansatz behebt die Inkompatibilität der transmissionsbasierten Bandenmodelle in Bezug auf die Streuung und kann gleichermaßen bequem auf dreidimensionale Streuungsprobleme angewendet werden. Für die Berechnung des Strahlungs-Intensitätsfeldes im Abgasstrahlmedium wurde das Finite-Volumen-Verfahren herangezogen. Um eine genaue Modellierung des spektralen Gasgemisch-Verhaltens zu gewährleisten, wird das schmalbandige Correlated-k Modell mit dem Finite-Volumen-Verfahren gekoppelt. Der in dieser Arbeit implementierte Finite-Volumen-Löser wird auf die diskretisierte Strahlungstransportgleichung, in ihrer primitiven variablen Form, angesetzt und dabei ein Fortschrittsverfahren verwendet, das mit dem hyperbolischen Charakter der Transportgleichung übereinstimmt. Das Step-Schema, das bedingungslos beschränkt und positiv ist, wird als räumliches Differenzierungsschema verwendet. In abgegrenzten dreidimensionalen Räumen, die die beteiligten Medien enthalten, stimmen die Lösungen für den Strahlungswärmefluss und dessen Divergenz gut mit den in der Literatur vorhandenen Daten überein, wodurch die Gültigkeit des Finite-Volumen-Lösers demonstriert wird. Zahlreiche Berechnungen zur

gerichteten Infrarotstrahlung werden anhand eines realen Turbofan-Triebwerkabgasstrahls durchgeführt. Dafür wird ein im Rahmen dieser Arbeit entwickelter Rechencode namens JERAD eingesetzt. Um zu zeigen, dass der vorgeschlagene Ansatz in der Lage ist, Infrarotsignaturen von Absorptionsemissionsstreuungs-Strahlabgasen genau vorherzusagen, wird eine umfassende Analyse der Berechnungsergebnisse durchgeführt.

Contents

List of Figures

List of Tables

List of Symbols

Latin Symbols

A	[	m^2, cm^2	]	area
a	[	μm	]	particle radius
a	[	$cm^2\,sr$	]	coefficient in the discretization equation of transfer
b	[	$(W\,cm^2)/m^2$	]	source term in the discretization equation of transfer
c	[	m/s	]	speed of light
d_j	[	m	]	jet (nozzle exit) diameter
E	[	J	]	radiation energy
$\vec{e}$	[	–	]	coordinate direction unit vector
f_v	[	–	]	particle volume fraction
$f(k)$	[	cm	]	k-distribution
G	[	W/m^2	]	incident radiation
g	[	–	]	cumulative k-distribution
H	[	–	]	Heaviside step function
I	[	$W/(m^2\,sr)$	]	radiance
J	[	W/sr	]	radiant intensity
k	[	–	]	absorptive index
k	[	cm^{-1}	]	absorption coefficient variable in k-distribution
$\bar{k}$	[	$cm^{-1}\,atm^{-1}$	]	ratio of mean line strength to mean line spacing
L	[	m	]	length
l	[	cm	]	gaseous column length
M	[	–	]	number of cells, or number of slabs, or number of species
N	[	–	]	number of control angles, or number of quadrature points, or number of spectral lines within $\Delta\eta$
N_{nb}	[	–	]	number of narrow bands
n	[	–	]	refractive index
$\vec{n}$	[	–	]	unit surface normal
p	[	atm	]	pressure

q_r	[	$\mathrm{W/m^2}$	]	radiative heat flux
$\vec{q}_r$	[	$\mathrm{W/m^2}$	]	radiative heat flux vector
$S, \bar{S}$	[	$\mathrm{cm^{-2}\,atm^{-1}}$	]	line strength, mean line strength within $\Delta\eta$
S	[	$\mathrm{W/(m^2\,sr)}$	]	radiative source function
S_r	[	$\mathrm{W/m^3}$	]	radiative heat source
s	[	cm	]	geometric path length (coordinate along ray)
$\vec{s}$	[	–	]	unit vector into a given direction (ray direction vector)
$\mathbf{s}$	[	sr	]	control solid angle size indicative vector
T	[	K	]	temperature
t	[	s	]	time
u	[	$\mathrm{J/m^3}$	]	radiation energy density
u	[	cm atm	]	optical path
v	[	–	]	scaling function for absorption coefficient
$\overline{W}$	[	$\mathrm{cm^{-1}}$	]	mean equivalent black-line width
x	[	–	]	mole fraction, or particle size parameter
x, y, z	[	m	]	Cartesian coordinates

Greek Symbols

α	[	–	]	model constant in Eq. (6.2)
$\bar{\beta}$	[	–	]	line overlapping parameter
β	[	$\mathrm{cm^{-1}}$	]	extinction coefficient
$\gamma, \bar{\gamma}$	[	$\mathrm{cm^{-1}}$	]	half-width at half-maximum, mean half-width at half-maximum within $\Delta\eta$
Δs	[	cm	]	slab length
ΔV	[	$\mathrm{cm^3}$	]	control volume
$\Delta\eta$	[	$\mathrm{cm^{-1}}$	]	wavenumber interval
$\Delta\Omega$	[	sr	]	control solid angle
δ	[	–	]	Dirac delta function
$\bar{\delta}, \bar{\delta}'$	[	$\mathrm{cm^{-1}}$	]	mean line spacing within $\Delta\eta$, effective mean line spacing
ϵ	[	–	]	emissivity
ζ_1, ζ_2	[	m	]	object plane coordinates
η	[	$\mathrm{cm^{-1}}$	]	wavenumber
Θ	[	–	]	scattering angle
θ	[	–	]	zenith angle, or aspect angle
κ	[	$\mathrm{cm^{-1}}$	]	absorption coefficient
λ	[	μm	]	wavelength

μ	[	–	]	cosine of scattering angle
ξ	[	–	]	mixture fraction
σ_s	[	cm^{-1}	]	scattering coefficient
τ	[	–	]	transmissivity
Φ	[	–	]	scattering phase function
φ	[	–	]	azimuth angle, or roll angle
$\underline{\phi}$	[	–	]	state variable vector $\underline{\phi} = (p, T, \underline{x})$
χ_s	[	–	]	scale factor for line-of-sight discretization
ψ	[	–	]	weighting factor in Eq. (2.12)
Ω	[	sr	]	solid angle
ω	[	–	]	quadrature weight

Subscripts

0	boundary value, or reference value
b	blackbody value
D, L, V	Doppler, Lorentz, Voigt
E, W, N, S, B, T	east, west, north, south, bottom, and top neighbours of P
e, w, n, s, b, t	east, west, north, south, bottom, and top control volume faces
f	face value
g	gas, or at a given cumulative k-distribution value
i, k	dummy counters
j	jet, or dummy counter
max	maximum value
min	minimum value
mix	multicomponent gas mixture
nb	control volume neighbour index
P	control volume
p	particle
s	at a given point along path s
uf	upstream face value
w	wall value
x, y, z	in a given coordinate direction
η	at a given wavenumber, or per unit wavenumber
θ, φ	in a given angular direction
λ	at a given wavelength, or per unit wavelength

Superscripts

$'$, $''$	dummy variables
$\bar{}$	average value
$\tilde{}$	normalized value
$+$, $-$	boundaries of control angle into a given direction
$*$	characteristic scale
l, l'	angular directions
n	iteration index

Acronyms and Abbreviations

1D	one-dimensional
2D	two-dimensional
3D	three-dimensional
ADF	absorption distribution function
API	application programming interface
CFD	computational fluid dynamics
CGA	Curtis-Godson approximation
CK	correlated-k
CKFG	correlated-k fictitious gas
CKG	correlated-k gray
DG	discontinuous Galerkin
DOM	discrete ordinates method
DTM	discrete transfer method
FEM	finite element method
FSK	full-spectrum k-distribution
FVM	finite volume method
HRS	high resolution scheme
HWHM	half-width at half-maximum
IDW	inverse distance weighting
IR	infrared
ISA	International Standard Atmosphere
LBL	line-by-line
LOS	line-of-sight

LTE	local thermodynamic equilibrium
MC	Monte Carlo
MOC	method of characteristics
MTO	maximum take-off
PDF	probability density function
RANS	Reynolds-averaged Navier-Stokes
RT	ray tracing
RTE	radiative transfer equation
SLG	single line group
SLW	spectral line-based weighted-sum-of-gray-gases
SNB	statistical narrow-band
SNBCK	statistical narrow-band correlated-k
SNBFG	statistical narrow-band fictitious gas
SNBG	statistical narrow-band gray
SRCS	Spectral Radiation Calculation Software
UV	ultraviolet
WLA	weak line approximation
WSGG	weighted-sum-of-gray-gases

Chapter 1

Introduction

Radiation originating from aerospace vehicles is of utmost importance for their designers. Thermal emissions, particularly those at infrared (IR) wavelengths, provide the basis for rocket detection and tracking. Spectral, temporal, and spatial distributions of IR radiation from rocket-powered vehicles are required for the design and optimization of sensors for various defense-related missions [1]. Anti-aircraft systems employ IR detectors and heat seeking missiles. Consequently, analysis of IR signatures passively emitted by aircraft is an important aspect of stealth technology [2].

The IR signature of an aerospace vehicle arises from multiple sources such as hot parts and skin emissions, reflected sunshine, skyshine, and earthshine emissions, and engine exhaust plume radiation [3]. The plume is a significant contributor to the total aircraft IR signature. Its length is several times greater than the aircraft's length, and so the plume radiation is visible from a wider range of aspect angles. Aircraft and countermeasure engineers rely upon the knowledge of plume radiation properties, be it for guidance and control or for detection [1, 4].

Accurate numerical modeling of IR radiation from plumes is therefore of prime importance for purposes such as long-range sensing; target detection, tracking, and lock-on; estimation of IR signature levels of aircraft, etc. Numerical simulations are also preferable to experimental measurements, for instance, to study the effects of passive countermeasures that can be undertaken to reduce the plume IR signature.

1.1 Background and Motivation

The accepted technique applied to predict IR emissions from plumes is based on the use of statistical narrow-band (SNB) models [5, 6]. In particular, some of the IR signature prediction codes, such as NIRATAM [7], SIGGE [8], CRIRA [9], and MIRA [10], use this approach despite its obvious shortcomings.

The most serious disadvantages of utilising the SNB models are the necessity of model parameter adjustments and the incompatibility with scattering by droplets and particles [11] (this is also true for the treatment of nongray walls). The latter is inherent to the SNB models and it cannot be eliminated, with the exception of the use of statistical Monte Carlo (MC) methods [12].

Indeed, if the plume's medium is purely gaseous, conventional band models (like SNB) can be directly applied to model gas IR properties when integrating the radiative transfer equation (RTE) along lines-of-sight (LOS) through the plume. When scattering occurs, the mean-transmissivity-based IR band model formalism fails [11]. Consequently this means that, in practical SNB calculations, all spectral correlation terms associated with scattering are simply approximated by uncorrelated products of corresponding mean quantities. As an example, for the mean product of spectral radiance and transmissivity one obtains $\overline{I_\lambda \tau_\lambda} = \bar{I}_\lambda \bar{\tau}_\lambda$, which is a crude approximation.

Liu et al. [13] suggested a method to alleviate the difficulty of the SNB model scattering incompatibility. The method is based on splitting the radiation intensity into nonscattered and scattered parts and solving the RTE using a ray tracing (RT) technique and discrete ordinates method (DOM). For example, this approach was used by Pautrizel et al. [14] to compute IR signatures of alumina loaded rocket exhaust plumes. Nevertheless, the model is approximate because there is no closed form for the spectral correlation between the gas absorption coefficient and scattered intensity.

In scattering media the radiative transport becomes three-dimensional. This imposes additional difficulties on the ways of modeling thermal radiation in scattering problems. In order to overcome these difficulties, various approximations have been introduced, e.g. the two-flux and six-flux scattering models [15–18] (see also Section 1.2).

Another approach assumes the medium to be optically thin with respect to scattering. This permits the use of a simple pseudo-gas model for particles, i.e. when the particle absorption coefficient is additive to that of gas. Such an approach was employed for alumina particles of two-phase plumes in the work [19] (discussed in Section 1.2). However, with the exception of soot, the gas and particle emissivities are not additive, and so the pseudo-gas model fails at large optical depths [11].

Dombrovsky et al. [20–22] developed the so-called combined two-step computational methods for radiative transfer in anisotropically scattering media. In these methods, the computational procedure is split into two solution steps. The first step is intended for the radiative source function evaluation. The second step is employed for the RTE solution with the source function values calculated from the first step.

The basic principle of the combined methods is to use the transport approximation for scattering phase function. In the transport approximation, which is a special case of the Dirac-delta approximation [23], the phase function is replaced by a sum of the isotropic component and the term describing the forward-scattering peak [22]. This yields a form of the RTE in which the forward scattering energy is treated as transmitted with an effective ("transport") scattering coefficient used. To obtain the incident radiation term

entering the source function, in the first solution step, the direction-integrated RTE based on the diffusion approximation is solved, e.g. by means of finite element method (FEM) [20]. To obtain the intensities, in the second step, the "transport" RTE is solved by the use of an arbitrary solution method such as the RT technique [20] or the MC method [21].

The treatment of the RTE in the presence of scattering remains one-dimensional, regardless of the approximation utilized (pseudo-gas, two-flux, or six-flux). It is obvious that the scattering problem is not treated rigorously. The errors introduced into computations by using these approximations are very difficult to ascertain [11].

Similarly, the combined two-step methods by Dombrovsky, because of their approximate nature, can lead to significant errors [21]. These methods are more applicable to problems where hemispherical radiative characteristics are of interest [21, 22]. In such problems, the transport approximation, which is likely to be the dominant source of errors in the combined methods, is a reasonable approach.

It is claimed in the work [24] that the solution of the RTE in the presence of scattering by particles is an impossible problem to solve without using approximate methods. This is believed to be an overstatement. Cai et al. [25] stated that the treatment of scattering with existing approximate methods is limited. They suggested a finite volume based model for simulations of IR emissions from particle-loaded liquid and solid rocket motor plumes. This work is the first attempt to solve the scattering problem for exhaust plumes without using additional approximations, to the author's best knowledge.

In order to take advantage of the finite volume method (FVM) (employed in the work [25]), the appropriate gas absorption coefficients are required. Which gas radiative property model is utilized to obtain the absorption coefficients is a question of great importance. Nevertheless, the model used in [25] was inaccurate since, to handle each narrow band over the spectrum, the mean absorption coefficients were assumed. This approach (called the gray-band approximation) is physically wrong because it ignores the fine structure of spectral lines within the narrow band. The use of a gray-band approximation can result in erroneous predictions of thermal signatures from plumes, as will be shown further in the present work.

To summarize, there is a lack of methods for prediction of directional radiation from absorbing, emitting, and scattering volumes at high temperature, such as exhaust plumes, that are 1) capable of treating radiative scattering by particles without any approximations, 2) coupled with spectral models that can readily be incorporated into scattering models, and 3) suitable for accurate narrow-band calculations.

1.2 Review of Earlier Work

A significant body of research has already been carried out into plume radiation. Nelson [17, 18] investigated the influence of particulates on the IR signature from liquid and solid rocket motor exhausts. In the work [17], the scattering effect of Al_2O_3 particles was studied using the pseudo-gas, two-flux, and six-flux models, whilst, in the work [18], the influence of radiation scattering by Al_2O_3 and carbon particles on IR emission from plumes of various motors was investigated. It was found that the IR signatures from plumes containing carbon particles are sensitive to the amount of carbon present, but insensitive to the carbon particle size. The IR signatures from plumes containing Al_2O_3 particles are sensitive to both the particle size and the amount present. Similar results were obtained in the work by Nelson and Tucker [26] for turbojet and ramjet plumes containing B_2O_3 particles.

The effect of phase transitions of Al_2O_3 particles on radiation characteristics of solid-propellant motor exhausts was studied by Plastinin et al. [27]. Computational results showed that the Al_2O_3 crystallization kinetics has a major impact on the predicted jet exhaust radiation.

Mahulikar et al. [28] as well as Rao and Mahulikar [29] modeled IR radiation emitted by aircraft plume and received by a ground-based IR detector. They also compared plume IR signature with rear fuselage and tailpipe IR emissions. It was found that most plume IR radiation received by the detector is absorbed by the intervening atmosphere and, in the nonafterburning mode, it is prominent only in the $4.15-4.20$ μm band. Moreover, it was demonstrated that in the nonafterburning mode the IR signature from the plume is much lower than that from the tailpipe and rear fuselage, especially with the use of $8-12$ μm band IR detectors.

Devir et al. [30] and Avital et al. [31] conducted experimental measurements of IR radiation associated with an underexpanded plume generated by a small solid-propellant rocket motor. Based on computational fluid dynamics (CFD) results, IR spectra and IR images of the plume were also calculated. The IR radiation characteristics of the numerically simulated exhaust plume and the experimentally derived plume were found to be broadly similar.

In the work [24], an axisymmetric nonisobaric supersonic jet mixing with the atmosphere was considered as a model for plume. The gas-dynamic structure of the plume, chemical kinetics, afterburning phenomenon, and two-phase flow features were considered in detail. The mechanisms of plume emissions in different spectral ranges including visible and ultraviolet (UV) were analysed. It was demonstrated that plume spectra are extremely sensitive to altitude changes. It was also found that the plume radiation in the visible and nearest UV regions, despite the less significant contribution to the total plume radiant intensity, can be pronounced in particular bands.

Another important work on modeling of radiation from solid and liquid-propellant motor plumes was carried out by Plastinin et al. [19]. An approach based on the assumption of nonequilibrium phase transitions of Al_2O_3 particles, nonequilibrium radiation of the

OH molecule in the UV spectral region, and soot oxidation in the plume was discussed in the paper. Simulations of radiation showed that soot oxidation becomes critical at lower altitudes. Additionally, nonequilibrium kinetics of OH population in the radiation model could result in approximately two orders of magnitude higher level of OH UV radiation when compared with an equilibrium model. The model for soot radiation in liquid-propellant motor plumes was considered in [32] and the model for the OH radiation was verified in [33] (through measured radiance image data and non-imaged spectral intensity data for Atlas missiles).

Modeling of the radiation from the exhaust plume of an Atlas II rocket was performed in the paper [34]. Although soot oxidation did not feature in this research, the plume flow field was numerically simulated more accurately than in [33]. In the work [33], the multi-nozzle plume of an Atlas missile was calculated using an assumption of a single equivalent nozzle, whilst in [34] a three-dimensional (3D) CFD simulation of the multi-nozzle plume was carried out. The reason was that the simplifying assumption of a single equivalent nozzle is not adequate to resolve a multi-nozzle plume structure [35].

MC simulation methods for plume emission predictions were used by Surzhikov [36–38]. The MC simulation algorithm was presented in detail in [36]. Comparative analysis of several numerical algorithms based on the line-by-line (LBL) method applied to MC calculations was performed in the paper [37]. In the work [38], results of IR signature calculations from particle-loaded single and multiple jets were presented, as well as the results of a solution of the problem of sunlight scattering by plumes.

Shuai et al. [39] applied the backward MC method to the prediction of the IR radiation characteristics of a high-temperature exhaust plume with particles. They compared the calculation results obtained using the backward MC method with those using the conventional (forward) MC method. The backward MC method was shown to be superior to the forward method with respect to computational efficiency.

Baek and Kim [40] applied the FVM to investigate a radiative heating of a rocket base plane due to the plume radiation and searchlight emission which is caused by photons emitted from the inside of nozzle and then scattered by the plume medium toward the base plane. To illustrate the applicability of the FVM, a parametric study involving the effects of changing various parameters, such as plume cone angle, scattering albedo, optical radius, nozzle exit temperature and scattering phase function (forward, isotropic and backward), was carried out. A simplified model of the exhaust plume assuming a uniform temperature distribution was used. Also, for simplicity, the radiative properties of the plume were assumed to be gray.

A number of efforts are known from the open literature that have been made to methodically study the IR characteristics of plumes from aircraft engines with emphasis on the IR radiation suppression and tailoring. Specifically, a mixed flow turbofan was analysed by Decher who used a simple modeling technique to study influences of the nozzle aspect ratio and the engine cycle parameters on the plume core IR emission [41]. It was found that high aspect ratio nozzles and the bypass ratio of unity have the potential effectiveness in the design of aircraft engine for low IR signature. However, the

simplicity of the model used restricts the usefulness of the results to the preliminary design phase only.

An experimental investigation of 0.1-scale model exhaust nozzles, namely, a single axisymmetric convergent, a twin axisymmetric convergent-divergent, and twin two-dimensional (2D) wedge, was carried out by Banken et al. [42]. They evaluated the effects of total temperature, nozzle pressure ratio, nozzle orientation, and aspect angle on the hot parts and plume IR signatures. It was shown that the indicated parameters have significant impacts on the plume emissions while, in general, the differences in the plume signatures for the free nozzle concepts were found to be small.

Sugiyama et al. [43] measured the IR radiation emitted by the plumes exhausting through straight and deflected rectangular nozzles with a wide range of aspect ratios. Scale nozzle models of roughly 1/20 of an actual size were used. Increasing the aspect ratio led to a rapid reduction in the radiation intensity from a side view of the plumes in comparison with the plume of an axisymmetric nozzle. A minor decay in the radiation was registered for the plumes from the deflected nozzles for measurements from a top view.

An experimental study of small-scale convergent four-notch nozzles to investigate the effect of the notched sections on the plume IR signature reduction was performed by Dix et al. [44]. They found that the nozzle with notches of 60° reduces the plume length by 33% and therefore gives a significant emission reduction for the CO_2 wavelength of 4.3 μm when compared with the baseline axisymmetric nozzle.

From the point of view of the aircraft plume IR signature reduction, it is commonly implied that the mixing of the jet with the atmosphere must be enhanced to reduce the size and intensity of the plume [45]. In order to study the IR characteristics of full-scale plumes of different mixing behaviour, Sventitskiy and Mundt [46] carried out numerical simulations of IR emissions of exhaust plumes from geometrically simple nozzles, namely, a conventional circular, a rectangular, and lobed. For all exhaust flows investigated, the turbulent jet was considered to be similar in temperature and species concentrations to exhaust from a turbojet engine. It was found that the emission from the rectangular plume is sensitive to the direction of observation, whereas the sensitivity of the lobed plume emission to the direction of observation is negligible. It was also demonstrated that the rectangular and lobed plumes emit, respectively, by 20% and 17% less than the baseline circular plume.

And finally, Sventitskiy and Mundt [47] investigated the effect of lobed mixer of a realistic turbofan engine on the plume IR signature by performing SNB calculations in the spectral range $1250-4250$ cm^{-1}. They found that, when compared to an annular mixer, the lobed mixer provides a reduction of the IR emission by 80% in the spectral range modeled.

1.3 Aims and Objectives

The aim of the present work is the development of a new predictive technique for exhaust plume IR emissions. This technique seeks to overcome the previously mentioned difficulties of the existing methods (see p. 3). The new method is based on the finite volume approach to radiation modeling. The advantages of the FVM over other RTE solution methods are:

1. Unlike DOM, the FVM is fully conservative – it does ensure conservation of radiative energy.
2. Unlike MC methods, the FVM is free of statistical errors.
3. Since the FVM provides a strictly 3D treatment of the RTE, no additional approximations with respect to scattering are required (for instance, an assumption that the phase function consists of two or six components); therefore, FVM solutions are affected by the numerical errors only, and they are not affected by any errors associated with the use of various approximate assumptions.
4. The FVM for radiation transport shares many similarities with solution methods used in CFD; consequently, for coupled radiation/CFD problems, a FVM procedure for the calculation of radiative heat transfer can easily be incorporated into an existing flow solver to take account of radiation effects.
5. The FVM formulates radiative properties in gaseous mixtures in terms of the absorption coefficient rather than in terms of the gaseous column transmissivity, and so the problem of incompatibility with scattering intrinsic to transmissivity-based SNB models is eliminated; moreover, this allows the use of advanced spectral models based upon narrow-band k-distributions such as correlated-k (CK). Coupling of the FVM with the CK model for performing accurate narrow-band calculations is a key feature of the current study.

The objectives of the research are the following:

1. Assessment of the CK method by comparing with LBL solutions.
2. Implementation of the FVM and coupling with the CK method for gas mixtures, with radiative property models for nongray particles (soot and model particles), and with anisotropic scattering phase functions.
3. Development and validation of a FVM solver.
4. Development and validation of a RTE solver based on the RT method coupled with both the CK and SNB models.
5. Development of numerical algorithms intended for the evaluation of the directional IR characteristics of exhaust plumes based upon the intensity fields obtained using the FVM and RT methods.

6. Carrying out accurate CFD calculations of temperature and species fields in a realistic aircraft engine exhaust that will be employed as a plume model.
7. Evaluation of the conventional IR signature prediction technique using the ray tracing based RTE solver and the SNB models with various model parameters.
8. Validation of the FVM/CK signature prediction approach by performing calculations of directional IR emissions from the plume comprising the gaseous products of combustion and by comparing the simulation results with the solutions obtained using the RT solver, SNB models, and gray-band approximations.
9. Study of the IR characteristics of exhaust plumes with scattering particles.
10. Development and verification of a new plume radiation prediction code that includes both the "standard" and newly developed methods.

1.4 An Outline of the Chapters to Follow

The remainder of this work is organized as follows. In **Chapter 2**, RTE solution methods relevant to the current study are considered. This involves the discussion of the RT technique, FVM, spatial differencing scheme and discretization, and RTE solvers.

Chapter 3 discusses narrow-band models for IR radiative properties of molecular gases. The transmissivity-based SNB approach, the absorption-coefficient-based CK method, and gray-band approximations are described in detail. The CK method is validated against LBL calculations performed for a one-dimensional (1D) test problem. The radiative properties of particles and approximate scattering phase functions (relevant to the present work) are also considered.

Chapter 4 describes the exhaust plume that is employed here as a radiatively participating medium. The plume represents a jet flow from a realistic turbofan. The temperature, pressure, and species fields in the plume based on CFD calculation and required for radiation analysis are presented.

In **Chapter 5**, the directional IR emissions from the plume are predicted. The plume is assumed to be a nonscattering (gas-only) medium. The predictions are first performed using the SNB models with various model parameters. Benchmark solutions for validating the FVM are then obtained using the RT technique and the CK model. Further, the CK results are compared with those of SNB. The FVM is next assessed by carrying out calculations with various angular discretizations on a given spatial grid. The calculations are conducted by coupling the FVM with both the CK and gray-band models.

Chapter 6 presents and analyses the results of IR signature calculations from plumes loaded with nonscattering/scattering particles using the FVM.

Chapter 7 concludes the current research by summarizing the important results and proposing some topics for possible future studies.

In **Appendix A**, the radiative characteristics, which are typically used to evaluate exhaust plume IR emissions, are derived based on the spectral radiance fields obtained through the solution of the RTE.

Appendix B seeks to validate the FVM and the CK method implemented in the present study. Calculations of total radiative quantities, such as the radiative heat flux and its divergence, in 3D rectangular enclosures containing gas and gas-soot mixtures are performed for five test cases reported in the literature.

Mathematical derivations of the total radiative quantities computed in Appendix B are presented in **Appendix C**.

Lastly, **Appendix D** gives a brief overview of the JERAD software. This software has been developed by the author and is used in this work for carrying out all calculations.

Chapter 2

Governing Equations and Solution Methods

2.1 Introduction

A number of numerical methods for solving the RTE can be found in the literature. These are zonal, flux, Monte Carlo, spherical harmonics (P_N-approximation), discrete ordinates (S_N-approximation), discrete transfer, finite element, finite volume methods [23], etc. The choice of one or other method is determined by the nature of the problem to be solved.

In the current work the emphasis is placed upon thermal radiation predictions from exhaust plumes. The radiative characteristics of plumes are directional quantities. Consequently, the RTE solution method has to provide the radiative intensity field resolved in all directions. For instance, the popular P-1 method, in which the RTE is reduced to a set of spatial partial differential equations in terms of direction integrated radiative quantities, would be unsuitable for the purposes of the present study.

The discussion in this chapter is therefore restricted to the RT technique and the FVM. This includes a consideration of the basics of those methods and a discussion of the developed RTE solvers.

2.2 Spectral Radiance

Spectral radiance (spectral intensity, specific intensity) is the fundamental radiative quantity that describes the temporal (t), spatial (x, y, z), directional (θ, φ), and spectral (η) dependencies of the radiation field inside a participating (absorbing, emitting, and scattering) medium. The spectral radiance I_η is defined as the rate of radiative energy flow per unit solid angle per unit projected area and per unit wavenumber [48],

$$I_\eta(t,x,y,z,\theta,\varphi,\eta) = \lim_{\Delta A,\Delta\Omega,\Delta\eta,\Delta t\to 0} \frac{\Delta E_\eta}{\Delta A(\vec{n}\cdot\vec{s})\Delta\Omega\Delta\eta\Delta t}, \tag{2.1}$$

where ΔE_η is the amount of radiation energy (expressed in J) transferred in the spectral region $\Delta\eta$ centered on wavenumber η, ΔA is the elementary area with the normal vector $\vec{n}$ located at position x, y, z, $\Delta\Omega$ is the elementary solid angle about the direction described by the zenith angle θ and the azimuth angle φ, $\vec{s}$ is the unit direction vector, and Δt is the elementary time interval centered on time t (Fig. 2.1).

In most solutions of radiative transfer problems the temporal dependence of the spectral radiance is neglected (because the characteristic time scale of a problem t^* is usually much greater than time of propagation of electromagnetic radiation, i.e. $t^* \gg L^*/c$, with L^* and c being, respectively, the characteristic length scale and speed of light [48]). The spectral radiance is then a six-dimensional quantity. Therefore, the radiation field has to be resolved in both the spatial (3D) and angular (2D) domains, and in wavelength (1D).

Methods for the treatment of the spatial and angular domains are considered here. The treatment of the wavelength dependence of the radiation field (on a narrow-band basis) will be discussed in Chapter 3.

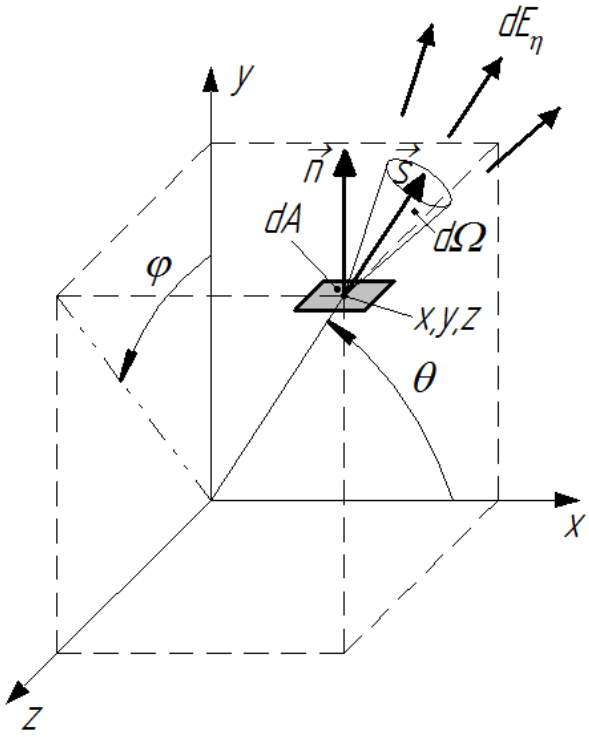

Figure 2.1: Schematic of geometry for the definition of spectral radiance

2.3 The Equation of Radiative Transfer

The steady-state spectral (monochromatic) RTE for an absorbing, emitting, and scattering medium under assumption of local thermodynamic equilibrium (LTE) is [23]

$$\frac{dI_\eta(\vec{s})}{ds} = \kappa_\eta I_{b\eta} - \kappa_\eta I_\eta(\vec{s}) - \sigma_{s\eta} I_\eta(\vec{s}) + \frac{\sigma_{s\eta}}{4\pi} \int_{4\pi} I_\eta(\vec{s}\,')\Phi_\eta(\vec{s}\,', \vec{s})\, d\Omega', \tag{2.2}$$

where $I_\eta(\vec{s})$ is the spectral radiance in the angular direction $\vec{s}$, $I_{b\eta}$ is the spectral blackbody intensity (Planck function), $\kappa_\eta = \kappa_{g\eta} + \kappa_{p\eta}$ is the spectral absorption coefficient that is the sum of gas and particulate contributors, $\sigma_{s\eta}$ is the spectral scattering coefficient, Φ_η is the scattering phase function, s is the coordinate along the radiation propagation path, and Ω is the solid angle.

The RTE, Eq. (2.2), is a first-order integro-differential equation formulated in terms of the spectral radiance (the so-called primitive variable formulation [49]). The first term on the right-hand side of Eq. (2.2) is augmentation of I_η through emission. The second and third terms are attenuations through absorption and out-scattering. The fourth term is augmentation due to in-scattering.

Eq. (2.2) may be written as

$$\vec{s} \cdot \nabla I_\eta(\vec{s}) = \beta_\eta (S_\eta(\vec{s}) - I_\eta(\vec{s})), \tag{2.3}$$

where the extinction coefficient $\beta_\eta = \kappa_\eta + \sigma_{s\eta}$ and the source function S_η is given by

$$S_\eta(\vec{s}) = \frac{1}{\beta_\eta} \left(\kappa_\eta I_{b\eta} + \frac{\sigma_{s\eta}}{4\pi} \int_{4\pi} I_\eta(\vec{s}\,')\Phi_\eta(\vec{s}\,', \vec{s})\, d\Omega' \right). \tag{2.4}$$

It follows from Eq. (2.3) that, if S_η is known, the RTE can be interpreted as pure convection of a scalar (intensity) through a given constant "velocity" field [50]. The components of this field in the x, y, and z directions are the corresponding direction cosines.

Eq. (2.3) is subject to the boundary condition formulated for a surface bounding the medium. In the case of a gray surface that emits and reflects diffusely, the boundary condition can be written as

$$I_{\eta,0}(\vec{s}) = \epsilon I_{b\eta}(T_0) + \frac{1-\epsilon}{\pi} \int_{\vec{n}\cdot\vec{s}\,'<0} I_\eta(\vec{s}\,')|\vec{n} \cdot \vec{s}\,'|\, d\Omega', \tag{2.5}$$

where $I_{\eta,0}$ is the intensity leaving the surface, ϵ is the surface emissivity, T_0 is the temperature of the surface, and $\vec{n}$ is the inward surface normal.

2.4 Solution of the RTE

Let the source function given by Eq. (2.4) be a known quantity; then Eq. (2.3) can be immediately integrated to yield the following solution:

$$I_{\eta,s}(\vec{s}) = I_{\eta,0}(\vec{s}) \exp\left[-\int_0^s \beta_\eta(s')\,ds'\right] + \int_0^s \beta_\eta(s') S_\eta(s') \exp\left[-\int_{s'}^s \beta_\eta(s'')\,ds''\right] ds', \tag{2.6}$$

where $I_{\eta,s}$ is the intensity in the direction $\vec{s}$ at the point under consideration s.

Eq. (2.6) represents the formal RTE solution because the source function itself is an integral over a set of directions and contains the unknown intensities (see Eq. (2.4)).

In the absence of scattering by particles the source function reduces to $I_{b\eta}$ and $\beta_\eta \equiv \kappa_\eta$, so that

$$I_{\eta,s}(\vec{s}) = I_{\eta,0}(\vec{s}) \exp\left[-\int_0^s \kappa_\eta(s')\,ds'\right] + \int_0^s \kappa_\eta(s') I_{b\eta}(s') \exp\left[-\int_{s'}^s \kappa_\eta(s'')\,ds''\right] ds'. \tag{2.7}$$

The above two equations can be used in conjunction with a RT technique for numerical calculation of radiative heat transfer (for instance, by using the discrete transfer method (DTM)). When treating absorption/emission processes without scattering, the integration in Eq. (2.7) along a ray through the medium is straightforward since the equation is an explicit expression for intensity, and so the ray can be treated independently without taking account of surrounding conditions. The inclusion of scattering requires a RT procedure in multidimensions [13], and the solution of Eq. (2.6) is iterative. Numerical aspects related to the implementation and use of RT are discussed further in Section 2.6.[1]

[1]The conventional treatment of IR radiation from exhaust plumes is based upon a 1D integration of the source function along a line-of-sight (LOS) [11, 15, 16]. The calculation is generally repeated for many lines-of-sight through the plume, thereby requiring ray tracing into a predetermined plume IR emission direction. In the current study, the RT method is associated with this technique (except for Appendix B). The two terms "ray" and "LOS" are considered equivalent.

2.5 Finite Volume Method for Radiative Transfer

2.5.1 Comparison with DOM

The FVM for predictions of radiative heat transfer in participating media [51–60] is the result of further improvements to the popular DOM. The method treats radiation in a way that is very similar to what is done in CFD. The most significant advantage of the FVM is that it ensures strict conservation of radiative energy (unlike DOM) [23, 58].

Moreover, the DOM does not ensure the conservation of scattered energy in the case of anisotropic scattering, e.g. the normalization condition for the scattering phase function is not satisfied (see Eq. (3.54) of Section 3.7). A common practice to force the scattered energy to be conserved is the renormalization of the scattering phase function. This technique, however, induces a deformation of the discretized phase function leading to a decrease in the accuracy of radiation predictions, especially in the case of acute forward scattering [61]. On the contrary, the FVM preserves the shape of the actual phase function on average (see Eq. (2.11) below), and so there is no loss of scattered radiation [58].

Both the DOM and FVM use a finite volume approach for spatial discretization. The major difference between the methods is the treatment of angular space. In the DOM, numerical quadratures, such as the S_N [62, 63] and T_N [64] quadrature sets, are utilized for angular discretization. The DOM is then best described as finite volume (in space)–quadrature (in direction) [58]. In the FVM, the finite volume approach is used both in space and direction. Therefore, the FVM can be defined as finite volume (in space)–finite volume (in direction) [58]. It is worth mentioning that the FVM and DOM are the only existing methods (aside from the statistical MC method) which permit arbitrary levels of accuracy of radiative transfer computations without adding to their mathematical complexity [23].

2.5.2 Basic Relations

A 3D formulation of the FVM in Cartesian coordinates is obtained by integrating the RTE, Eq. (2.3), over a control volume ΔV and then over a control solid angle $\Delta\Omega^l$ (hereafter, the superscript l denotes a given angular direction), as illustrated in Fig. 2.2. The volume integral on the left hand side is rewritten as an integral over the entire bounding surface of the control volume by using the divergence theorem. This gives

$$\sum_k I_k^l(\mathbf{s}^l \cdot \vec{n}_k)A_k = \beta_P(S_P^l - I_P^l)\Delta V \Delta\Omega^l, \tag{2.8}$$

where $\vec{n}$ is the outward face normal as indicated in Fig. 2.2, A is the face area, the subscript k designates the midpoint of a control volume face and runs over all volume's

faces ($k = e, w, n, s, b, t$ for the control volume shown in Fig. 2.2), and the superscript l denotes a value associated with $\Delta\Omega^l$. It is assumed in Eq. (2.8) that the magnitude of the intensity is constant within the control solid angle $\Delta\Omega^l$ and the radiative properties are constant within the volume ΔV. All quantities on the right hand side, i.e. β_P, S_P^l, and I_P^l, are evaluated at the volume center P. The wavelength dependence indicated by the subscript η in Eq. (2.3) is omitted for the sake of simplicity. One should of course remember that Eq. (2.8) holds on a spectral basis.

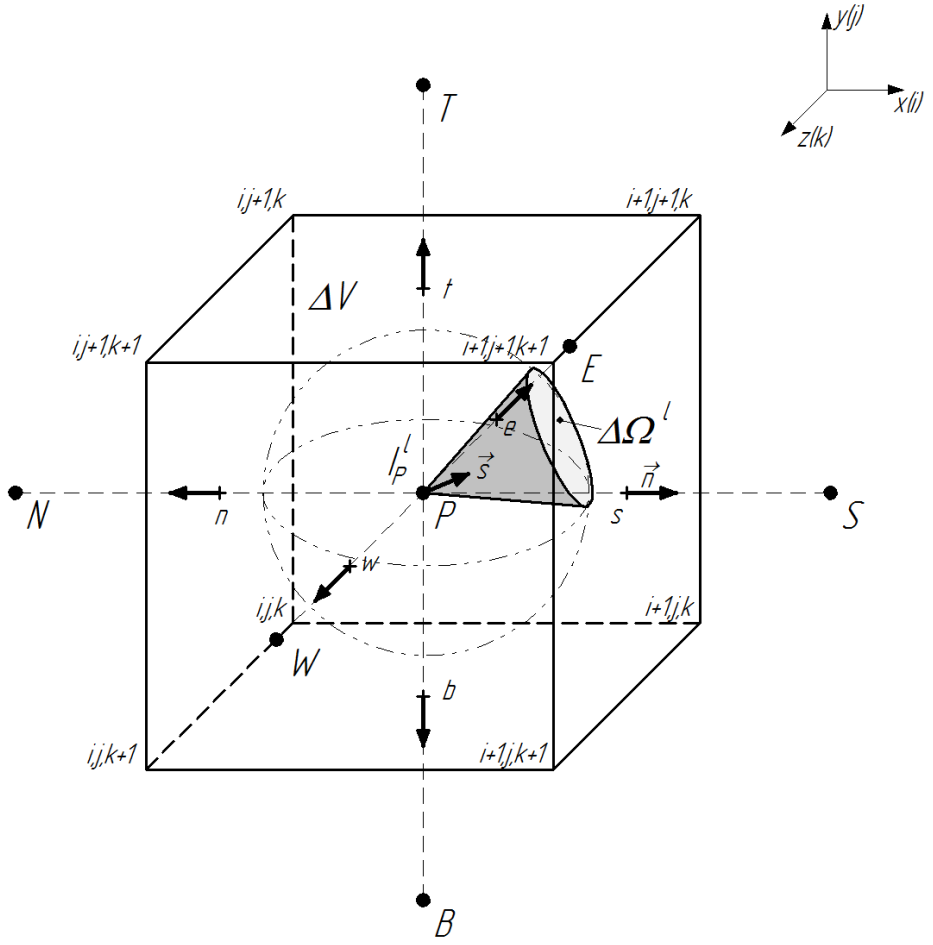

Figure 2.2: A hexahedral control volume and a control solid angle

Note that in Eq. (2.8) the radiation direction varies within the control angle. Otherwise the DOM's discretization equation would be obtained [54]. In other worlds, the vector $\mathbf{s}^l$ has a varying length depending on the size of $\Delta\Omega^l$ and points into an average solid angle direction, i.e.

$$\mathbf{s}^l = \int_{\Delta\Omega^l} \vec{s}\, d\Omega. \tag{2.9}$$

The source term at the control volume center P is

$$S_P^l = \frac{1}{\beta_P}\left(\kappa_P I_{b,P} + \frac{\sigma_{s,P}}{4\pi}\sum_{l'=1}^{N} I_P^{l'}\,\bar{\Phi}^{l'l}\Delta\Omega^{l'}\right), \tag{2.10}$$

where N is the number of discrete directions and $\bar{\Phi}^{l'l}$ is the average scattering phase function from direction l' to direction l defined as

$$\bar{\Phi}^{l'l} = \frac{1}{\Delta\Omega^l\,\Delta\Omega^{l'}}\int\limits_{\Delta\Omega^l}\int\limits_{\Delta\Omega^{l'}} \Phi(\vec{s}',\vec{s})d\Omega' d\Omega. \tag{2.11}$$

The key points of the FVM are an accurate evaluation of the average phase function given by Eq. (2.11) to ensure conservation of radiative energy and a spatial discretization technique to relate the intensities at the face centers I_k^l to those at the volume centers I_P^l. The evaluation of $\bar{\Phi}^{l'l}$ can be performed either analytically or numerically. The spatial differencing scheme is considered in the next subsection.

2.5.3 Spatial Differencing Scheme

Downstream cell face intensities may be approximated by the following linear differencing scheme that involves two upstream values (see, e.g., Liu et al. [50]):

$$I_f^l = I_P^l + \left(\frac{1}{\psi} - 1\right)(I_P^l - I_{uf}^l), \tag{2.12}$$

where I_P^l is the cell center intensity. For directions with negative direction cosines ($\mathbf{s}^l \cdot \vec{e}_i < 0$, $i = x, y, z$), I_f^l, $f = e, n, b$, are the intensities at east, north, and bottom cell faces, and I_{uf}^l, $uf = w, s, t$, are the corresponding intensities at west, south, and top cell faces, as illustrated in Fig. 2.2. The factor ψ is assumed constant in all three Cartesian directions as well as in all angular directions.

Conventional schemes applied to the DOM and FVM are the first-order step and second-order diamond schemes [50, 56, 65–67]. They are obtained from Eq. (2.12) by setting $\psi = 1$ and $\psi = 0.5$, respectively. The step scheme is known as the upwind scheme in the field of CFD, whereas the diamond scheme resembles the central difference scheme [68]. The diamond scheme can produce oscillations in intensity solutions (i.e. the scheme is unbounded) and negative intensity values that are physically unrealistic [66, 69]. The step scheme does ensure boundedness and positivity of the primitive variable (intensity) (see, e.g., Jessee and Fiveland [69]), but it always causes the so-called false scattering (see p. 19) whenever the radiation direction is not aligned with grid lines.

Other spatial differencing schemes are exponential-type schemes [50, 51, 66], the second-order upwind scheme for 3D unstructured grids [70], standard (MINMOD, MUSCL,

CLAM, SMART, etc.) [69, 71] and skewed [72] high resolution schemes (HRS), and schemes based on the TVD (total variation diminishing) methodology [73]. A comprehensive study of various schemes has been performed by Coelho [74].

In this work, the step (upwind) scheme is chosen as the spatial differencing scheme. Fig. 2.3 shows the scheme stencil drown in two dimensions for the sake of clarity. The relationships between the intensities are represented as coloured arrowheads. As can be seen from the figure, the step scheme sets the cell face intensities equal to the respective upstream nodal (cell center) values:

$$I_e^l = I_n^l = I_P^l, \quad I_w^l = I_W^l, \quad I_s^l = I_S^l. \tag{2.13}$$

The step scheme is computationally stable and inexpensive, and it can easily be implemented in a FVM radiation code.

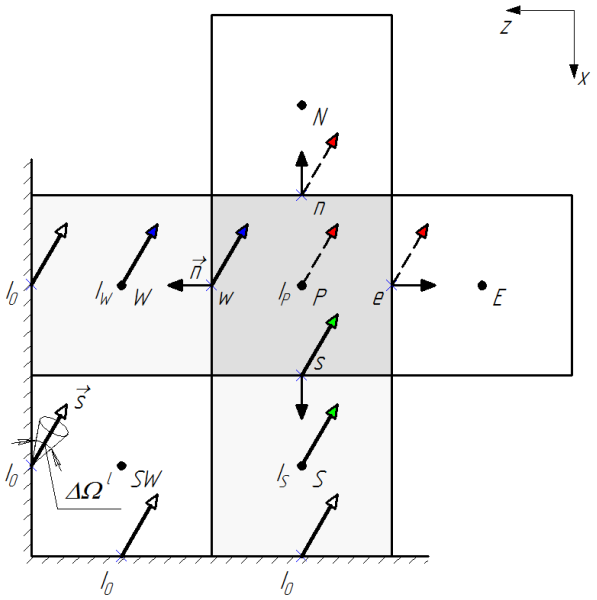

Figure 2.3: 2D stencil for spatial finite volume discretization using the step scheme

2.5.4 Derivation of the Discretized RTE

In order to obtain the final discretization form of the RTE using the step scheme, Eq. (2.8) should be linearized by removal the forward-scattering term in S_P^l (Eq. (2.10)). This reduces the iterations dependence and leads to faster convergence [75]. One obtains then the following linear equation [56]:

$$a_P^l I_P^l = a_E^l I_E^l + a_W^l I_W^l + a_N^l I_N^l + a_S^l I_S^l + a_B^l I_B^l + a_T^l I_T^l + b^l, \tag{2.14}$$

where E, W, N, S, B, T denote the east, west, north, south, bottom, and top node points around P, respectively (Fig. 2.2). In accordance with the step scheme, the coefficients and the source term in Eq. (2.14) are

$$a_{nb}^{l} = \max[-A_k(\mathbf{s}^l \cdot \vec{n}_k),\, 0], \tag{2.15}$$

$$a_P^l = \left(\beta_P - \frac{\sigma_{s,P}}{4\pi}\bar{\Phi}^{ll}\Delta\Omega^l\right)\Delta V\Delta\Omega^l + \sum_k \max[A_k(\mathbf{s}^l \cdot \vec{n}_k),\, 0], \tag{2.16}$$

$$b^l = \left(\kappa_P I_{b,P} + \frac{\sigma_{s,P}}{4\pi}\sum_{l'=1,l'\neq l}^{N} I_P^{l'}\,\bar{\Phi}^{l'l}\Delta\Omega^{l'}\right)\Delta V\Delta\Omega^l, \tag{2.17}$$

where $nb = E, W, N, S, B, T$, the subscript $k = e, w, n, s, b, t$ stands for the east, west, north, south, bottom, and top faces of the control volume ΔV, and the vector $\mathbf{s}^l$ is defined by Eq. (2.9).

2.5.5 Angular Space Discretization

Spatial domain discretization practices used in radiative transfer computations with the FVM are fully identical to those employed in CFD [68]. Therefore, the angular domain discretization, which does not exist in CFD calculations, is only considered here.

The simplest directional discretization is $N_\theta \times N_\varphi$ (employed in the current research). The total solid angle $\Omega = 4\pi$ is uniformly subdivided into discrete solid angle elements of size $\Delta\Omega^l$, $l = 1 \ldots N$. In the $N_\theta \times N_\varphi$ notation, N_θ is the number of the elements in the θ direction and N_φ is the number of the elements in the φ direction, $0 \leqslant \theta \leqslant \pi$ and $0 \leqslant \varphi \leqslant 2\pi$ are the zenith and azimuth angles, respectively. Fig. 2.4 demonstrates the uniform angular discretization scheme. In the figure, θ^-, θ^+, φ^-, φ^+ are the zenith and azimuth angles bounding the solid angle element.

The advantage of using the uniform directional discretization is that the angular grid can be easily generated and handled. The disadvantage is that the angular grid becomes denser with decreasing θ ($\Delta\Omega^l = (\cos\theta^- - \cos\theta^+)(\varphi^+ - \varphi^-)$), i.e. the grid is essentially nonuniform in Ω–space. To overcome this shortcoming, the so-called $\mathrm{FT_n}$ [76] angular discretization scheme can be used.

2.5.6 Discretization Errors

Inaccuracies in radiative transfer predictions with the FVM arise from three different sources of errors. These are 1) false scattering, 2) ray effect, and 3) control angle overlap [57, 77–80].

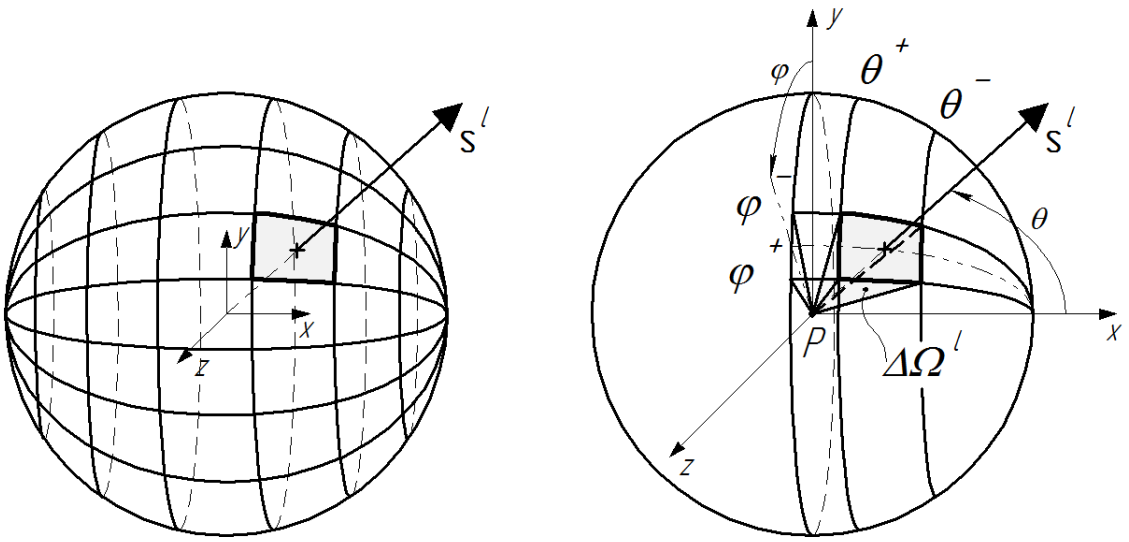

Figure 2.4: The $N_\theta \times N_\varphi$ uniform angular discretization scheme: the entire angular grid (left); a single solid angle element (right)

2.5.6.1 False Scattering

False scattering (also referred to as ray diffusion, false diffusion, or numerical smearing) is a consequence of spatial discretization errors. False scattering is analogous to numerical diffusion in CFD. This means that, in multidimensional problems, the radiation intensity appears to be nonphysically smeared. This typically occurs if a spatial differencing scheme is used in which the radiative fluxes through cell faces are treated as locally one-dimensional (i.e. without taking into account the directional effect of radiation as in the case of the step scheme) [74].

2.5.6.2 Ray Effect

Ray effect is related to the directional discretization and it is independent of the spatial discretization. There is nothing similar to this type of error in CFD. The ray effect occurs due to the fact that a continuously varying angular nature of radiation is approximated with a set of discrete angular directions associated with each control solid angle [77]. The radiation intensity is nonphysically concentrated along the center of each control angle (which is also called the ray concentration error [59, 78]).

The ray effect can be reduced by using a finer angular grid. Since directional and spatial discretization errors tend to cancel [78], an angular grid refinement has to be accompanied by using a finer spatial grid. Also, to reduce the ray effect, unstructured angular grids can be utilized [81].

2.5.6.3 Control Angle Overlap

A control angle overlap (overhang) occurs whenever a control solid angle bisects a control volume face in such a manner that the intensity associated with the control angle is not fully outgoing ($\mathbf{s}^l \cdot \vec{n} > 0$) or incoming ($\mathbf{s}^l \cdot \vec{n} < 0$) at the face. This situation is almost unavoidable for complex irregular geometries and unstructured meshes.

In this work, no special attempts are made to treat such overlaps since they would significantly increase the computational effort for the evaluation of I_P^l. Therefore, the so-called simple approximation (also known as the bold approximation [79] or "to-do-nothing" approach [59]) is used. The solid angle overlap error diminishes with solid angle refinement [78].

2.6 RTE Solvers

2.6.1 RT Solver

The RT technique solver is based on Eq. (2.7) that represents the RTE solution along a single LOS through an absorbing-emitting medium. The intensity values are obtained by solving Eq. (2.7) numerically along each LOS traced through the medium in a given direction. In the literature, this approach is sometimes referred to as the method of characteristics (MOC) [81]. In this work, the RT solver is applied to the solution of nonscattering problems only (see also p. 13).

Note that the RT method is free of spatial and directional discretization errors such as false scattering and ray effect inherent to the DOM and FVM. It can thus be used to gain benchmark solutions to validate results obtained using the methods based on the discretization of the RTE.

2.6.1.1 Absorption Coefficient Based Formulation

For calculations of intensities, each LOS through the medium is uniformly subdivided into M homogeneous slabs of length Δs defined as

$$\Delta s = \chi_s \sqrt[3]{\Delta V_{min}}, \tag{2.18}$$

where χ_s is a scale factor that allows variation of the slab length along LOS and ΔV_{min} is the minimum cell volume in the computational mesh.

Assuming the incoming intensity $I(s = s_M, \vec{s}) = 0$ (Fig. 2.5(a)), the intensity at the point $s = 0$ is

$$I(s = 0, \vec{s}) = \sum_{i=1}^{M} \left[I_b(T_{i-1/2})(1 - \tau_i) \prod_{j=0}^{i-1} \tau_j \right] \tag{2.19}$$

with a slab transmissivity given by

$$\tau_i = \exp(-\kappa_{i-1/2}(s_i - s_{i-1})) = \exp(-\kappa_{i-1/2}\Delta s), \tag{2.20}$$

where i is a spatial discretization node index and $\tau_0 = 1$. The slab temperature $T_{i-1/2}$ and absorption coefficient $\kappa_{i-1/2}$ may be calculated as

$$T_{i-1/2} = \frac{T_{i-1} + T_i}{2}, \tag{2.21a}$$

$$\kappa_{i-1/2} = \frac{\kappa_{i-1} + \kappa_i}{2}. \tag{2.21b}$$

The respective values at nodes $i - 1$ and i may be computed using an inverse distance weighting (IDW) interpolation procedure. In this case, the distance-weighted nodal value is evaluated by averaging over the known values at cell vertices surrounding a given LOS node (a practice used in CFD codes to compute gradients [68]).

Alternatively, the following explicit equation can be solved [82]:

$$I_{i-1} = \tau_i[I_i - I_b(T_{i-1/2})] + I_b(T_{i-1/2}). \tag{2.22}$$

Note that it is assumed in Eq. (2.22) that the direction of radiation propagation is from $i = M$ to $i = 0$, as shown in Fig. 2.5(a). The subscript η is intentionally omitted to emphasize that the above equations hold either spectrally or on a gray basis. Importantly, Eqs. (2.19) and (2.22) should not be confused with a finite-difference approximation of the RTE.[2]

[2] A second-order finite-difference scheme for the RTE can be found in the book by Surzhikov [48]. The discretization equation using this scheme is

$$\frac{I_{i-1} - I_i}{\Delta s} + \kappa_{i-1/2}\frac{I_{i-1} + I_i}{2} = \kappa_{i-1/2} I_{b,i-1/2}.$$

Calculations showed that the use of this scheme can lead to negative intensities similar to the diamond scheme applied to DOM. Therefore, the finite-difference approximation is not employed here.

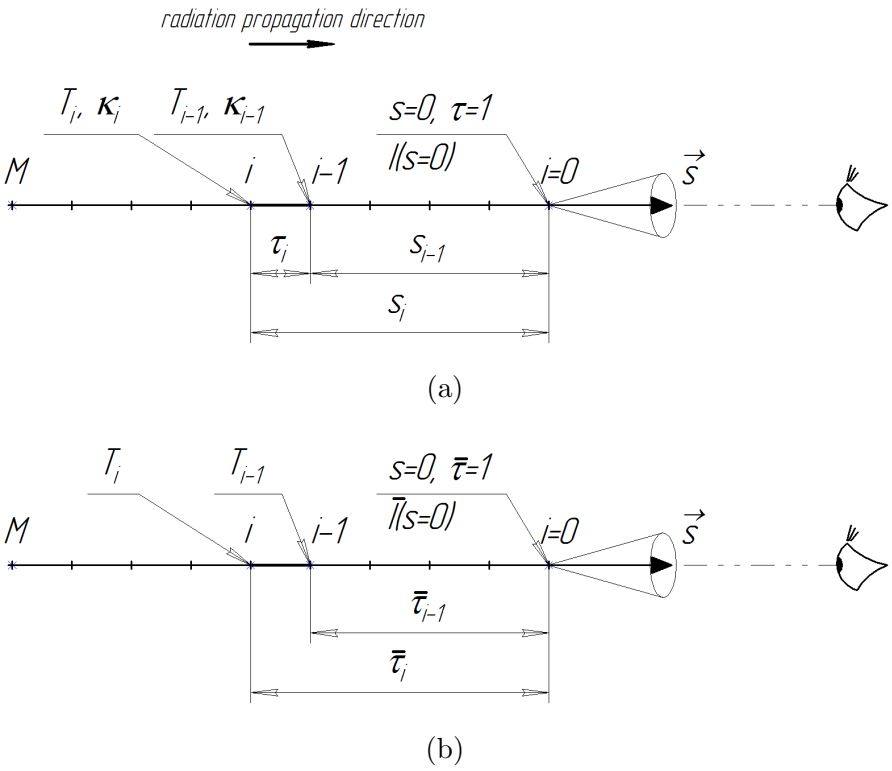

Figure 2.5: Schematic of 1D spatial grid (LOS discretization) for solving the RTE using the RT technique: (a) κ-formulation; (b) $\bar{\tau}$-formulation

2.6.1.2 Mean Transmissivity Based Formulation

Neither Eq. (2.19) nor Eq. (2.22) can be used in conjunction with band models that formulate gas radiative properties in terms of mean transmissivity $\bar{\tau}$ such as SNB models. To get a formulation that suits the SNB mean-transmissivity formalism, Eq. (2.7) must first be averaged over a narrow band $\Delta\eta$. The corresponding mean intensity can then be computed as (Fig. 2.5(b))

$$\bar{I}_\eta(s=0,\vec{s}) = \sum_{i=1}^{M} \bar{I}_{b\eta}(T_{i-1/2}) \left[\bar{\tau}_{\eta,i-1\to 0} - \bar{\tau}_{\eta,i\to 0}\right], \tag{2.23}$$

where the incoming intensity at $s = s_M$ is assumed to be zero, M is the number of slabs used to discretize the LOS, $\bar{I}_{b\eta}$ is the average blackbody intensity, $\bar{\tau}_{\eta,i-1\to 0}$ and $\bar{\tau}_{\eta,i\to 0}$ are, respectively, the mean transmissivities of the gaseous layers from $i-1$ to 0 and from i to 0, with $\tau_{0\to 0} = 1$.

It is worth noting that $\bar{\tau}_{\eta,i-1\to 0} - \bar{\tau}_{\eta,i\to 0} \neq \bar{\tau}_{\eta,i\to i-1}$, i.e. the summation in Eq. (2.23) cannot be replaced by a summation over single slab transmissivities. If the layer between nodes i and 0 contains inhomogeneities in total pressure, temperature, and/or species mole fraction, then a method for the treatment of inhomogeneous paths, such as the Curtis-Godson approximation (CGA) (discussed in Section 3.2), has to be employed.

2.6.1.3 Verification Procedure

The implementation of the RT mean transmissivity based solver was verified by executing simple spectral radiance calculations and comparing with data obtained using a code from the EM2C laboratory. This code is provided with the SNB model parameters described in [83]. The spectral radiance values were calculated along a 2 m length LOS consisting of 20 slabs at 1 bar with temperature varying between 300 and 670 K, and with varying CO_2 and H_2O concentrations.

Fig. 2.6 compares the radiances as computed here with those predicted by the EM2C code in the 150 – 4500 cm^{-1} spectral range. As seen from the figure, the relative percent difference between the results determined as

$$\text{Relative difference } \% = 100 \times \frac{\mid I_\eta \; - \; I_{\eta,\text{EM2C}} \mid}{\max\left(I_\eta,\, I_{\eta,\text{EM2C}}\right)} \tag{2.24}$$

is limited to 2.5%, showing that the solver was coded properly. This also shows that the SNB model parameters and the CGA were implemented correctly.

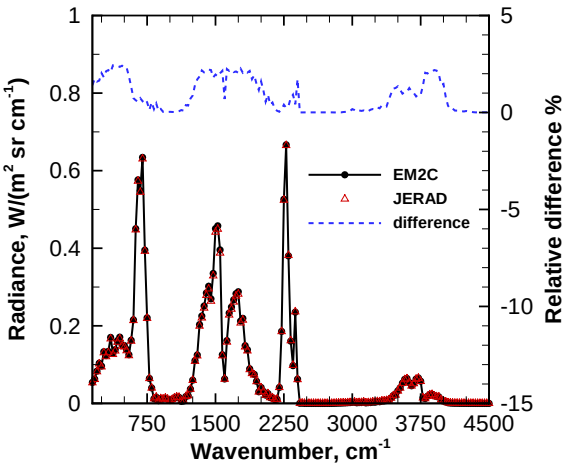

Figure 2.6: Verification of the RT technique based RTE solver

2.6.2 FVM Solver

2.6.2.1 Overview

The finite-volume discretization leads to a set of linear equations with the intensities at the cell centers as the unknowns (see Eq. (2.14)) [69]. The algebraic set is written for each direction associated with control solid angles. Coupling between the directions is incorporated in the source term. The resulting system of equations is solved using any solution technique for linear algebraic equations.

On orthogonal, structured grids the system may be solved very efficiently by using a marching technique. This technique takes advantage of the step scheme in which the downstream cell neighbour coefficients in Eq. (2.14) are equal to zero. Therefore, the I_P values are obtained by visiting the cells from upstream to downstream as $I_P = \left(\sum_{nb} a_{nb} I_{nb} + b\right) / a_P$. The source term b is treated explicitly, and so Eq. (2.14) can be solved independently for each direction. Global iterations are required to include the source term and upstream boundary conditions. The marching method converges rapidly in most cases.

2.6.2.2 Solution Strategy

With the FVM algorithm, if the distributions of thermophysical properties within a participating medium are known (for instance, through CFD computations), the RTE solution strategy consists of the steps illustrated in Fig. 2.7 and outlined below [56, 70, 84]:

1. For each direction l related to $\Delta\Omega^l$, $l = 1 \ldots N$, $I_P^l = 0$ is used as initial guess for each cell of the space mesh.
2. Coefficients and the source term in Eq. (2.14) are calculated for each cell assuming that the $I_{b,P}$, κ_P, $\sigma_{s,P}$, and $\bar{\Phi}$ values are known.
3. Eq. (2.14) is solved in each direction by using the marching technique beginning from the appropriate domain boundary where the proper boundary values $I_{k,0}$, $k = e, w, n, s, b, t$, are set.
4. The source term (Eq. (2.17)) is updated.
5. Convergence is judged by calculating a preset convergence criterion. The criterion is based on the maximum relative difference between intensity values of two consecutive global iterations

$$\max_l \left[\max_i \left(\left| \frac{\{I_{P,i}^l\}^n - \{I_{P,i}^l\}^{n-1}}{\{I_{P,i}^l\}^n} \right| \right) \right] < 10^{-6}, \tag{2.25}$$

   where $l \in [1, N]$, $i \in [1, M]$, with M being the number of cells in the computational grid, and n and $n-1$ represent the current and previous iterations.
6. Steps 3 to 5 are repeated until the convergence criterion, Eq. (2.25), is satisfied.
7. Steps 1 to 6 are repeated for each narrow band (in spectral calculations).

The FVM solver implementation is verified in Appendix B.

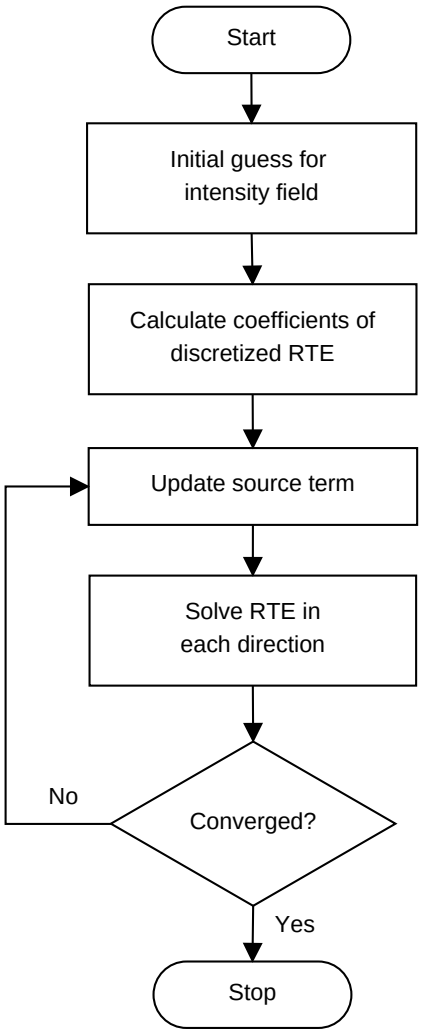

Figure 2.7: The FVM algorithm

2.7 Summary

The RTE solution methods employed in the current work have been considered theoretically in this chapter, namely the RT technique and the FVM for radiative heat transfer. Ray-tracing and finite-volume RTE solvers have been developed. The RT solver is based on the solution of the RTE in integral form. This solver is utilized for radiative transfer computations in nonscattering media. Absorption coefficient and mean transmissivity RT solver formulations were suggested. The κ-formulation is suitable for using with LBL and CK methods, whereas the $\bar{\tau}$-formulation is intended for use with SNB models. Results from the RT solver match perfectly with simulations using a radiance calculation code from the EM2C laboratory. The FVM solver is based upon the discretization of the RTE, both in space and direction. The solution of the equation is obtained by solving it explicitly using a marching method. The source term is computed from the previous iteration. The RT and FVM solvers use the same spatial computational grid. However, in the RT solver, this grid is employed solely to interpolate cell vertex values of temperature, pressure, etc. The purpose of the interpolation procedure is to provide the nodal values of thermophysical and spectral properties along a LOS in order to compute radiances. Both solvers were implemented in the JERAD code.

Chapter 3

Spectral Narrow-Band Modeling of Thermal Radiation

3.1 Introduction

The LBL method is the most accurate approach to predict the radiative transfer in participating media such as exhaust plumes. LBL calculations are exact in the sense that no additional assumptions are required to describe the spectrum behaviour. Although there are LBL codes, which have been optimized for signature calculations [85, 86], the large computational effort they require makes them impracticable for engineering applications. This is particularly true for real-life aircraft (rocket) engine exhaust plumes. The gas-dynamic structure of these plumes can be highly complex and so the RTE must be solved for each of the thousands lines-of-sight passing through the plume to provide an accurate estimation of the plume signature.

Due to the enormous computational cost associated with the LBL method, a variety of spectral models for radiative transfer have been developed. These models are suitable for a wide range of engineering applications and may be put into three groups (in order of decreasing accuracy): narrow-band models, wide-band models, and global models [23].

In the narrow-band models, the spectrum is subdivided into bands of several tens of wavenumbers, say up to 50 cm^{-1}, to assume the Planck function within each band to be constant and to avoid significant changes in the parameters of spectral lines. Computations based on narrow-band modeling provide spectrally average intensities whilst ensuring reasonable computation time and cost. The regular Elsasser model and SNB models are classical narrow-band methods.

The wide-band models treat the spectral range of the entire vibration-rotation band. Such models are more applicable to problems where total quantities, such as radiative heat fluxes, are of interest. The exponential wide-band model due to Edwards [87] is by far the most successful [23].

The global models, such as weighted-sum-of-gray-gases (WSGG) [88, 89], spectral line-based weighted-sum-of-gray-gases (SLW) [90–93], absorption distribution function (ADF) [94], and full-spectrum k-distribution (FSK) [95], treat the entire spectrum. These models are unable to provide the spectral information on gas radiative properties required for the prediction of IR emissions from plumes. The global methods are commonly used in CFD problems which involve radiation.

This chapter discusses aspects of narrow-band modeling of IR radiation. The LBL calculations, wide-band models, and global models are not considered for obvious reasons. A consideration of the band models for the prediction of radiative transfer in air plasma applications under nonequilibrium conditions is far beyond the scope of the current work, and so the interested reader is referred to the literature [96, 97].

In the sections below, the "traditional" SNB models are first considered. An alternative to the SNB models called the CK method is discussed and assessed next. Some simplified approaches to narrow-band modeling based on the so-called gray approximation are then presented, followed by the consideration of the radiative properties of soot particles and approximate scattering phase functions.

3.2 Statistical Narrow-Band Models

3.2.1 Basic Principles

Band models formulate the radiative properties of a molecular gas in terms of uniform gaseous column transmissivity averaged over a small spectral interval, $\Delta\eta$, usually 5 to 25 cm^{-1}. In absence of scattering by particles and under assumption of LTE, the solution of the RTE formulated for the average spectral intensity can then be expressed using the mean transmissivity as [15, 98]

$$\bar{I}_\eta(s) = \int_0^s \bar{I}_{b\eta}(T(s')) \frac{\partial \bar{\tau}_\eta(s' \to s)}{\partial s'} ds', \tag{3.1}$$

where $\bar{I}_\eta$ is the spectral intensity averaged over $\Delta\eta$, $\bar{\tau}_\eta(s' \to s)$ is the mean transmissivity of the gaseous column between points s' and s, $\bar{I}_{b\eta}$ is the mean Planck function, and T is the temperature. In Eq. (3.1), the subscript η designates the spectral dependence and stands for the center of $\Delta\eta$. The incoming intensity at the gas boundary ($s = 0$) is assumed to be zero.

The general expression for the mean transmissivity given by a random model is

$$\bar{\tau} = \exp\left(-\frac{\overline{W}}{\bar{\delta}}\right), \tag{3.2}$$

where $\bar{\delta} = \Delta\eta/N$ is the mean spacing between N spectral lines located within $\Delta\eta$ and $\overline{W}$ is the mean equivalent black-line width of these lines. Eq. (3.2) has nothing to do with the Beer-Lambert law and is a consequence of the statistical treatment of spectral lines inside $\Delta\eta$. A clear mathematical derivation of this formula is presented in [99].

The objective of SNB models is to provide an approximate value of $\overline{W}/\bar{\delta}$ entering Eq. (3.2). Two commonly employed SNB models due to Goody and Malkmus are discussed directly below.

3.2.2 The Goody Model

With the assumptions used in random models and assuming the exponential line strength distribution together with the Lorentz line shape (see [98] for detail), the Goody model is obtained as

$$\frac{\overline{W}}{\bar{\delta}} = xpl\bar{k}\left(1 + \frac{\pi xpl\bar{k}}{2\bar{\beta}}\right)^{-\frac{1}{2}}, \tag{3.3}$$

where x is the species mole fraction, p is the total pressure (in atm), l is the column length (in cm), $\bar{k} = \bar{S}/\bar{\delta}$ is the ratio of the mean line strength to the mean line spacing (often referred to as the mean absorption coefficient, expressed in $\mathrm{cm^{-1}\,atm^{-1}}$), and $\bar{\beta} = 2\pi\bar{\gamma}/\bar{\delta}'$ is the line overlapping parameter with

$$\bar{\gamma} = \frac{1}{N}\sum_{i=1}^{N}\gamma_i, \tag{3.4}$$

$$\bar{\delta}' = \bar{\delta}\frac{\bar{S}\bar{\gamma}}{\left[(1/N)\sum_i \sqrt{\gamma_i S_i}\right]^2}, \tag{3.5}$$

where $\bar{\gamma}$ is the mean half-width at half-maximum (HWHM), $\bar{\delta}'$ is the effective mean spacing between the lines in the spectral interval of interest, and γ_i and S_i are the HWHM and strength of each individual line inside the interval, respectively.

3.2.3 The Malkmus Model

The Malkmus model is obtained for the inverse-exponential tailed line strength distribution and the Lorentz line shape [100]. The value of $\overline{W}/\bar{\delta}$ is defined by

$$\frac{\overline{W}}{\bar{\delta}} = \frac{\bar{\beta}}{\pi}\left[\left(1+\frac{2\pi xpl\bar{k}}{\bar{\beta}}\right)^{\frac{1}{2}}-1\right], \tag{3.6}$$

where the same notations as in Eq. (3.3) are used. The mathematical derivation of Eq. (3.3) as well as of Eq. (3.6) may be found in the appendix to the treatise by Taine and Soufiani [98].

3.2.4 Weak Line Limit

The weak line limit is an asymptotic one given by

$$\lim_{u\to 0}[-\ln(\bar{\tau})] = \bar{k}u, \tag{3.7}$$

where $u = xpl$ is the optical path. Since Eq. (3.7) corresponds to the linear portion of the curve of growth, it is also called the linear limit [15] (in contrast to the square-root limit for strong absorption).

It is readily seen from Eqs. (3.3) and (3.6) that the weak line limit is a valid assumption if the condition $u\bar{k}/\bar{\beta} \ll 1$ is satisfied. The latter is true either for small optical depths (based on average absorption coefficient), $\bar{k}u \ll 1$, or when a strong overlapping of spectral lines within $\Delta\eta$ occurs, $\bar{\beta} \gg 1$. In either cases, the fine structure of the lines has no effects on radiation transport resulting in a linear absorption rate with l.

In practice, the condition $u\bar{k}/\bar{\beta} \ll 1$ leads to a significant simplification in the solution of the RTE. In this limiting case, the Beer-Lambert law is simply recovered with an absorption coefficient equal to $xp\bar{k}$, i.e.

$$\bar{\tau} = \exp(-xpl\bar{k}). \tag{3.8}$$

The use of the average absorption coefficient $\bar{\kappa} = xp\bar{S}/\bar{\delta}$ to estimate the average transmissivity by applying Eq. (3.8) is called the weak line approximation (WLA) [101]. It should be understood that the WLA and the so-called thin-gas approximation, i.e. when $\bar{\tau} \approx 1 - \bar{k}u$, are two distinct assumptions, though they are sometimes made together [15].

3.2.5 Voigt Line Profile

Eqs. (3.3) and (3.6) allow for the collision broadening of spectral lines only. To take a proper account of combined effects of collision and Doppler broadening, the mixed line shape (Voigt profile) must be used [23]. Since no analytical expression exists for the mean equivalent black-line width $\overline{W}_V$ of a set of Voigt absorption lines, additional approximations combining the Lorentz $\overline{W}_L$ and the Doppler $\overline{W}_D$ equivalent widths are commonly employed [98].

One of the approximations assumes the form [48, 98, 102]

$$\frac{\overline{W}_V}{\bar{\delta}} = xpl\bar{k}\sqrt{1 - Y^{-1/2}},$$
$$Y = \left[1 - \left(\frac{1}{xpl\bar{k}}\frac{\overline{W}_L}{\bar{\delta}}\right)^2\right]^{-2} + \left[1 - \left(\frac{1}{xpl\bar{k}}\frac{\overline{W}_D}{\bar{\delta}}\right)^2\right]^{-2} - 1. \tag{3.9}$$

This approximation neglects the smaller of the two equivalent widths as long as they differ by a factor of 3 or more [102]. Eq. (3.9) is used in conjunction with the Goody model to form the NASA single line group (SLG) model proposed by Ludwig et al. [102]. The SLG model as well as the MLG (multiple line group) model [102] are used, for instance, in the NATO Infrared Air Target Model (NIRATAM) [6, 7].

The most satisfactory approximation, which provides an accuracy of 8-10% [48, 98], was introduced by Rodgers and Williams [103] for a single spectral line with the Voigt profile. This approximation can also be applied to a group of lines and is given by

$$\frac{\overline{W}_V}{\bar{\delta}} = \left[\left(\frac{\overline{W}_L}{\bar{\delta}}\right)^2 + \left(\frac{\overline{W}_D}{\bar{\delta}}\right)^2 - \left(\frac{1}{xpl\bar{k}}\frac{\overline{W}_L}{\bar{\delta}}\frac{\overline{W}_D}{\bar{\delta}}\right)^2\right]^{\frac{1}{2}}. \tag{3.10}$$

Expressions for $\overline{W}_D/\bar{\delta}$ entering Eqs. (3.9) and (3.10) may be found in the literature (see, e.g., [15, 102, 104]).

3.2.6 The Curtis-Godson Approximation

Both the Goody and Malkmus models are formulated for a homogeneous path of length l. For nonuniform media, which are of the most practical interest, either the CGA or the formal Lindquist-Simmons approximation can be used [98]. The CGA is known to be the most widely applied method to address medium nonhomogeneity, and so this approximation is considered here.

In the CGA, a nonuniform optical path between abscissas s_1 and s_2 is replaced by an effective uniform one. This yields the following expressions for the mean transmissivity:

$$\bar{\tau}_{\mathrm{CGA}}(s_1, s_2) = \exp\left\{-u\bar{k}_{\mathrm{CGA}}\left(1 + \frac{\pi u\bar{k}_{\mathrm{CGA}}}{2\bar{\beta}_{\mathrm{CGA}}}\right)^{-\frac{1}{2}}\right\}, \tag{3.11}$$

$$\bar{\tau}_{\mathrm{CGA}}(s_1, s_2) = \exp\left\{-\frac{\bar{\beta}_{\mathrm{CGA}}}{\pi}\left[\left(1 + \frac{2\pi u\bar{k}_{\mathrm{CGA}}}{\bar{\beta}_{\mathrm{CGA}}}\right)^{\frac{1}{2}} - 1\right]\right\}. \tag{3.12}$$

Eq. (3.11) is for the CGA applied to the Goody model, whereas Eq. (3.12) is for the CGA applied to the Malkmus model. In the equations, the parameters of the equivalent uniform path are

$$\bar{k}_{\mathrm{CGA}} = \frac{1}{u}\int_{s_1}^{s_2} x(s)p(s)\bar{k}(s)\,ds, \tag{3.13}$$

$$\bar{\beta}_{\mathrm{CGA}} = \frac{1}{u\bar{k}_{\mathrm{CGA}}}\int_{s_1}^{s_2} x(s)p(s)\bar{k}(s)\bar{\beta}(s)\,ds, \tag{3.14}$$

with u defined by

$$u = \int_{s_1}^{s_2} x(s)p(s)\,ds. \tag{3.15}$$

The CGA relies on an assumption that the widths and strengths of all lines in a given spectral range $\Delta\eta$ vary in a similar manner with temperature, pressure, and species composition between s_1 and s_2 (scaling approximation), i.e. [23, 98]

$$\gamma_i(s) = \gamma_{i,0}\, f_\gamma(s), \tag{3.16}$$

$$S_i(s) = S_{i,0}\, f_S(s), \tag{3.17}$$

where the subscript i runs over all the lines inside $\Delta\eta$, $i = 1 \ldots N$. The constants $\gamma_{i,0}$ and $S_{i,0}$ are functions of η only, whereas $f_\gamma(s)$ and $f_S(s)$ are functions of the physical coordinate s along the path, and they are the same for each line. Mathematically, Eqs. (3.16) and (3.17) mean that the frequency and spatial integrations can be separated yielding Eq. (3.14).

While being rather acceptable for HWHM, the scaling approximation can be inaccurate for line strengths in the presence of strong temperature gradients due to rise of "hot lines" that are unimportant at room temperatures but become prominent at higher temperatures. More precisely, the CGA overestimates the spectral correlations between cold and hot lines, which is physically wrong [105].

The CGA was found to be fairly accurate for moderate degrees of inhomogeneity [98, 106]. However, because of the overcorrelation effect, it can fail when applied to remote sensing applications, i.e. when the IR radiation emitted by a gaseous mixture at high temperature is transmitted through a long atmospheric path. For such applications, a fictitious-gas based SNB model (SNBFG) [105] seems to be an appropriate candidate.

3.2.7 Treatment of Gas Mixtures

The mean transmissivity of a homogeneous gaseous column of length l containing a mixture of two species that absorb in the same spectral interval $\Delta\eta$ is

$$\bar{\tau}_{mix} = \frac{1}{\Delta\eta} \int_{\Delta\eta} e^{-(\kappa_{\eta,1}+\kappa_{\eta,2})l}\, d\eta = \frac{1}{\Delta\eta} \int_{\Delta\eta} \tau_{\eta,1}\tau_{\eta,2}\, d\eta, \tag{3.18}$$

where $\kappa_{\eta,1}$ and $\kappa_{\eta,2}$ are, respectively, the monochromatic absorption coefficients of species 1 and 2, and $\tau_{\eta,1}$ and $\tau_{\eta,2}$ are the corresponding transmissivities.

Considering the absorption coefficients as random variables over $\Delta\eta$ and introducing a joint probability density function (PDF) $f(\kappa_1, \kappa_2)$, the expression for $\bar{\tau}_{mix}$ is transformed into

$$\bar{\tau}_{mix} = \int_0^\infty\!\!\int e^{-(\kappa_1+\kappa_2)l} f(\kappa_1, \kappa_2)\, d\kappa_1\, d\kappa_2. \tag{3.19}$$

If the κ_1 and κ_2 are now assumed to be statistically independent, then the joint PDF is the product of PDFs for κ_1 and κ_2 considered separately, $f(\kappa_1)$ and $f(\kappa_2)$, and Eq. (3.19) reduces to

$$\bar{\tau}_{mix} = \int_0^\infty e^{-\kappa_1 l} f(\kappa_1)\, d\kappa_1 \int_0^\infty e^{-\kappa_2 l} f(\kappa_2)\, d\kappa_2 = \bar{\tau}_1 \bar{\tau}_2. \tag{3.20}$$

Eq. (3.20) can be generalized to a mixture of M absorbing species to take the final form

$$\bar{\tau}_{mix} = \prod_{i=1}^{M} \bar{\tau}_i, \tag{3.21}$$

which claims that, if one treats the absorption coefficients of the M species as statistically independent random variables, the mean transmissivity of the mixture can be evaluated as the product of the transmissivities of the individual components [23].

For relatively narrow spectral intervals, say up to 25 cm^{-1}, Eq. (3.21) leads to a very good agreement with LBL calculations, as demonstrated in [98, 107]. For wide spectral intervals, the validity of Eq. (3.21) is questionable [108]. On the other hand, when employed to formulate a global spectral model, the statistically uncorrelated method leads to significant errors. This has been shown in the work [94] in which the assumption of completely uncorrelated spectra was used to model radiative transfer in a H_2O–CO_2 mixture by utilizing the ADF model.

3.2.8 SNB Model Parameters

Three quantities in Eqs. (3.3) and (3.6), i.e. $\bar{k}$, $\bar{\gamma}$, and $\bar{\delta}'$ (or its inverse value $1/\bar{\delta}'$ referred to as the line density), are the SNB model parameters. These parameters can be obtained either theoretically or experimentally, and also from spectroscopic databases such as HITRAN [109, 110], HITEMP [111], and CDSD [112, 113].

The SNB model parameters have been generated by many researches over the years. Ludwig et al. provided the well-known NASA parameters based on experimental measurements in the temperature range 300-3000 K [102]. The data were later corrected in [99]. Khmelinin and Plastinin compiled their parameters for H_2O, CO_2, CO, and HCl at temperatures of 300-3000 K [114]. These parameters are based on theoretical computations. Young provided the SNB model parameters for the 2.7-μm bands of H_2O and CO_2 in the temperature range from 100 to 3000 K [115]. Soufiani and Taine derived their high-temperature SNB parameters from the EM2C second-generation approximate spectroscopic databases [83]. The parameters were adjusted to fit LBL curves of growth in order to correct the intrinsic inaccuracies resulting from the assumptions used to build SNB models. These data have been updated by Rivière and Soufiani in [116]. Perez et al. compiled a new parameter set based on their own spectroscopic database for H_2O [117]. Lindermeir and Beier updated the NIRATAM database using a new set of the SNB model parameters derived from the HITEMP2010 spectroscopic database [118].

The SNB model parameters from various data sets have been described and compared in the author's paper [47], so the interested reader is referred to this work for more details.

3.3 The Narrow-Band Correlated-k Method

3.3.1 k-Distribution Method

A narrow-band k-distribution serves to reorder the erratic monochromatic absorption coefficient of gas media into a monotonically increasing function over a narrow band [23]. When compared to LBL calculations, the use of k-distributions decreases the number of RTE solutions required for the evaluation of the narrow band average of any radiative quantity that depends on the absorption coefficient, such as transmissivity $\bar{\tau}_\eta$, intensity $\bar{I}_\eta$, etc. In fact, the k-distribution method replaces spectral integrations over η by integrations over the values of a reordered wavenumber. Therefore, the computational effort is dramatically reduced (in comparison to that of LBL).

Let the spectral absorption coefficient κ_η be a random variable within the narrow band $\Delta\eta$. The average of any spectral quantity Q, which depends on κ_η, can then be expressed as [98]

$$\overline{Q}_\eta = \frac{1}{\Delta\eta}\int_{\Delta\eta} Q(\kappa_\eta)\,d\eta = \int_0^\infty Q(k)f(k)\,dk, \tag{3.22}$$

where k is the absorption coefficient variable and $f(k)$ is the k-distribution function for the narrow band. The k-distribution assumes the form [23]

$$f(k) = \frac{1}{\Delta\eta}\int_{\Delta\eta} \delta(k-\kappa_\eta)\,d\eta, \tag{3.23}$$

where δ is the Dirac delta function. The k-distribution is a PDF, so that $f(k)dk$ is the probability that the absorption coefficient κ_η takes values between k and $k+dk$ inside $\Delta\eta$.

The k-distribution function shows rather erratic behaviour (see [23]). In practice, it is more convenient to use a smoothly increasing function of k over $\Delta\eta$. Such a function is the cumulative distribution function (cumulative k-distribution), $g(k)$, that is expressed in terms of $f(k)$ as

$$g(k) = \int_0^k f(k')\,dk'. \tag{3.24}$$

The cumulative k-distribution represents the fraction of the spectrum whose absorption coefficient lies below the value of k [23], as illustrated in Fig. 3.1. In this figure, which depicts a 25-inverse-cm-width portion of the H_2O 2.7-μm band at $p = 1$ atm, $T = 300$ K, and $x_{H_2O} = 0.06$, a particular k-value, k_j, is selected. The respective g-value, g_j, can be

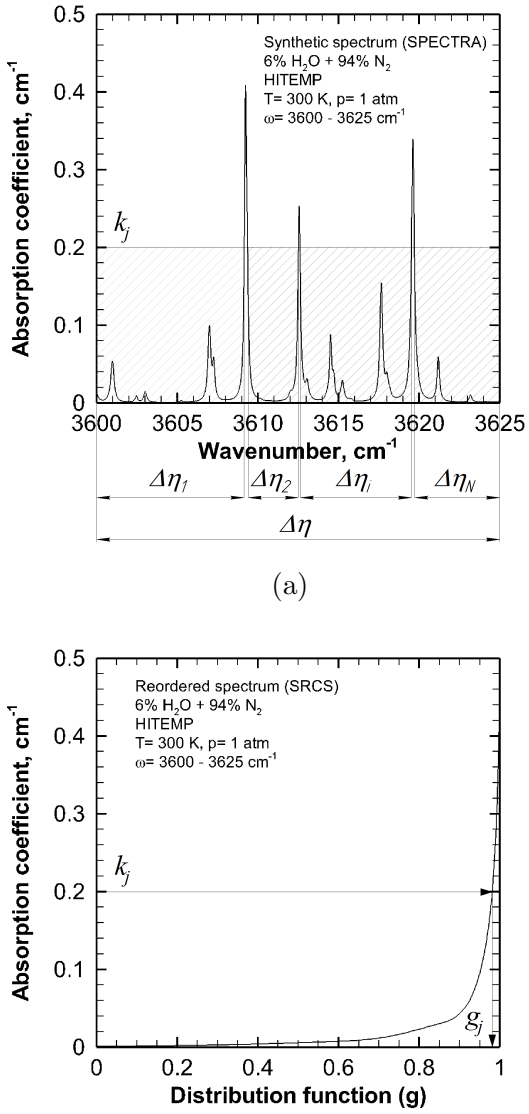

Figure 3.1: Extraction of a narrow-band k–g distribution from monochromatic absorption coefficient data: (a) high-resolution spectrum and (b) reordered spectrum

determined as $g_j = \sum_{i=1}^{N} \Delta\eta_i / \Delta\eta$, with N being the number of sub-intervals for which the absorption coefficient values are below k_j. The g_j is the probability that the absorption coefficient inside $\Delta\eta$ will attain values less than k_j. By definition, $g(k) \in [0, 1]$.

Using the cumulative k-distribution, a radiative quantity averaged over $\Delta\eta$ is

$$\overline{Q}_\eta = \frac{1}{\Delta\eta} \int_{\Delta\eta} Q_\eta \, d\eta = \int_0^1 Q_g \, dg, \tag{3.25}$$

where $Q_g \equiv Q(k(g))$, with $k(g)$ being the reordered absorption coefficient (reciprocal of $g(k)$). Inspection of Eq. (3.25) reveals that g can be interpreted as artificial wavenumber.

In order to evaluate the integral in Eq. (3.25), Gaussian-type quadratures are typically utilized [98]. Using an N-point quadrature one obtains

$$\overline{Q}_\eta = \int_0^1 Q_g \, dg \approx \sum_{i=1}^{N} \omega_i Q_{g_i}, \tag{3.26}$$

where g_i and ω_i are the quadrature points and weights, respectively.

In particular, the mean intensity is evaluated as

$$\bar{I}_\eta = \frac{1}{\Delta\eta} \int_{\Delta\eta} I_\eta \, d\eta = \int_0^1 I_g \, dg \approx \sum_{i=1}^{N} \omega_i I_{g_i}. \tag{3.27}$$

3.3.2 Nonuniform Media – Correlated-k Approximation

3.3.2.1 Basic Principles

The k-distribution method yields exact results for uniform gaseous media. However, this approach is not well suited for media where there are spatial inhomogeneities in pressure, temperature, and concentration (Fig. 3.2). Two methods are commonly used to address inhomogeneity, namely the scaling approximation and the assumption of a correlated k-distribution [119].

In the scaling approximation, spectral and spatial dependences of the absorption coefficient are assumed to be separable. In the correlated k-distribution method (CK method), it is simply assumed that the absorption coefficients at different thermophysical conditions in a nonuniform medium, say at two states $\underline{\phi}_1 = (p_1, T_1, x_1)$ and $\underline{\phi}_2 = (p_2, T_2, x_2)$ (as shown in Fig. 3.2), are spectrally correlated. This may be written as [120]

$$\text{correlated:} \qquad \kappa_\eta(\eta, \underline{\phi}) = \kappa_{\eta,0}(\eta, \underline{\phi}_0) v(\underline{\phi}, \underline{\phi}_0, \kappa_{\eta,0}), \tag{3.28}$$

$$\text{scaled:} \qquad \kappa_\eta(\eta, \underline{\phi}) = \kappa_{\eta,0}(\eta, \underline{\phi}_0) v(\underline{\phi}, \underline{\phi}_0). \tag{3.29}$$

In the above equations, the subscript 0 denotes a reference state and v is a scaling function. The scaling approximation is more restrictive, i.e. a scaled absorption coefficient is always correlated, but not vice versa [120].

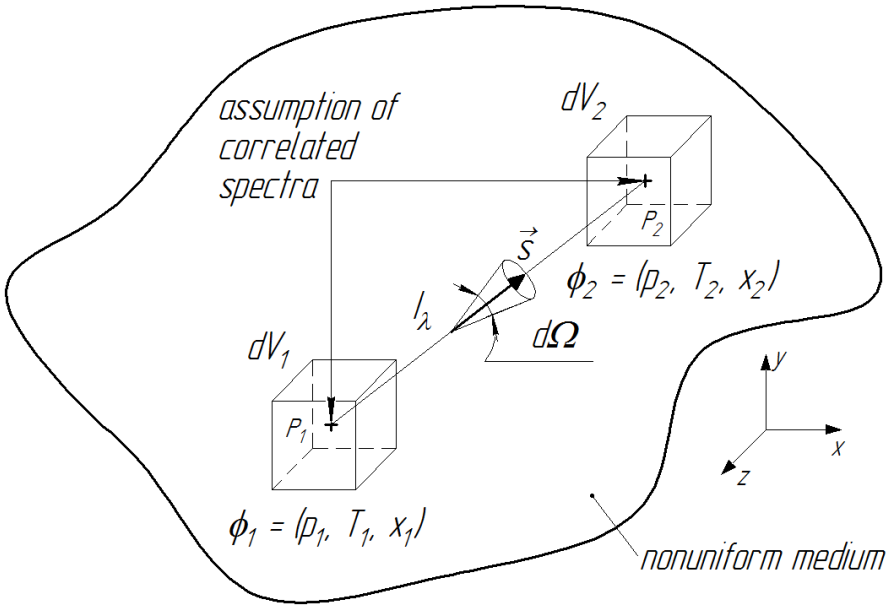

Figure 3.2: A nonuniform participating medium

In the present work, correlated k-distributions will be used for the treatment of inhomogeneous (nonuniform) media. The reason for this is that the CK method is more straightforward to implement.[1]

Unlike scaled-k, the CK method assumes that if k–g distributions are known at two locations in a nonuniform medium, then the absorption coefficient can be mapped from one location to the other [23], as demonstrated in Fig. 3.3(a) (which shows a small portion of the 2.7-μm band for a H_2O–N_2 mixture at temperatures of 300 and 700 K). In Fig. 3.3(a), the absorption coefficient at $T = 700$ K is artificially constructed to be correlated with that at $T = 300$ K. This implies that a particular g-value in the k–g distributions for 300 and 700 K corresponds to identical sets of actual wavenumber $\eta_i, i = 1 \ldots N$, regardless of $\underline{\phi}$ [119].

It should be understood that the CK method is based on the assumption of correlated absorption coefficient spectra (even though they are not). This assumption is only rigorous for a single spectral line, for the Elsasser band, for optically thin media, and if the scaling approximation is valid (optically thick media) [121]. In the general case, the CK method can yield significant errors, especially in inhomogeneous media with strong temperature gradients. This is illustrated in Fig. 3.3(b) that depicts the realistic absorption coefficient at $T = 700$ K (cf. Fig. 3.3(a)). It is easily seen that the absorption coefficients at 300 and 700 K are actually uncorrelated. The absorption coefficient at a higher temperature of 1500 K becomes even "more uncorrelated" due to rise of "hot lines".

[1]Both the correlated-k and scaled-k methods have been demonstrated to be about equally accurate when applied to narrow spectral bands. Moreover, both methods require roughly the same numerical effort [119]. However, if the scaled-k method is employed, the function $v(\underline{\phi}, \underline{\phi}_0)$ in Eq. (3.29) must be found.

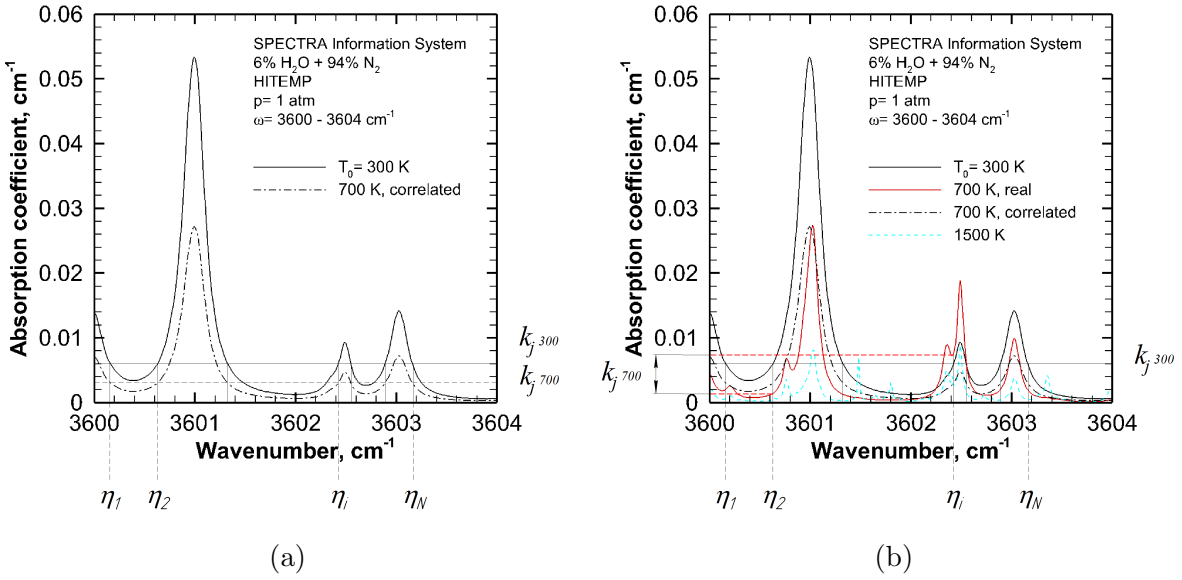

(a) (b)

Figure 3.3: Monochromatic absorption coefficient of 6% H_2O in nitrogen at 300 and 700 K across a small portion of the 2.7-μm band: (a) correlated spectra and (b) realistic spectra

The errors associated with the use of the CK method at typical gas conditions encountered in aircraft engine exhausts will be evaluated in Section 3.5.

3.3.2.2 CK and the RTE

Following Modest [107, 119], the narrow-band RTE for an absorbing, emitting, and scattering medium expressed in terms of the cumulative k-distribution assumes the form

$$\frac{dI_g}{ds} = k(g, \underline{\phi}, \underline{\phi}_s)(\bar{I}_{b\eta}(T) - I_g) - \bar{\sigma}_{s\eta}(\underline{\phi}_s) \left(I_g - \frac{1}{4\pi} \int_{4\pi} I_g(\vec{s}\,')\Phi(\vec{s}\,', \vec{s})\, d\Omega' \right), \qquad (3.30)$$

where I_g is the reordered intensity, $k(g)$ is the reordered absorption coefficient, and $\underline{\phi}_s$ is a state variable vector containing information of local particle properties. In Eq. (3.30), $\bar{I}_{b\eta}$ and $\bar{\sigma}_{s\eta}$ are, respectively, the average values of the Planck function and scattering coefficient across the narrow band. Also, it is assumed that the scattering phase function, Φ, is not dependent on η and $\underline{\phi}_s$. The absorption coefficient is the sum of gas and particulate contributors, i.e. $k(g, \underline{\phi}, \underline{\phi}_s) = k_{gas}(g, \underline{\phi}) + \bar{\kappa}_{p\eta}(\underline{\phi}_s)$, with $\bar{\kappa}_{p\eta}$ being the mean particle absorption coefficient.

In absence of scattering by particles, Eq. (3.30) reduces to

$$\frac{dI_g}{ds} = k(g, \underline{\phi})(\bar{I}_{b\eta}(T) - I_g). \tag{3.31}$$

The average narrow band intensity can be calculated from Eq. (3.27) after solving the RTE, Eq. (3.30) or (3.31), using any arbitrary solution method.

3.3.3 Multicomponent Gas Mixtures

The CK method is not straightforward to apply to spectral ranges where several species absorb simultaneously, e.g. CO_2 and H_2O near 2.7 μm. As illustrated in Fig. 3.4, an overlap of CO_2 and H_2O spectral lines occurs approximately between 3500 and 3750 cm^{-1} (for the conditions shown in the figure). Similar to the SNB models, overlapping bands require special consideration.[2]

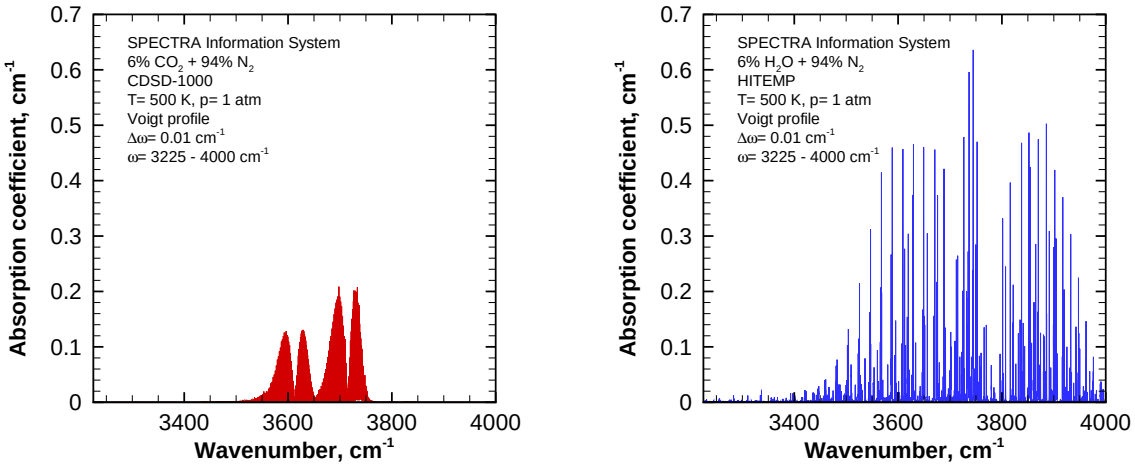

(a) (b)

Figure 3.4: High-resolution absorption coefficient spectra obtained using SPECTRA Information System [122] in the spectral range 3225 – 4000 cm^{-1} for mixtures containing (a) 6% CO_2 and 94% N_2, and (b) 6% H_2O and 94% N_2. The mixtures are at a total pressure of 1 atm and a temperature of 500 K

There is plenty of methods for handling multicomponent gas mixtures (see, e.g., [93, 123–127]). In what follows, three approaches to the treatment of overlapping bands on a narrow-band basis are considered: an approach based upon the direct use of the multiplication property for the total gas transmissivity, a summation approach, and mixing model.

[2] k-Distributions can directly be constructed for mixtures of gases, so that the mixture is simply treated as a single gas. In practice, however, this task is feasible for gas mixtures with uniform composition only. For arbitrary mixtures it is much more convenient to obtain the mixture k-distribution based on the k-distributions of the individual component species.

3.3.3.1 Direct Integration Approach

This approach is directly based upon the use of Eq. (3.21) which assumes that the absorption coefficients of different absorbing species in the mixture are statistically uncorrelated over a narrow band [98]. Let us consider, for simplicity, the case of a homogeneous mixture consisting of two species 1 and 2. Then Eq. (3.21) expressed in terms of the cumulative k-distribution becomes

$$\bar{\tau}_{mix} = \bar{\tau}_1 \bar{\tau}_2 = \int_0^1 e^{-k_1(g)\,l}\,dg \int_0^1 e^{-k_2(g)\,l}\,dg, \tag{3.32}$$

where l is the column length and $k_1(g)$ and $k_2(g)$ are, respectively, the reordered absorption coefficients for species 1 and 2.

The two integrals that appear in Eq. (3.32) can be evaluated by utilizing an N-point quadrature yielding to

$$\begin{aligned} \bar{\tau}_{mix} &= \sum_{i=1}^{N} \omega_i \exp\{-k_1(g_i)\,l\} \sum_{j=1}^{N} \omega_j \exp\{-k_2(g_j)\,l\} \\ &= \sum_{i=1}^{N}\sum_{j=1}^{N} \omega_i\,\omega_j \exp\{-[k_1(g_i) + k_2(g_j)]\,l\}. \end{aligned} \tag{3.33}$$

This implies that, by analogy with Eq. (3.26), the average intensity also satisfies the double quadrature seen in Eq. (3.33) [98] and it is expressed as (cf. Eq. (3.27))

$$\bar{I}_\eta = \sum_{i=1}^{N}\sum_{j=1}^{N} \omega_i\,\omega_j I_{g_i g_j}. \tag{3.34}$$

In the case of a purely absorbing/emitting (nonscattering) medium, the RTE at an overlapping band takes the form (cf. Eq. (3.31))

$$\frac{dI_{g_i g_j}}{ds} = [k_1(g_i, \underline{\phi}_1) + k_2(g_j, \underline{\phi}_2)](\bar{I}_{b\eta}(T) - I_{g_i g_j}), \tag{3.35}$$

where $\underline{\phi}_1 = (p, T, x_1)$ and $\underline{\phi}_2 = (p, T, x_2)$.

The direct integration approach is applicable to any number of species, M, in the mixture. Since the multiplication property, Eq. (3.21), is known to be very accurate when compared to LBL transmissivity calculations, the direct integration approach can be used as a benchmark method to validate various approximate models for handling overlapping bands. The most serious disadvantage of this approach is that it requires N^M evaluations of the RTE, Eq. (3.35), to obtain the average narrow band intensity from Eq. (3.34).

3.3.3.2 Summation Approach

The summation approach[3] is an approximate method which relies on the assumption that the reordered absorption coefficient of all species can be added up, as in the case of a monochromatic absorption coefficient. Therefore, the total (reordered) absorption coefficient at the quadrature point g_j, $k_{mix}(g_j)$, is the sum of the individual absorption coefficients, i.e.

$$k_{mix}(g_j) = \sum_{i=1}^{M} k_i(g_j), \tag{3.36}$$

where M is the number of absorbing gases.

The advantage of this method is that gas mixtures can be treated as a single gas, and therefore, only N evaluations of the RTE, Eq. (3.30) or (3.31), are required for each narrow band. The average intensity is calculated using Eq. (3.27).

3.3.3.3 The Mixing Model of Modest and Riazzi

Modest and Riazzi [107] proposed a new narrow-band mixing model that is intended for obtaining the k vs. g distribution of a gas mixture from the individual component k–g distributions. The model can mathematically be derived as follows.

Consider a binary mixture of gases. Suppose that the individual absorption coefficients are statistically uncorrelated – or, to be more precise – independent random variables. Then the mixture k-distribution is the convolution of the individual species k-distributions,

$$f_{mix}(k) = f_1(k) * f_2(k), \tag{3.37}$$

where the property was used that the PDF of the sum of two independent random variables X and Y is the convolution of their individual PDFs, i.e $f_{X+Y} = f_X * f_Y$.

By applying the convolution theorem, one can write:

$$\mathcal{L}\{f_{mix}(k)\} = \mathcal{L}\{f_1(k) * f_2(k)\} = \mathcal{L}\{f_1(k)\} \cdot \mathcal{L}\{f_2(k)\}, \tag{3.38}$$

where $\mathcal{L}$ denotes the Laplace transform operator.

[3] In the work by Liu et al. [125], this approach is called the uncorrelated method, whereas the previously described direct integration approach is called the correlated method (though it is based on the uncorrelated assumption).

Since the definition of the mean transmissivity,

$$\bar{\tau} = \int_0^\infty e^{-kl} f(k)\, dk, \tag{3.39}$$

is also the definition of the Laplace transform of $f(k)$ [107], Eq. (3.38) becomes

$$\mathcal{L}\{f_{mix}(k)\} = \int_0^\infty e^{-k_1 l} f_1(k)\, dk_1 \int_0^\infty e^{-k_2 l} f_2(k)\, dk_2. \tag{3.40}$$

In terms of the cumulative k-distributions, Eq. (3.40) can be expressed as

$$\mathcal{L}\{f_{mix}(k)\} = \int_{g_1=0}^1 \int_{g_2=0}^1 e^{-[k_1(g_1)+k_2(g_2)]\, l}\, dg_2\, dg_1. \tag{3.41}$$

Using the Laplace transform integration property one obtains

$$\mathcal{L}\left\{ \int_0^k f_{mix}(k')\, dk' \right\} = \int_{g_1=0}^1 \int_{g_2=0}^1 \frac{e^{-[k_1(g_1)+k_2(g_2)]\, l}}{l}\, dg_2\, dg_1 = \mathcal{L}\{g_{mix}(k)\}. \tag{3.42}$$

The mixture cumulative k-distribution is determined from Eq. (3.42) by taking the inverse Laplace transform, i.e.

$$g_{mix}(k_{mix}) = \mathcal{L}^{-1}\left\{ \int_{g_1=0}^1 \int_{g_2=0}^1 \frac{e^{-[k_1(g_1)+k_2(g_2)]\, l}}{l}\, dg_2\, dg_1 \right\}. \tag{3.43}$$

Since the inverse Laplace transform is a linear operator, Eq. (3.43) becomes

$$g_{mix}(k_{mix}) = \int_{g_1=0}^1 \int_{g_2=0}^1 \mathcal{L}^{-1}\left\{ \frac{e^{-[k_1(g_1)+k_2(g_2)]\, l}}{l} \right\} dg_2\, dg_1. \tag{3.44}$$

The inverse Laplace transform of $X(s) = e^{-\tau s}/s$ is the delayed unit step function, i.e. $x(t) = \mathcal{L}^{-1}\{X(s)\} = H(t-\tau)$, with H being the Heaviside step function. Therefore, Eq. (3.44) reduces to

$$g_{mix}(k_{mix}) = \int_{g_1=0}^1 \int_{g_2=0}^1 H(k_{mix} - [k_1(g_1) + k_2(g_2)])\, dg_2\, dg_1. \tag{3.45}$$

It can easily be shown that

$$\int_{g_2=0}^{1} H(k_{mix} - [k_1 + k_2])\, dg_2 = g_2(k_{mix} - k_1), \tag{3.46}$$

so that the mixing model by Modest and Riazzi takes its final form:

$$g_{mix}(k_{mix}) = \int_{g_1=0}^{1} g_2(k_{mix} - k_1)\, dg_1. \tag{3.47}$$

This expression can be extended to mixtures comprising any number of species (see [107]). However, for the case of $M > 2$, it is more practical to use it in a recursive manner.

Exact mixing of k-distributions can never be done because the reordering process obliterates any spectral information. Nevertheless, the mixing model by Modest and Riazzi results in virtually no error, as will be shown further in Section 3.5. A disadvantage of the model is that, whilst decreasing the number of RTE evaluations from N^M to N, it requires additional calculation effort to perform mixing.

3.3.4 CK vs. SNB

Table 3.1 summarizes the differences between the CK and SNB models. It is assumed in the table that $M = 2$ (number of species) and $N = 8$ (number of quadrature points in CK).

As can be seen from Table 3.1, the CK method is superior to the SNB models in many respects (see also Modest [23]). With respect to the treatment of medium inhomogeneity, the CGA employed in the SNB models is similar to the assumption of correlated spectra involved in the CK method (cf. Eqs. (3.16), (3.17), (3.28), and (3.29)). Both models perform equally well as long as severe spatial inhomogeneities in total pressure, temperature, and component gas mole fraction are not encountered. On the other hand, the SNB models require less computational cost than the CK method. Note however that, for a band of 25 cm^{-1}, LBL calculations with a wavenumber step of 10^{-3} cm^{-1} would require 25×10^3 RTE evaluations.

Table 3.1: Comparison of the CK and SNB models

Criterion	SNB models	CK method
Radiative property	Transmissivity $\bar{\tau}$	Absorption coefficient k
RTE solution method	RT	Arbitrary
Compatibility with scattering	No	Yes
Voigt broadening regime	Eq. (3.9) or (3.10)	Directly applicable
Narrow band width, cm^{-1}	< 50	$\leqslant \sim 250$
Number of RTE evaluations	$M = 2$	$N^M = 64, \min N = 8$
Inhomogeneity treatment	CGA	CK approximation

3.4 Implementation of the CK Method

Unlike the SNB models whose parameters are only temperature dependent (at a given wavelength), k-distribution methods require the values of the reordered absorption coefficient that are generally functions of temperature, total pressure, and species mole fraction.

The easiest way to obtain the (reordered) absorption coefficients is to use the inverse Laplace transform applied to the average transmissivity given by the SNB model of Malkmus [98]. The CK method in conjunction with such generated absorption coefficients is referred to as the statistical narrow-band correlated-k (SNBCK) model [82, 125, 128, 129]. For instance, Dembele and Wen [130] suggested a SNBCK scheme based on a 5-point Gauss-Legendre quadrature and on the optimized set of SNB parameters due to Soufiani and Taine [83] containing 43 spectral narrow bands of variable width. This approach was referred to as "FAST CK".

On the other hand, when the SNB based CK methods are employed, intrinsic inaccuracies involved in the SNB model generation are automatically transferred to CK calculations, regardless of the fact whether the SNB model parameters are fitted or definition-derived. Therefore, it seems preferable to construct k-distributions directly from a spectroscopic database.

In the present work, the SNBCK method will thus not be used. The k–g data for CK calculations will be retrieved from the narrow-band k-distribution database due to Wang and Modest [131]. A portable spectral module called Spectral Radiation Calculation Software (SRCS) will be employed.

3.4.1 Narrow-Band k-Distribution Database

Wang and Modest [131] have constructed an accurate and compact database of narrow-band k-distributions for H_2O and CO_2. In this database, the k–g distributions for H_2O are based on and derived from the HITEMP spectroscopic database (an edition prior to

HITEMP2010). The k–g distributions for CO_2 are generated based on the CDSD-1000 data.[4]

The k-distribution data are stored in the database for a variety of pressures (up to 30 bar), temperatures (from 300 to 2500 K, every 100 K), and species mole fractions ($0-1$, every 0.25). In the range $300-4000$ cm^{-1}, a spectral resolution of 25 cm^{-1} is used. In order to obtain an arbitrary gas state k–g distribution, various interpolation schemes in p–T–x space are available. Also, a scalable quadrature scheme (see Table 3.2 below) is realized in the database using a fixed-g concept.

3.4.2 Application of the SRCS

The k-distribution database has been implemented in the SRCS package developed by Pal et al. [133, 134]. The SRCS includes all state-of-the-art k-distribution methods and the LBL method. The source code is available, so that the user is able to run these methods as part of another application. This software is basically aimed for full-spectrum k-distribution-based calculations during the solution of combustion problems. Nevertheless, it can be applied to moderate resolution narrow-band simulations.

In order to use the SRCS in conjunction with JERAD (see Appendix D), which is a narrow-band radiation calculation software program, the narrow-band single-group data retrieval module of SRCS has been improved by declaring new global variables, modifying some functions and subroutines, etc. Since the SRCS is a Fortran-based software package, a C/C++ application programming interface (API) containing "wrapper routines" for the narrow-band data retrieval module has been developed. This API provided coupling between the SRCS and the C-based JERAD code on Linux platforms, thereby ensuring an accurate and robust procedure for obtaining k vs. g distributions from the narrow-band database of Wang and Modest for performing CK calculations.

3.4.3 Quadrature Scheme

The Gauss-Lobatto and Gauss-Legendre quadrature schemes are generally used for the numerical evaluation of the integrals in Eqs. (3.27), (3.34), and (3.47) [82, 83, 135]. The k-distributions in the SRCS database are however tabulated based upon a Gaussian quadrature with the abscissas that are zeroes of the Chebyshev polynomial of the second kind of the n^{th} rank (see [131] for more detail). This quadrature is open at one end ($g = 1$) but closed at the other ($g = 0$). The quadrature is scalable that allows one to choose the number of quadrature points desired for a certain calculation. The number of quadrature points available is 2, 4, 8, 16, etc., with 16 being the minimum number of the points tabulated. The quadrature points and weights are given in Table 3.2.

[4] Recently, Cai and Modest [132] updated the narrow-band k-distribution database by using HITEMP2010, including more species, and increasing the tabulated temperature range up to 4000 K.

Table 3.2: Numerical quadrature points and weights

Abscissas g_i	Weights ω_i			
	$N = 2$	$N = 4$	$N = 8$	$N = 16$
0.000000	0.333333	0.180952	0.094283	0.048112
0.098017	—	—	—	0.099653
0.195090	—	—	0.200357	0.094337
0.290285	—	—	—	0.095898
0.382683	—	0.393464	0.173631	0.088751
0.471397	—	—	—	0.088533
0.555570	—	—	0.171016	0.079680
0.634393	—	—	—	0.077839
0.707107	0.666667	0.247619	0.131113	0.067473
0.773010	—	—	—	0.064227
0.831470	—	—	0.116749	0.052600
0.881921	—	—	—	0.048218
0.923880	—	0.177965	0.067639	0.035639
0.956940	—	—	—	0.030413
0.980785	—	—	0.045212	0.017279
0.995185	—	—	—	0.011348

3.4.4 Samples of k–g Distributions

Figs. 3.5(a) and (b) show examples of k–g distributions for CO_2 and H_2O derived from the database [131] using the SRCS retrieval routines. For the demonstrative purpose, the k–g data are plotted together with the corresponding monochromatic absorption coefficient obtained using the SPECTRA system [122]. The LBL spectra for water vapor were obtained from the same version of the HITEMP spectroscopic database that was applied to the k-distribution generations in [131]. The CDSD-1000 spectroscopic database was used for the carbon dioxide spectrum simulation. A mixture of the first four CO_2 isotopologues with their natural abundance was considered. In the figures, the data are demonstrated for the 16-point quadrature. The 17^{th} point (for which the quadrature weight is zero) is used for the evaluation of the maximum absorption coefficient inside the narrow band.

The k_{mix} vs. g_{mix} distributions for a CO_2–H_2O–air mixture across a part of the 2.7-μm overlapping band (between 3575 and 3725 cm^{-1} every 25 cm^{-1}) are demonstrated in Fig. 3.6. To illustrate the results of using the gas mixture treatment methods (discussed in Section 3.3), the $(k$–$g)_{mix}$ distributions were assembled from the CO_2 and H_2O individual k–g distributions (shown by the red and cyan lines, respectively). The summation approach, Eq. (3.36), and the mixing model, Eq. (3.47), were used. As seen from Fig. 3.6, the k_{mix} computed using Eq. (3.36) is always underestimated at small k-values and overestimated at large k-values when compared to the k_{mix} given by Eq. (3.47).

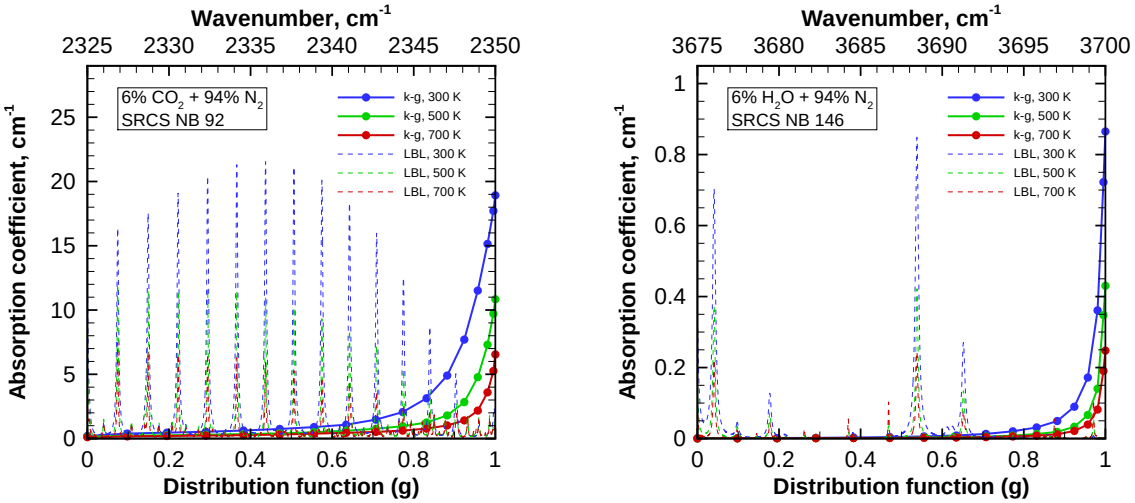

(a) (b)

Figure 3.5: Samples of k vs. g distributions of (a) CO_2 and (b) H_2O derived from the narrow-band single-group k-distribution database of SRCS [131]. The corresponding monochromatic absorption coefficient was computed using SPECTRA Information System [122]. The data are for 6% CO_2 and 6% H_2O in nitrogen at 1 atm and 300, 500, and 700 K

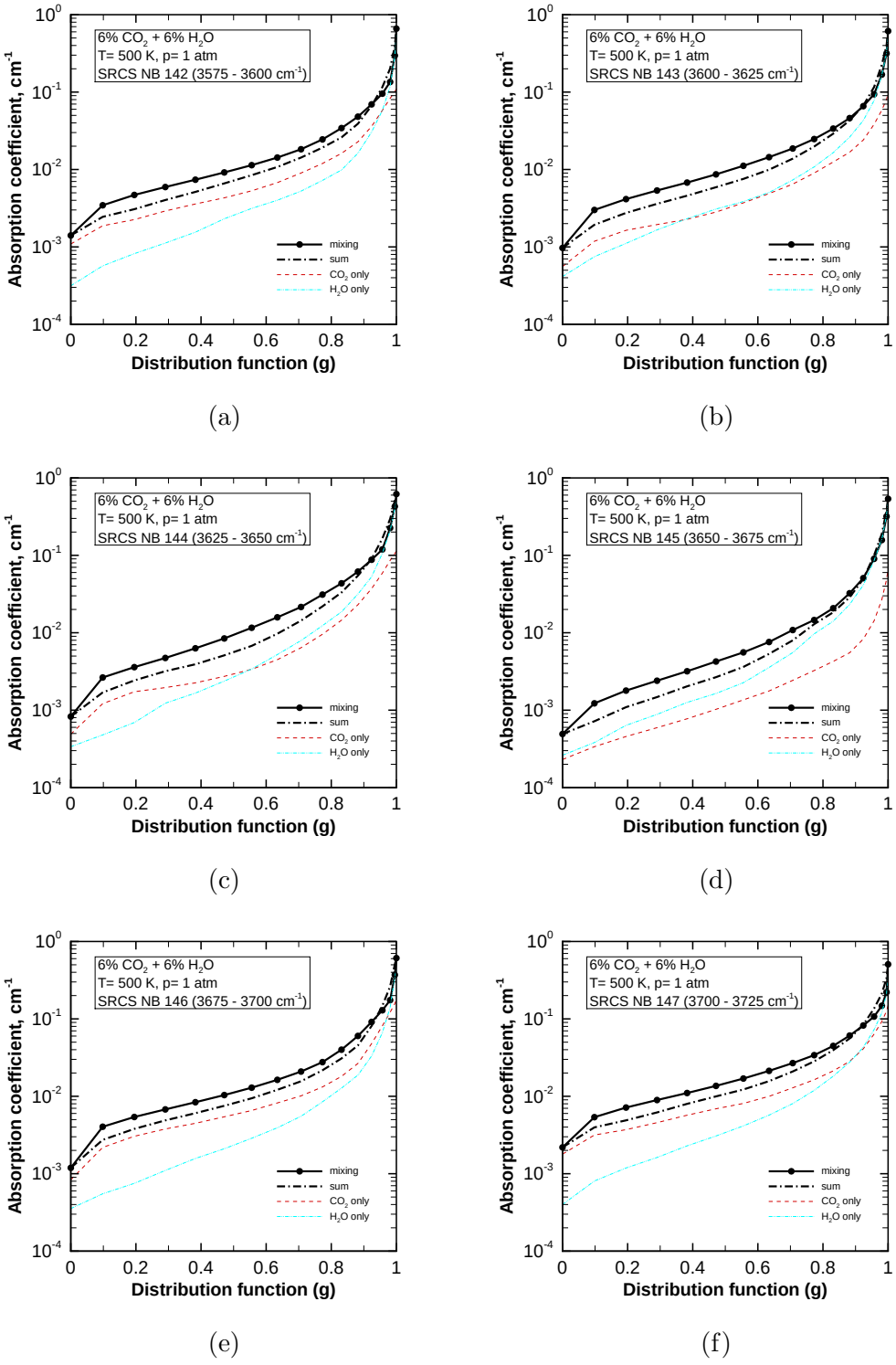

Figure 3.6: k–g Distributions for a CO_2–H_2O–air mixture at 1 atm and 500 K for six 25-inverse-cm-width bands near 2.7 μm: (a) 3575 – 3600 cm^{-1}, (b) 3600 – 3625 cm^{-1}, (c) 3625 – 3650 cm^{-1}, (d) 3650 – 3675 cm^{-1}, (e) 3675 – 3700 cm^{-1}, (f) 3700 – 3725 cm^{-1}. The mixture k–g distributions obtained from the mixing model by Modest and Riazzi are compared with those computed as the sum of k-values of the individual components

3.5 Assessment of the CK Method

The CK method applied to aero-engine plume signature prediction problems has been first investigated by Sventitskiy and Mundt in [136]. Among other things, they demonstrated that the 8-point quadrature scheme (see Table 3.2) results in very minor differences in intensities when compared with the 16-point quadrature. Therefore, the 8-point quadrature scheme will be applied to all CK computations performed in this study.

Within this section, the CK method implemented in the current research will be assessed with respect to accuracy by comparison with exact LBL solutions. The methods for handling overlapping bands will also be evaluated.

3.5.1 1D Test Problem

Since LBL computations of entire exhaust plumes are prohibitive, a 1D test problem is suggested here. In this test problem, the spectral radiance leaving a single LOS passing through the plume of a typical medium-bypass turbofan engine with a mixed exhaust is calculated. The LOS of length 1.06 m consists of 54 isothermal and homogeneous slabs with total pressure, temperature, and CO_2 and H_2O mole fraction distributions shown in Fig. 3.7. The radiance values are computed at $L = 0$ m.

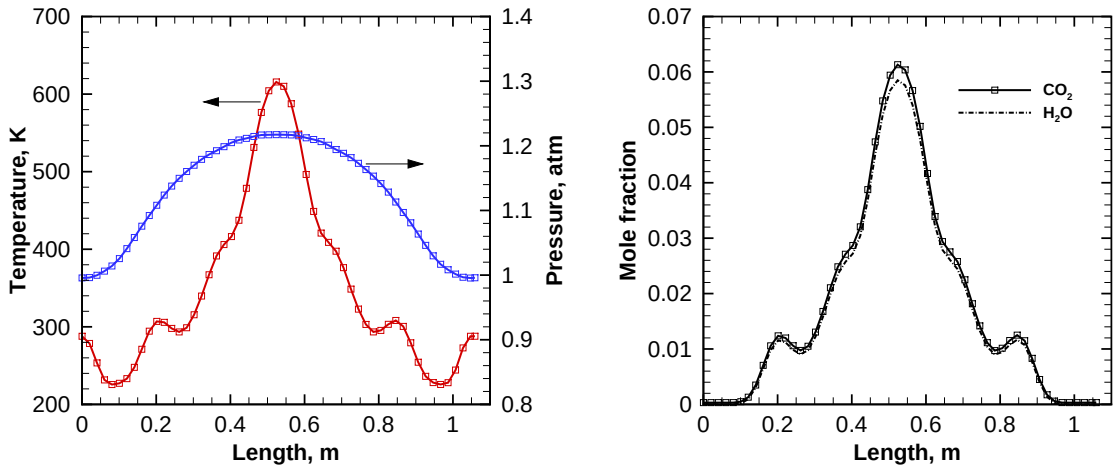

Figure 3.7: Distributions of temperature, pressure, and species mole fractions along LOS in the 1D test problem

3.5.2 LBL Reference Data

The LBL solutions for the spectral radiance along the LOS are presented in Fig. 3.8 (which depicts high-resolution radiance spectra for the 6.3-μm band of H_2O, 4.3-μm band of CO_2, and 2.7-μm band of CO_2/H_2O). Two types of spectra can be seen in the figure, namely the synthetic spectrum and the convoluted spectrum. The latter was obtained by using a rectangular slit function with a width of 25 cm^{-1} to allow comparisons with CK results. Note that the LBL calculations were carried out using the monochromatic absorption coefficients computed by means of the LBL routines of the SRCS package. The same routines had been applied to construct the k-distribution database [131].

3.5.3 Comparison with LBL Solutions

Fig. 3.9 compares the CK and LBL results. For the H_2O 6.3-μm band and the CO_2/H_2O 2.7-μm band the error determined as

$$\text{Error } \% = 100 \times \frac{I_{\eta,\text{CK}} - I_{\eta,\text{LBL}}}{I_{\eta,\text{LBL}}} \tag{3.48}$$

is less than 10%. For the CO_2 4.3-μm band, the error is somewhat greater than 50% near the band center. The use of the 16-point quadrature scheme (denoted as CK16 in Fig. 3.9) reduces the error up to approximately 30%.

In realistic IR signature problems, however, significant errors produced by the CK method near the CO_2 4.3-μm band center are unimportant. In the 4.3-μm band, the cold CO_2 absorption is extreme in the band center, but it is transparent in the wings of the hot CO_2 radiation within the spectral regions 2212.5 – 2337.5 and 2362.5 – 2412.5 cm^{-1} (the so-called "red spike" and "blue spike", respectively) [15, 118]. The CO_2 emissions from the band wings are therefore transmitted through the atmosphere and they can be measured experimentally. This implies that rather the band wing spectral regions are of interest where the CK method yields fairly accurate results (for moderately inhomogeneous media as in Fig. 3.7).

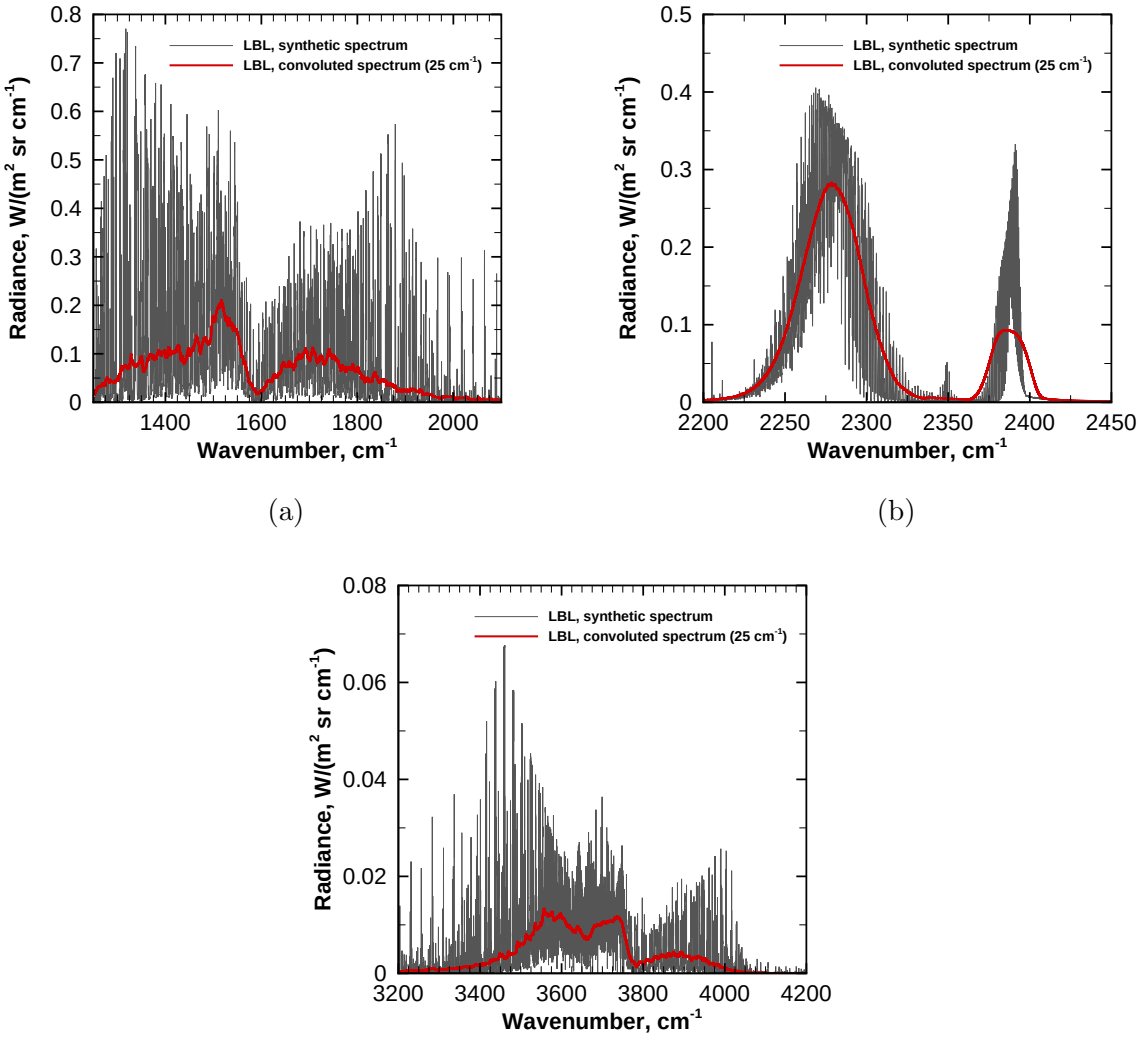

Figure 3.8: LBL solutions for the 1D test problem in the spectral regions (a) 1250 – 2100 cm^{-1} (6.3-μm band of H_2O), (b) 2200 – 2450 cm^{-1} (4.3-μm band of CO_2), and (c) 3200 – 4200 cm^{-1} (2.7-μm band of CO_2/H_2O)

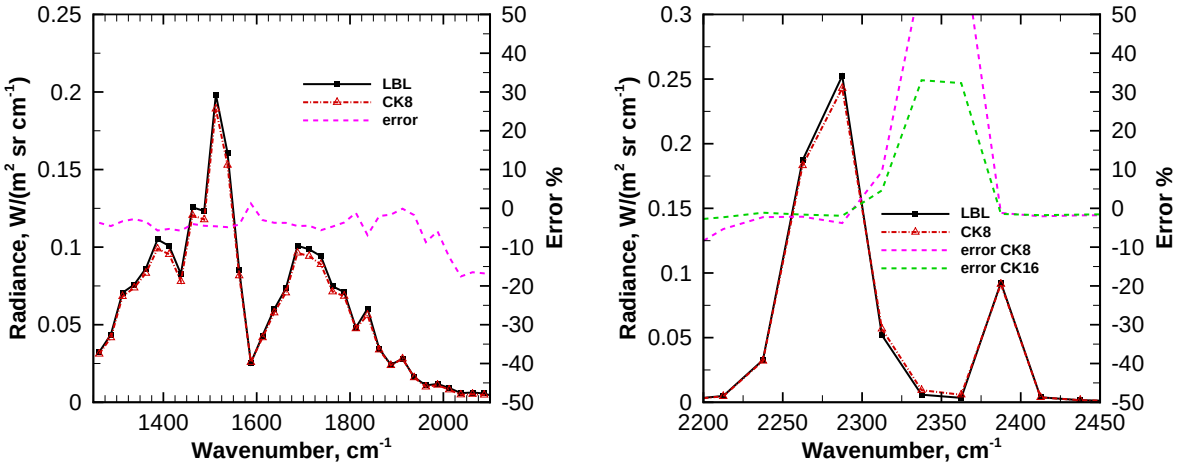

(a) (b)

(c)

Figure 3.9: Comparison of CK and LBL solutions for the 1D test problem in the spectral regions (a) 1250 – 2100 cm^{-1} (6.3-μm band of H_2O), (b) 2200 – 2450 cm^{-1} (4.3-μm band of CO_2), and (c) 3200 – 4000 cm^{-1} (2.7-μm band of CO_2/H_2O)

3.5.4 Treatment of the 2.7-μm Overlapping Band

In Fig. 3.9(c), the CK spectral radiances have been computed using the "exact" direct integration approach, Eq. (3.34). Fig. 3.10 shows the comparison between those radiance values and the values computed by the summation approach and the mixing model due to Modest and Riazzi, Eqs. (3.36) and (3.47).

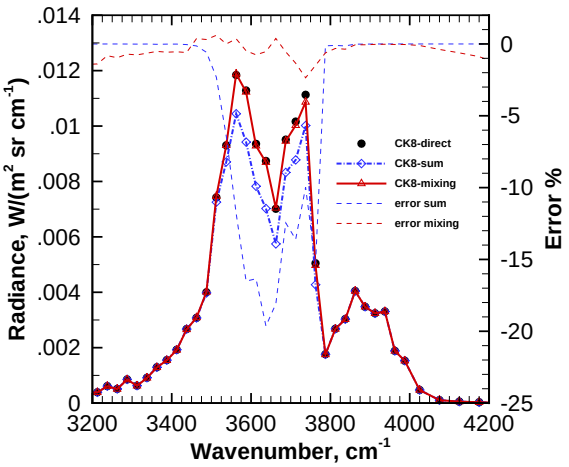

Figure 3.10: Spectral radiances in the 2.7-μm region leaving the LOS in the 1D test problem computed using various models for gas mixtures

The comparison reveals that the summation approach, which is rather theoretically unsound, results in significant errors (up to 20%) when compared to the basic direct approach. The mixing model results agree well with those given by the direct approach (maximum error limited to less than 2.5%). Therefore, the mixing model of Modest and Riazzi will be used to treat gas mixtures in all plume IR emission simulations that will be performed in Chapters 5 and 6 (and also in Appendix B).

3.6 Gray-Band Approximations

Gray-band models, unlike the SNB models and the CK method, approximate the complicated spectral behaviour of the absorption coefficient across a narrow band by means of the use of a single gray-gas value, $\bar{\kappa}$. A number of such models utilizing the local absorption coefficient have been proposed by Liu et al. [137].

Two gray narrow-band models called correlated-k gray (CKG) and statistical narrow-band gray (SNBG) are suggested in the present study.[5] These models also use the local gas properties to estimate the local average absorption coefficient, but they differ from the models developed in the work [137] with respect to the averaging method.

[5]The terms CKG and SNBG were introduced for the first time in the author's work [138].

3.6.1 The CKG Model

The CKG model is based on narrow-band k–g distributions. The average absorption coefficient for a mixture of gases is calculated as

$$\bar{\kappa}_{mix} = \sum_{i=1}^{N} \omega_i k_{mix}(g_i), \tag{3.49}$$

where $k_{mix}(g_i)$ is the linear absorption coefficient (expressed in cm^{-1}) in the mixture k–g distribution, ω_i is the corresponding quadrature weight, and N is the number of quadrature points.

3.6.2 The SNBG Model

For a gaseous mixture comprising M species, the narrow-band average absorption coefficient given by the SNBG model is

$$\bar{\kappa}_{mix} = p \sum_{i=1}^{M} x_i \bar{k}_i, \tag{3.50}$$

where $\bar{k}_i = \bar{S}_i/\bar{\delta}_i$ is the ratio of the mean line strength to the mean line spacing for each species denoted by the subscript i, p is the total pressure, and x is the species mole fraction. The quantity $\bar{k}$ is one of the SNB model parameters. A very similar approximation was also introduced by Surzhikov in his paper [101].

The advantage of the gray narrow-band models is that they permit only one solution of the RTE for every narrow band, whereas the CK method requires N solutions (provided that k-distributions for the mixture are precalculated). Like CK (but not SNB), these models can be used with an arbitrary RTE solution method. However, both the CKG and SNBG models fall into the WLA category, as seen by comparing with Eq. (3.8).

3.7 Radiative Properties of Particles

Particles of primary interest in exhaust plumes are generally carbon (or soot) and aluminium oxide (Al_2O_3) [1, 15]. Soot particles may be formed in plumes (or, more specifically, in fuel-rich parts of flames) as a result of incomplete combustion of hydrocarbons. The particles of Al_2O_3 are produced by combustion of solid propellants loaded with metallic powdered aluminium. Particulate radiation can have a considerable impact on the IR characteristics of the plume.

The main focus of the present work is on the numerical simulation of thermal radiation from airbreathing jet engine plumes (as discussed further in Chapters 5 and 6). While

Al_2O_3 particles are associated with solid rocket motor exhaust plumes, aero-engine exhausts often contain soot particles. Therefore, the consideration of radiative properties of solid particles is limited to the properties of small particles such as soot. This, of course, does not influence too strongly the mathematical model and computer code for plume signature predictions developed within this study. If it is needed, the radiative properties of any particles can be incorporated in the code without loss of generality. The analytical expressions commonly used to approximate the scattering phase function are discussed in more detail.

3.7.1 Rayleigh Scattering

Rayleigh scattering holds for particles small enough that the particle size parameter $x = 2\pi a/\lambda$, where a is the particle radius, is close to zero. In the limit of $x \to 0$ the particle absorption coefficient is [23]

$$\kappa_{p\eta} = \frac{36\pi nk}{(n^2 - k^2 + 2)^2 + 4n^2k^2} f_v \eta, \tag{3.51}$$

where f_v is the particle volume fraction, n and k are, respectively, the real part (refractive index) and the imaginary part (absorptive index) of the complex index of refraction, $m = n - ik$. The value for the absorption coefficient does not depend on particle size distribution, but only on f_v.

It is straightforward to show that the particle scattering coefficient can be evaluated as

$$\sigma_{s\eta} = 4\pi \frac{36n^2k^2 + \left[(n^2 - k^2 - 1)(n^2 - k^2 + 2) + 4n^2k^2\right]^2}{\left[(n^2 - k^2 + 2)^2 + 4n^2k^2\right]^2} x^3 f_v \eta, \tag{3.52}$$

where a mean particle radius $\bar{a}$ is assumed for the x value.

It can clearly be seen by comparing the equations given above that $\sigma_{s\eta}/\kappa_{p\eta} \propto x^3$. Since $x \ll 1$, it follows that $\sigma_{s\eta} \ll \kappa_{p\eta}$, i.e. scattering may be neglected as compared with absorption leading to $\beta_\eta \approx \kappa_\eta$.

3.7.2 Optical Properties of Soot

Soot particles are mostly spherical in shape and their size is generally small, ranging in diameter from 5 to 80 nm [23]. For jet engine exhaust plumes, the soot particle diameters of 10 to 22 nm [139] and 30 to 60 nm [140] have been reported. Therefore, in the IR spectral range, the particles of soot fall into the Rayleigh scattering regime obeying Eq. (3.51) for the absorption coefficient.

Soot strongly emits thermal radiation in a continuous spectrum over the IR region [23]. A very considerable amount of attention has thus been given to soot optical constants (see [23] and references therein). The correlations developed by Chang and Charalampopoulos [141] are used in the present study to model radiation from nongray absorbing particles. They define the values of n and k for flame soot as follows:

$$n = 1.8110 + 0.1263 \ln \lambda + 0.0270 \ln^2 \lambda + 0.0417 \ln^3 \lambda, \tag{3.53a}$$

$$k = 0.5821 + 0.1213 \ln \lambda + 0.2309 \ln^2 \lambda - 0.0100 \ln^3 \lambda, \tag{3.53b}$$

where the wavelength λ is in μm. The expressions are valid for the wavelength range $0.4\,\mu\text{m} \leqslant \lambda \leqslant 30\,\mu\text{m}$.

3.7.3 Scattering Phase Function

The phase function Φ describes how radiation energy is redistributed in angular directions when scattering by particles occurs. The ratio $\Phi(\vec{s}', \vec{s}) d\Omega / 4\pi$ can be interpreted as the probability that radiation propagating in the direction $\vec{s}'$ and confined within the solid angle $d\Omega'$ is scattered through the angle $\Theta = \arccos(\vec{s}' \cdot \vec{s})$ into the solid angle $d\Omega$ around the direction $\vec{s}$. The scattering phase function should therefore satisfy

$$\frac{1}{4\pi} \int_{4\pi} \Phi(\vec{s}', \vec{s}) \, d\Omega = 1. \tag{3.54}$$

Eq. (3.54) is known as the normalization condition. It simply claims that the radiation in the direction $\vec{s}'$ will be scattered into the solid angle of 4π with probability 1 [48].

Scattering is classified into two categories. These are isotropic and anisotropic scattering. Isotropic scattering occurs if energy is scattered equally into all directions. In this case, the scattering phase function is independent of the scattering angle Θ, or

$$\Phi(\mu) = 1, \tag{3.55}$$

where $\mu \equiv \cos \Theta$.

The most comprehensive approach to treat the anisotropy of scattering is to use the complicated Mie scattering theory. This was done by Trivic et al. [142] who coupled Mie equations for the evaluation of scattering phase function with the FVM for radiative transfer predictions in a 2D rectangular enclosure.

The scattering phase functions derived from Mie theory, however, may undergo strong angular oscillations which are somewhat inconvenient for radiation analysis. In order

that this problem be addressed, several approximate anisotropic phase functions have been suggested over the years. These approximate phase functions represent the exact (Mie-scattering) phase functions by simpler expressions while retaining their anisotropic characteristics.

In particular, the phase function for Rayleigh scattering is

$$\Phi(\mu) = \frac{3}{4}(1 + \mu^2). \tag{3.56}$$

The Rayleigh phase function is symmetric with respect to forward and backward scattered intensities.

For large particles with strong forward-scattering peaks, such as Al_2O_3, many authors (see, e.g., [21, 143]) have used the Henyey-Greenstein phase function,

$$\Phi(\mu) = \frac{1 - \bar{\mu}^2}{(1 + \bar{\mu}^2 - 2\bar{\mu}\mu)^{3/2}}, \tag{3.57}$$

in which the average cosine of the scattering angle $\bar{\mu}$, known as asymmetry factor, is the only measure of the scattering anisotropy, $-1 \leqslant \bar{\mu} \leqslant 1$. The asymmetry factor is positive when forward scattering dominates and negative when backward scattering dominates. If $\bar{\mu} = 0$, then the medium is isotropic. Fig. 3.11 shows the Henyey-Greenstein phase function for $\bar{\mu} = 0.5$ and $\bar{\mu} = 0.86$ in comparison with phase functions for Rayleigh and isotropic scattering.

In most problems, an arbitrary scattering phase function can be represented by a series of Legendre polynomials P_n with argument μ [48],

$$\Phi(\mu) = 2\bar{\mu}\delta(1 - \mu) + (1 - \bar{\mu}) \sum_{n=0}^{\infty} (2n + 1) b_n P_n(\mu), \tag{3.58}$$

where the forward-scattering peak is treated separately (the so-called delta-Eddington approximation). In Eq. (3.58), δ is the Dirac delta function and b_n are the expansion coefficients.

An example of treatment of general Mie-anisotropic phase functions by Legendre polynomial expansions can be found in the work by Kim and Lee [144] who proposed four approximate phase functions for some particle size parameters and complex indices of refraction. These scattering phase functions are designated as F1, F2, B1, and B2 (where the letters F and B indicate that the phase function has peak values in forward and backward directions, respectively), and they are widely used in the literature to examine the effects of anisotropic scattering [54, 60, 76, 142, 145].

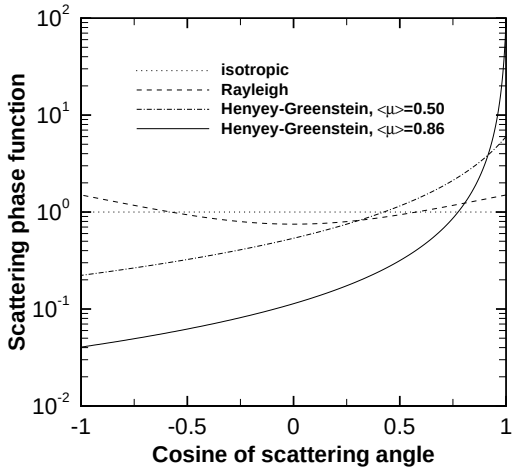

Figure 3.11: Comparison of Henyey-Greenstein, Rayleigh and isotropic scattering phase functions

3.8 Summary

In this chapter, narrow-band methods for modeling of the spectral radiative properties of molecular gases and particles have been considered. The "classical" SNB models, which provide the average gaseous column transmissivity, were first overviewed. This included giving consideration to the formulations of Goody and Malkmus, their extension to the Voigt line broadening regime, and the CGA for the treatment of inhomogeneous paths. The transmissivity multiplication property commonly used together with the SNB models for handling gaseous mixtures has been presented. The narrow-band k-distribution method formulating the gas radiative properties in terms of the reordered absorption coefficient was considered next. Two approaches used to address medium inhomogeneity, namely the scaled-k and correlated-k assumptions, were explained in detail. The CK model was chosen to be employed in the present research as the basic narrow-band model. Multicomponent gas mixture treatment methods used together with the CK model, such as the direct integration approach, the summation approach, and the mixing model originally developed by Modest and Riazzi, were mathematically substantiated and derived. Principal differences between the SNB models and the CK method were summarized. Details of the CK method implementation were outlined and examples of k–g distributions were given. The CK method has been assessed by comparing its results with exact LBL solutions for a single LOS passing through a typical turbofan engine plume. It was shown that the CK method yields the results with about 10% accuracy when compared to the reference LBL solutions (except for the center of the CO_2 4.3-μm band). It was also demonstrated by performing computations in the CO_2/H_2O 2.7-μm band region that the mixing model of Modest and Riazzi results in essentially no error in spectral radiance. Furthermore, the CKG and SNBG models were suggested. These models approximate the complicated spectral behaviour of the realistic absorption coefficient across a narrow band by using an average absorption coefficient

value calculated based on local gas properties, thereby decreasing the number of RTE evaluations required. And finally, the radiative properties of soot and anisotropic scattering phase functions, such as the Henyey-Greenstein phase function, were presented and analysed.

Chapter 4

Turbofan Engine Exhaust Plume

4.1 Introduction

In the present work, the exhaust jet of a realistic turbofan engine mounted on high speed subsonic aircraft is considered as an emitting plume. It is typical for such engines that the hot core flow is mixed with the cold bypass flow such that increased thrust and reduced acoustic noise are achieved. After being mixed by a forced mixer the flow is expanded through a common nozzle [146–149].

In order to predict IR radiation originating from a participating medium such as an exhaust plume, the distribution of gas-dynamic properties through the medium should first be known, particularly static temperature and partial pressures of all species. In the case of an exhaust plume at low altitude, the flow field modeling and the IR emission prediction are two different, non-connected issues.

In principle, the temperature and species fields in the plume can be obtained from calculations based upon a variety of approaches. While concentrating on radiation phenomenon modeling, it is not unusual for some investigators to be, however, very approximate in modeling the plume flow. The division of a flow field into several coaxial cylinders [25], within each of which the medium is assumed to be homogeneous and isothermal, is an example of non-physical treatment for plume gas dynamics.

The lobed forced mixer makes the plume flow highly complex and essentially three-dimensional. It is obvious that neither simplified jet flow models [41, 46, 150] nor 2D simulations [5, 28] are appropriate for this particular jet flow. Approximate methods are unable to capture many important flow features such as vortex structures downstream of the mixer and, if present, shocks. This, in turn, deteriorates the radiation prediction accuracy. Therefore, 3D CFD modeling has been performed in order to estimate the plume flow accurately. The commercial Reynolds-averaged Navier-Stokes (RANS) solver ANSYS FLUENT [151] was used.

In the following sections, relevant details of the CFD modeling are outlined. The composition of the atmosphere and the exhaust gas composition are discussed. The temperature, pressure, and species concentration fields in the exhaust plume needed for thermal radiation predictions are presented and analysed.

4.2 CFD Simulation with ANSYS FLUENT

4.2.1 Engine Operation Point

The maximum take-off (MTO) phase is the most vulnerable event against the IR threat for civil airliners [9]. This operation point is therefore preferred to other phases of flight, such as cruise, with respect to thermal radiation modeling.

A realistic case of turbofan operation, which corresponds to MTO conditions, is simulated in order to provide the distribution of thermophysical properties throughout the exhaust plume for subsequent IR signature predictions. The ambient and engine operating conditions at MTO are given in Table 4.1.[1]

Table 4.1: Ambient and engine operating conditions at MTO

Parameter	Value
Free stream	
Altitude, m	333.4512
Mach number	0.239
Ambient pressure, Pa	97381.59
Ambient temperature, K	295.98
Fan flow (cold)	
Total pressure, Pa	168321.78
Total temperature, K	351.7
Core flow (hot)	
Total pressure, Pa	150560.87
Total temperature, K	864.6

[1]The free stream conditions presented in Table 4.1 are those kept in flight that is hold in the International Standard Atmosphere (ISA) (see, e.g., [152, 153] and references therein) at a given altitude when the ground level temperature is assumed. The present case corresponds to ISA + 10° day, i.e. the ground level temperature is 298.15 K.

4.2.2 Grid System

The computational domain adopted for the CFD simulation of the plume flow is similar to that used in the work by Saegeler [148], but with an extended length of approximately $10\,d_j$, where $d_j = 0.875$ m is the jet diameter taken to be equal to the nozzle exit diameter. Due to geometric reasons, a sector of 90 degrees has been considered. The domain was meshed with a block-structured grid containing about 16 million cells. The grid is shown in Fig. 4.1.

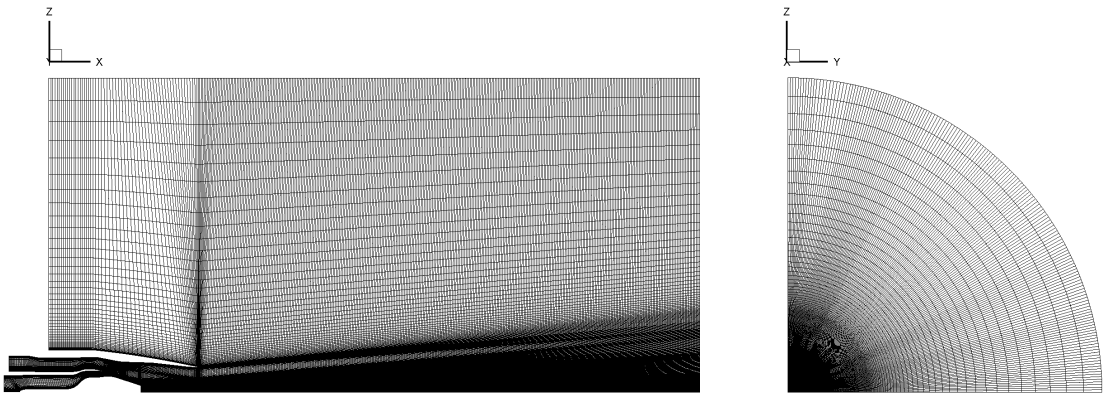

Figure 4.1: Block-structured grid used in the plume flow simulation

4.2.3 Boundary Conditions

Boundary conditions specified at the boundaries of the flow domain are of the following types. At the flow inlets, namely core, fan, and free stream (Fig. 4.1), pressure inlet boundary conditions were applied. The corresponding total pressure and total temperature values are given in Table 4.1. A pressure outlet boundary condition was used at the outlet boundary at $x = x_{max}$, where the specified static pressure is equal to the ambient pressure. The outer circular boundary was defined as a characteristic (pressure far-field) boundary with the free stream static conditions from Table 4.1. The two side boundaries of the domain were treated as periodic boundaries. All other boundary conditions were set as no-flow (wall). Finally, for species transport calculations, mole fractions of species constituting the exhaust gas and air were specified at the corresponding boundaries. Tables 4.2 and 4.3 below summarize the air composition and the exhaust gas composition, respectively. The interested reader is also referred to the work [148] for further details on boundary conditions used for the definition of CFD problems for jet flows from turbofans.

4.2.4 Solver Settings

The steady-state RANS solution for the jet flow was obtained by using the ANSYS FLUENT pressure-based segregated solver [154]. The second-order upwind scheme was chosen for the convection terms in all discretized transport equations. The SST $k-\omega$ turbulence model was used with the default values assigned to the model constants. In particular, the values for the turbulent Prandtl and Schmidt numbers were 0.85 and 0.7, respectively. The flow was assumed to be nonreacting (transport of passive scalar species).

4.2.5 Calculation Sample

Fig. 4.2 shows the distribution of static temperature in the symmetry plane as calculated with ANSYS FLUENT for the entire domain including the engine inner flow. However, only a part of the overall flow solution is needed for plume radiation analysis. The necessary data on plume thermophysical properties required to calculate IR emissions should therefore be extracted from the CFD solution obtained over the entire flow domain. This procedure and respective flow fields used as input for radiation calculations are discussed separately in Section 4.4.

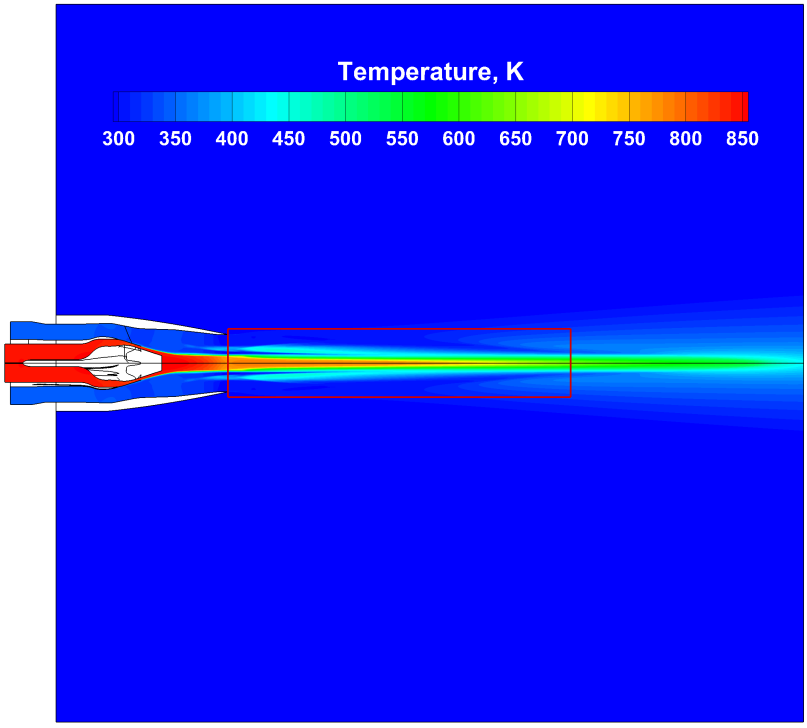

Figure 4.2: Distribution of static temperature in the CFD domain and the computational domain adopted for radiation predictions

4.3 Air and Exhaust Gas Compositions

4.3.1 Air Composition

The atmospheric model profiles, such as tropical, mid-latitude summer, mid-latitude winter, sub-arctic summer, sub-arctic winter, etc. [155], specify atmospheric radiance and transmittance which varies for different models through various concentrations of species. This affects the plume IR emission transmitted through the atmosphere and perceived by a detector [156].

Plume intrinsic radiation is predicted in this work, as discussed further in Section 5.1. However, the air composition should be specified carefully because the combustion products, e.g., H_2O, CO_2, and CO, are also atmospheric constituents.

The model adopted in the work assumes the air composition which corresponds to mid-latitude summer at zero altitude. The air constituents are eight principal gases encountered in the earth's atmosphere. The composition of air is presented in Table 4.2.

Table 4.2: Gaseous composition of air

Species	Symbol	Amount (ppmv)
Nitrogen	N_2	774134.01
Oxygen	O_2	207661.12
Water vapor	H_2O	17810
Carbon dioxide	CO_2	392.6
Carbon monoxide	CO	0.15
Others	$CH_4 + N_2O + O_3$	2.1242

The atmospheric constituents with very trace amount, like nitric oxide (NO), sulphur dioxide (SO_2), nitrogen dioxide (NO_2), etc. [110, 157], are not considered in the model. The noble gases are not taken into account as well. Consequently, the model dry air constituents are, in order of decreasing concentration, nitrogen (N_2), oxygen (O_2), carbon dioxide (CO_2), methane (CH_4), nitrous oxide (N_2O), carbon monoxide (CO), and ozone (O_3). Note that, in the dry air, the latter five molecules are the most radiatively active [155, 158], whereas nitrogen appears as only a trace spectral contributor [155].

The atmospheric model profiles mentioned above are mainly specified by water vapor. The atmospheric concentration of H_2O varies widely in space and time, typically within the range 0-4% by volume [158, 159]. The concentration of CO_2 can also vary by season and location, but not as much as for water vapor [158].

In Table 4.2, the H_2O concentration was calculated by means of a realistic relative humidity value obtained for a summer day in the Airport of Krasnodar (45°N), Russia.[2]

[2] July 19, 2012, 10 a.m., 24.9°C, 759.5 Torr, RH 56% at altitude of 2 m. Weather archive in Krasnodar (airport). http://www.rp5.ru/.

The CO_2 molecule concentration value is based on the annual mean data for 2012.[3] The CO value was taken from the MODTRAN report [155].

4.3.2 Exhaust Gas Composition

The well-known CEA code [160] was used to obtain a chemically equilibrium composition of combustion products. Jet A kerosene-type fuel was chosen for this particular combustion problem at assigned pressure of 25 atm (pressure inside combustor). The fuel injection temperature was taken to be equal to the ambient temperature. The oxidant was air at 778 K with the composition given in Table 4.2. When performing the simulation, the air/fuel mass ratio of 44 was assumed (lean mixture).

The species mole fractions in the exhaust gas are summarized in Table 4.3. Note that, according to measurements [161], the realistic CO value encountered in aircraft engine exhausts is significantly higher than that given in the table. This is a consequence of the chemical equilibrium assumption involved in CEA.

Table 4.3: Composition of exhaust gas

Species	Symbol	Mole fraction
Nitrogen	N_2	0.7566
Oxygen	O_2	0.1349
Water vapor	H_2O	0.0612
Carbon dioxide	CO_2	0.0461
Carbon monoxide	CO	0.1951×10^{-6}
Others	$NO_x + N_2O + O_3$	1.1429×10^{-3}

4.4 Plume Flow Field

The objective of the present work is numerical modeling of plume intrinsic IR emissions. As such, the plume is considered to be isolated from other sources of radiation such as exhaust arrangement, turbine blades, etc. In order to allow radiative transfer to be simulated solely within the plume medium, a separate computational domain for 3D radiation modeling was adopted.

A sketch of the radiation domain is shown in Fig. 4.2 by the red box. The domain has a length of $6.0\,d_j$, where $d_j = 0.875$ m, to fully occupy the region of the jet potential core that emits the bulk of the plume radiation. In the directions perpendicular to the jet axis, i.e. in the y and z coordinate directions, the domain has an equal length of $1.2\,d_j$.

[3] P. Tans, NOAA/ESRL, and R. Keeling, Scripps Institution of Oceanography. Trends in atmospheric carbon dioxide. www.esrl.noaa.gov/gmd/ccgg/trends/.

CFD solutions for temperature, pressure, and concentration of each species in the plume, but not in the entire flow domain, are of interest. These properties were obtained by performing a linear interpolation from the CFD grid onto a 3D Cartesian grid used in radiation calculations. The radiation domain discretization will be discussed further in Section 5.2.

The distributions of static temperature and static pressure within the plume are shown in Fig. 4.3, whereas the distributions of mole fractions of CO_2 and H_2O, which are the most dominant radiatively active species in the exhaust gas (see Table 4.3), are demonstrated in Fig. 4.4. The plume thermophysical properties shown are those after performing the interpolation. It is worth noting that pressure is intentionally in atm rather than in Pa. The standard atmosphere (atm) is a more convenient unit for radiative transfer applications. Also note that the species fields are more diffusive than the temperature field due to the difference in the turbulent Prandtl and Schmidt numbers (see p. 64). The temperature, pressure and species profiles as shown in the figures will be used as input data for plume IR radiation predictions that shall be discussed in Chapters 5 and 6.

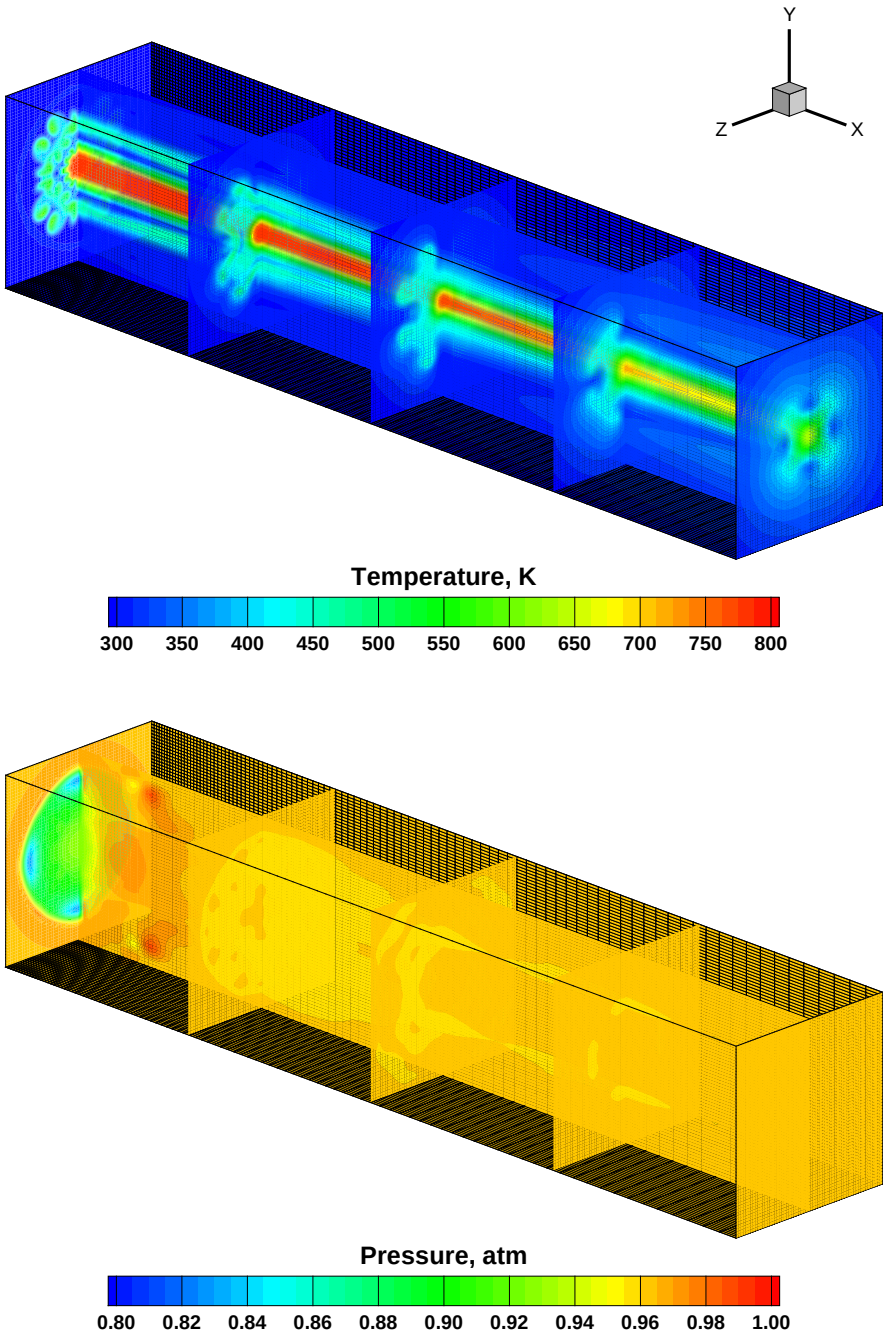

Figure 4.3: Static temperature and pressure distributions in the plume

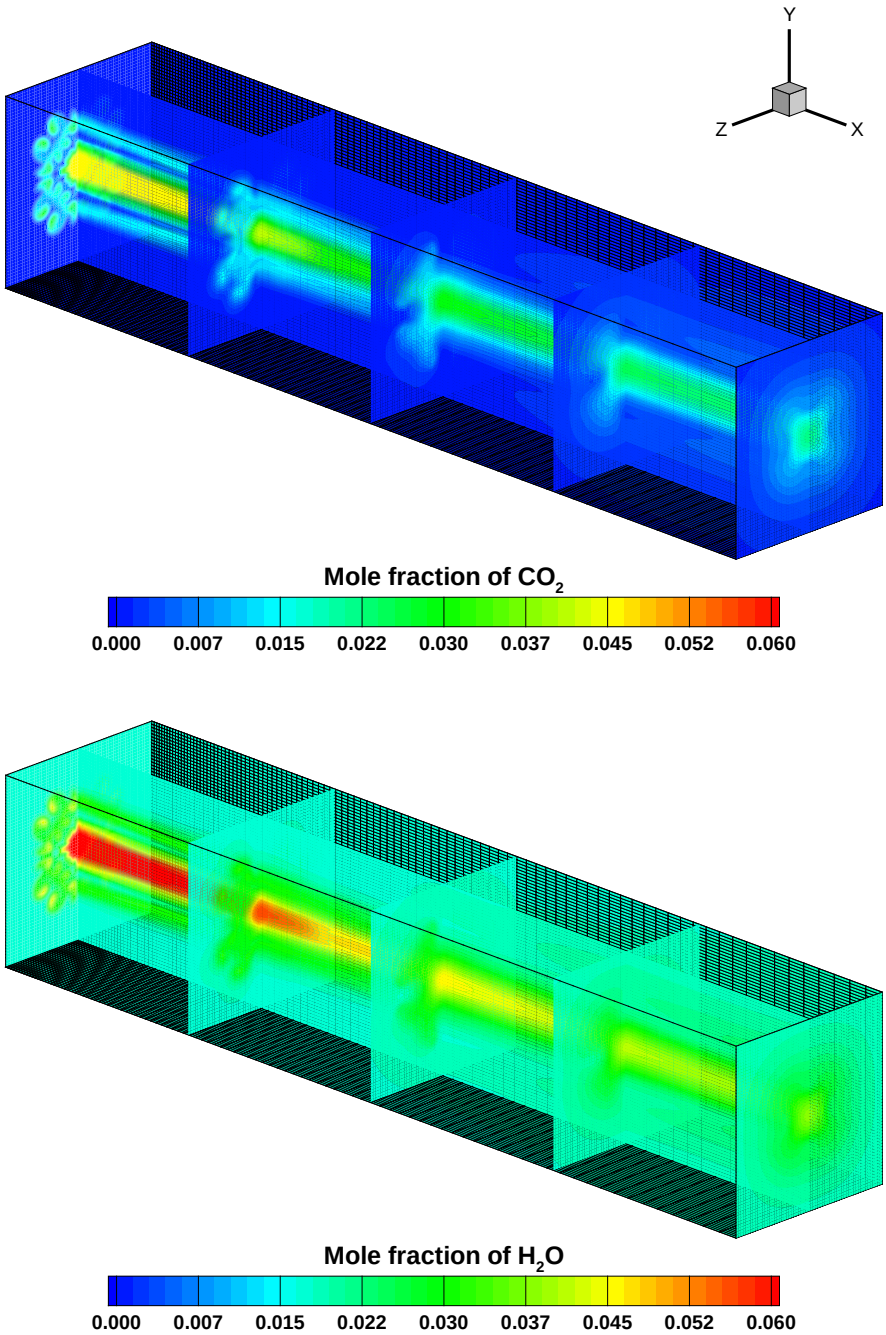

Figure 4.4: Mole fraction distributions of CO_2 and H_2O in the plume

4.5 Summary

In this chapter, a particular emphasis was placed on plume flow field modeling. The exhaust plume of a real-life turbofan equipped with a forced mixer was simulated numerically using the commercial CFD software ANSYS FLUENT. This simulation has allowed the description of a true physical pattern of temperature and species distributions in the plume, thus providing accurate input parameters for the subsequent IR radiation calculations.

Chapter 5

Gaseous Exhaust Plume IR Emission Simulations

5.1 Introduction

Predictions of thermal radiation from exhaust plumes fall into two categories dependent upon whether the distance between the plume and an observer (such as a ground-based IR detector or a seeker head of an IR-guided missile) is short or long. If the observer is located close to the plume, a detailed modeling that takes account of observer's field of view and its orientation and location with respect to the plume has to be carried out [5, 162]. For long-range applications, the entire plume is effectively viewed from an infinite distance [26]. All lines-of-sight through the plume are then parallel. For the purposes of this chapter it is assumed that the plume is observed from an infinite distance.

Due to space limitations it is beyond the scope of the present research to deal with the plume IR radiation transmitted through the intervening atmosphere [156]. For all cases studied within the framework of the work, the medium between the plume and the observer is treated as radiatively nonparticipating.[1] Factors such as radiation from inner jetpipe walls and turbine blades, background sky emission, sunshine, etc., are not taken into account. Consequently, the only considered phenomenon in this thesis is the intrinsic (source) radiation of the plume.

The following sections seek to present and analyse the results of numerical simulations of IR emissions from the exhaust plume of a typical full-scale turbofan engine considered

[1]The JERAD software (see Appendix D) has an option which permits inclusion of isothermal atmospheric paths into overall radiation transport pattern. Either spectrally correlated or uncorrelated approaches can be used. The option is currently available for SNB calculations. One should however recognise that neither SNB nor CK models are accurate enough for remote sensing applications [83]. For such problems, the statistical narrow-band fictitious gas (SNBFG) [105] and correlated-k fictitious gas (CKFG) [135, 163] models provide an accurate estimation of radiation from hot gas through a long cold path.

previously in Chapter 4. In order to better validate the FVM, which is suggested in the current work for solving plume radiation problems, the simulations within this chapter are performed for purely gaseous exhaust. The results of computations of IR signatures from the plume with nonscattering/scattering particles will be considered in the next chapter.

In what follows, the 8-point quadrature scheme with the quadrature weights given in Table 3.2 is applied in all computations using the CK method. A hybrid interpolation in 3D p–T–x space[2] is used to retrieve narrow-band k–g distributions for arbitrary gas states that are not contained in the database of SRCS. The mixture of combustion products with air is treated by utilizing the narrow-band mixing model by Modest and Riazzi.

The definitions of the IR radiative properties used hereafter to assess radiation from the plume can be found in Appendix A.

5.2 Simulation Setup

5.2.1 Definition of Observation Angles

It is typical for plume IR signature prediction problems that the plume position relative to an observer is described by the aspect angle which is defined as an angle between the plume centerline and LOS (see, e.g., [1]). The plume examined in the current work is nonaxisymmetric. The plume emission direction is therefore specified by two angles, namely the aspect angle θ and the roll angle φ (Fig. 5.1). The θ angle is measured from the plume centerline (x-axis), whilst the φ angle is measured from the y-axis.

The angle definitions are identical to those used for the angular space discretization in the FVM (as described in Section 2.5, p. 18). In this notation, the aspect and roll angles are equivalent to the zenith and azimuth angles, respectively. By definition, control solid angles do not vary with the observation angles when carrying out FVM computations. All results presented below in this chapter were obtained with varying θ at $\varphi = 90°$.

5.2.2 Computational Domain Discretization

Regardless of the RTE solver used, the rectangular domain introduced in Chapter 4 has to be spatially discretized. It should however be understood that the purpose of this discretization is fundamentally different for the RT solver and for the FVM solver.

The RT technique provides the plume IR emission in a particular direction by performing RTE integration along many lines-of-sight through the plume. Thus, the spatial domain

[2]The hybrid interpolation scheme implies a bilinear interpolation in pressure–mole fraction space and a spline interpolation in temperature space.

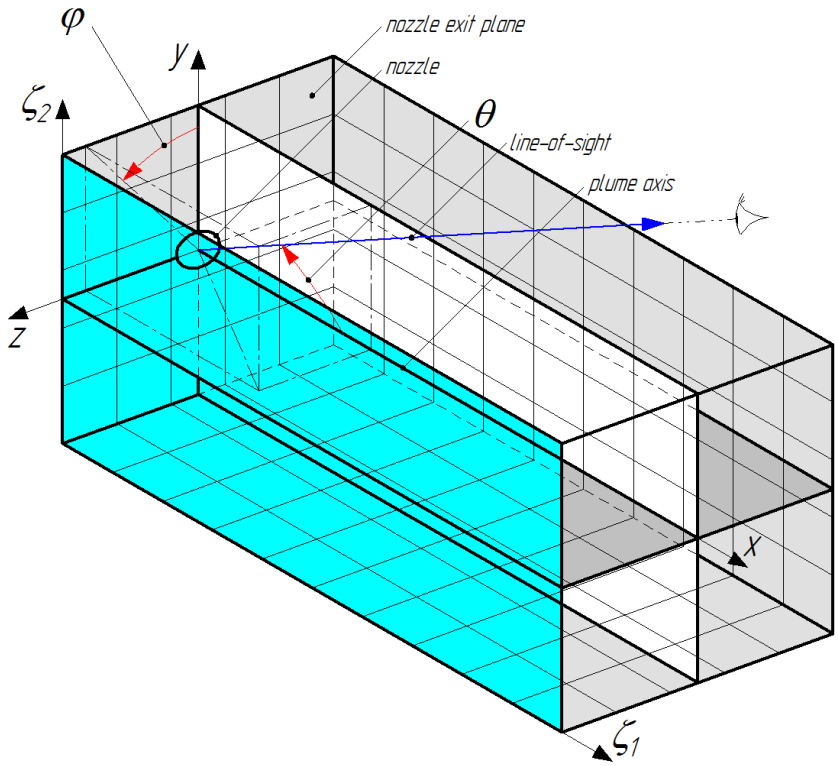

Figure 5.1: Definition of the aspect angle θ and roll angle φ for plume observation

discretization is needed to obtain the distributions of thermophysical and radiative properties along each LOS by means of an interpolation procedure such as IDW. On the other hand, the RT algorithm implemented in JERAD performs in such a manner that the rays (lines-of-sight) pass through the medium starting from the midpoints of the boundary cell faces of the domain. The finer the spatial grid is, the more rays are traced in a given direction.

The FVM solver is based on a control volume approach. The spatial domain is therefore subdivided into control volumes over which the RTE is integrated to formulate the discretization equations. Since the RTE is also integrated over control solid angles, a directional (angular) discretization is required.

5.2.2.1 Spatial Discretization

The $6.0\,d_j \times 1.2\,d_j \times 1.2\,d_j$ domain, where $d_j = 0.875$ m (see Section 4.4), is subdivided into 372100 control volumes using a regular grid of $100 \times 61 \times 61$ shown in Fig. 5.2. The grid is nonuniform along the jet centerline that coincides with the x-axis of the Cartesian coordinate system associated with the domain and becomes denser close to the nozzle exit to enable better prediction of the IR radiation emitted by the hot jet core.

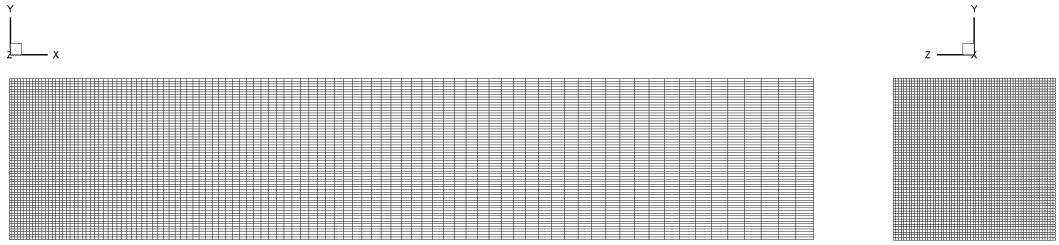

Figure 5.2: Computational grid for the exhaust plume IR radiation calculations

Since the grid is orthogonal it is well suited for the marching technique for solving the RTE when the FVM is employed (see Section 2.6). The use of a nonorthogonal grid, such as that adopted in the author's work [47] for SNB computations, was found to be computationally inefficient as the number of iterations required to achieve a converged solution increases. This is especially critical for nonscattering problems (with black boundaries) where only a single sweep across the grid is sufficient for each discrete direction. Therefore, the grid shown in Fig. 5.2 will be used in all radiation simulations performed in the present study.

5.2.2.2 Angular Discretization

The directional domain discretization of $N_\theta \times N_\varphi$, where $0 \leqslant \theta \leqslant \pi$ and $0 \leqslant \varphi \leqslant 2\pi$, is utilized for all FVM based simulations. In this discretization, the total solid angle of 4π is uniformly subdivided into discrete, nonoverlapping control (solid) angles. The subdivisions of 3×6, 5×10, 7×14, and 9×18 will be used. It is readily seen that the numbers of control angles in the θ and φ angular directions are chosen in such a manner that the average solid angle direction vector $\mathbf{s}^l$ (Eq. (2.9)) is always aligned with the LOS when the plume is viewed broadside, i.e. at $\theta = 90°$ (see Fig. 5.1).

5.2.3 Boundary Conditions

All boundaries of the domain are assumed to be nonemitting and perfectly transparent. The boundary conditions are therefore imposed as

$$I_{\eta,0} = 0. \tag{5.1}$$

Eq. (5.1) provides the intensity entering the boundary for using with the RT solver (first term on the right-hand side of Eq. (2.6)). If the FVM solver is used, Eq. (5.1) defines the intensity leaving the bounding surface that is black and cold (see Eq. (2.5)).

5.2.4 Details on Spectral Modeling

5.2.4.1 Spectral Range and Radiatively Active Species

The IR signature calculations are carried out in the spectral range between 2 and 5 μm (2000 – 5000 cm^{-1}) which is of interest to practical applications [38]. For instance, for military applications, the 3 – 5 μm atmospheric window is mainly used by IR seekers to detect and track flying vehicles [3, 150].[3]

Within the spectral region of 2 – 5 μm, the major vibration-rotation bands are 2.7 and 4.3-μm of CO_2, 2.7-μm of H_2O (overlap with CO_2), and 4.7-μm of CO. Additionally, the 6.3-μm band of H_2O contributes near 5 μm. Generally, for aircraft engine exhausts, the IR emission is primarily dominated by the 4.3-μm band of carbon dioxide.

In the present study, only CO_2 and H_2O are considered as principal emitters in the exhaust plume. Since CO is present in trace concentration in the plume (Table 4.3), it does not contribute to the overall plume emission. Therefore, carbon monoxide was not included in the calculations.[4]

5.2.4.2 Spectral Grids

Spectral grids used for the simulations are those on which the narrow-band model parameters are generated. The SNB model parameters are generated on grids of 25 cm^{-1}, except for the ONERA data set, where a spectral resolution of 5 cm^{-1} was used. Thus, in the spectral range modeled, a uniform grid of 121 nodes is used for SNB model calculations based on the data from EM2C and NASA. The ONERA data based calculations required a uniform grid of 605 nodes.

All CK calculations in this work are based on the k-distribution database by Wang and Modest [131]. In the spectral range 2000 – 4000 cm^{-1}, k-distributions in the database are tabulated with a resolution of 25 cm^{-1}. In the range 4000 – 5000 cm^{-1}, the data are tabulated for narrow bands of 50-inverse-cm-width each. Consequently, a spectral grid of 101 nodes is employed when using the CK method. Note that the nodes (narrow band centers) of this grid are shifted by 12.5 cm^{-1} relative to the SNB grid nodes in the range 2000 – 4000 cm^{-1}.

[3] The 3 – 5 μm atmospheric window is generally used for the detection of hot spots such as jet exhausts. Another window, namely 8 – 12 μm, is better suited for detecting emissions from large surface areas at lower temperatures.

[4] Inclusion of carbon monoxide and/or other emitters in a more general case for radiation calculations is straightforward using JERAD. It is specified by the user's input; no source code modifications are required.

5.3 SNB Model Simulations

Transmissivity-based SNB models (described in Section 3.2) have been used over the last decades as the basic approach to narrow-band simulations including those intended for radiation signature predictions [1, 15]. SNB results are therefore included in this work for completeness and comparison.

The total plume IR emission obtained by integration of the radiance values over the visible plume's surface and over the full spectral interval from 2000 to 5000 cm^{-1} is shown in Fig. 5.3 as a function of aspect angle θ varying between 90 and 0 deg at $\varphi = 90°$. The aspect angle of 90 deg corresponds to the plume viewed broadside, whereas the angle of 0 deg corresponds to the plume viewed backside (Fig. 5.1 of Section 5.2). Since the IR radiation is modeled without taking into account any external radiation sources, such as inner jetpipe walls, the radiant intensity values decrease with decreasing θ.

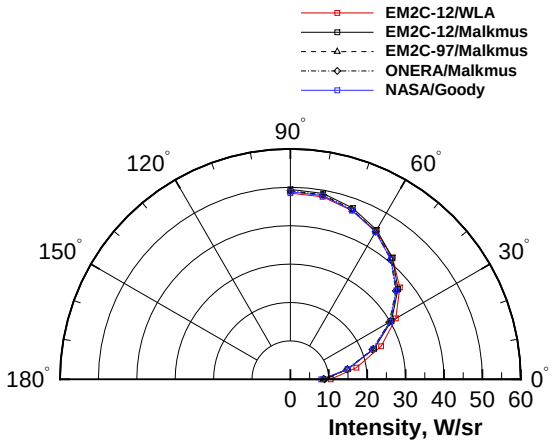

Figure 5.3: Polar plot of plume radiant (total) intensities calculated using the WLA and SNB models with various model parameters in the spectral range 2000 – 5000 cm^{-1}

The five curves presented in the polar plot of Fig. 5.3 were obtained using the WLA (Eq. (3.8)) and the Goody and Malkmus models extended to the case of nonuniform gaseous media by means of the CGA (Eqs. (3.11) and (3.12)).[5] The SNB model parameters due to NASA (which is actually a combination of the parameters tabulated in the NASA handbook by Ludwig et al. [102] for H_2O and in the work by Khmelinin and Plastinin [114] for CO_2), EM2C (both 1997 [83] and updated 2012 [116] versions), and ONERA [117][6] were used.[7] The RTE solution for each LOS through the plume was obtained by the RT solver applied to Eq. (3.1).

[5] Approximations allowing the extension of SNB models to the case of Voigt broadening regime (given by Eq. (3.9) or (3.10)) were not used in the present calculations. The reason for this is that collision broadening is the only mechanism affecting radiative transfer under gas conditions in the plume [164].

[6] The data on SNB parameters were kindly provided by P. Perez of ONERA. Personal communication, July 8, 2011.

[7] Each set of data was used along with the model for which this set had been specifically generated, thereby providing the proper use of adjusted parameters such as $\bar{\delta}'$.

The Malkmus model is known to be the most accurate for polyatomic molecules [23, 106]. The updated parameters of EM2C [116] (designated as EM2C-12 in Fig. 5.3), which are based on the data of CDSD-4000 for CO_2 and HITEMP2010 for H_2O, are believed to be the most reliable. Therefore, the combination EM2C-12/Malkmus will be considered as a reference model in the discussion below.

As can be seen from Fig. 5.3, the difference between the SNB results is insignificant. The WLA overpredicts the radiation emitted from the plume by about 15% for θ varying from 0 to 40 deg.

Table 5.1 demonstrates the total intensities with regard to the case of the broadside viewed plume. The intensities were obtained by integrations over the entire spectral range 2000 – 5000 cm^{-1} as well as over the bands 2200 – 2450 cm^{-1} (4.3-μm band of CO_2) and 3200 – 4200 cm^{-1} (2.7-μm overlapping band of CO_2 and H_2O). The corresponding deviations determined by comparison with the EM2C-12/Malkmus results are summarized in Table 5.2.[8]

Table 5.1: Comparison of predictions of band intensities (in W/sr) using the WLA and SNB models, aspect angle 90 deg

Model	Spectral range, cm^{-1}		
	2000 – 5000	2200 – 2450	3200 – 4200
EM2C-12/WLA	48.46	36.32	9.98
EM2C-12/Malkmus	49.46	41.28	6.32
EM2C-97/Malkmus	48.96	40.72	6.35
ONERA/Malkmus	49.03	39.74	7.47
NASA/Goody	48.84	40.13	6.88

Table 5.2: Relative deviations associated with the WLA and SNB calculations of band intensities presented in Table 5.1

Model	Spectral range, cm^{-1}		
	2000 – 5000	2200 – 2450	3200 – 4200
EM2C-12/WLA	-2.022%	-12.02%	57.91%
EM2C-12/Malkmus	0.000%	0.000%	0.000%
EM2C-97/Malkmus	-1.011%	-1.357%	0.475%
ONERA/Malkmus	-0.869%	-3.731%	18.20%
NASA/Goody	-1.254%	-2.786%	8.861%

[8]Percentage deviation determined by comparison with EM2C-12/Malkmus is

$$\text{Deviation } \% = 100 \times \frac{J - J_{\text{EM2C-12/Malkmus}}}{J_{\text{EM2C-12/Malkmus}}},$$

where J is the radiant intensity.

It follows from Tables 5.1 and 5.2 that, in the range 2000 – 5000 cm^{-1}, the prediction accuracy (absolute deviation value) is limited to 2.02%. Nevertheless, for the band 3200 – 4200 cm^{-1}, the maximum error (deviation) reaches as much as 18.2% in the SNB calculations and 57.9% in the WLA calculations. At the same time, the error resulting from the use of the old EM2C parameters (EM2C-97) does not exceed 1.36%. Note also that Table 5.1 confirms the CO_2 molecule to be the dominant radiator in the plume.

The difference between the predictions becomes more obvious when considering spectral radiant intensities plotted versus wavenumber. Such spectra, which are demonstrated in Fig. 5.4, exhibit the IR radiation emitted by the plume in a particular viewing direction (in Fig. 5.4, the spectra for θ of 90, 40, and 0 deg are presented). Figs. 5.4(a), (c), and (e) show the emission band of CO_2 near 4.3 μm, whilst Figs. 5.4(b), (d), and (f) show the emission band of CO_2 and H_2O near 2.7 μm. The spectra are plotted with a spectral resolution of $\Delta\eta = 25$ cm^{-1}. This spectral resolution is used in the SNB parameters from NASA and EM2C. The ONERA parameters are generated with a spectral resolution of 5 cm^{-1}. The spectra obtained using the ONERA parameters have therefore been degraded to 25 cm^{-1} to match the results based on the parameters of NASA and EM2C.

As can be seen from Fig. 5.4, the WLA fails to predict the plume radiation in both the bands, except near 2325 cm^{-1} at $\theta = 0°$. The Goody model combined with the old parameters from [102, 114] agrees reasonably well with the Malkmus model used along with the EM2C and ONERA parameters. Nevertheless, an error up to 17% occurs in the spectral range 2250 – 2300 cm^{-1} ("red spike" region). In the important range near 2400 cm^{-1} ("blue spike" region), the use of the CO_2 parameters by Khmelinin and Plastinin [114] results in a strong underprediction of the intensity values.

The CO_2 emission spectra near 4.3 μm predicted by the Malkmus model using the SNB parameters of EM2C and ONERA match each other very well. In the computations based on the ONERA parameters, the intensities are however overpredicted in the spectral region between 3400 and 4000 cm^{-1} where the CO_2 and H_2O molecules absorb together. This is most likely due to the fact that the parameter $\bar{\gamma}$ from ONERA is assumed to be independent of species mole fraction. In the ONERA parameters, the $\bar{\gamma}$ values have been computed directly from the spectroscopic database [117] using Eq. (3.4) and then tabulated along with the $\bar{k}$ and $\bar{\delta}'$ values. Reference mole fraction for $\bar{\gamma}_{H_2O}$ is 0.4 that is much greater than the H_2O mole fraction encountered in the plume (see Fig. 4.4). Unlike the parameters of ONERA, the EM2C parameters assume constant values of $\bar{\gamma}$ across bands, but these values do depend on mole fraction. This is particularly critical in the case of water vapor for which self-collision line broadening is about six times greater than foreign gas broadening [98, 102]. Consequently, an overestimation of the reference molar fraction for H_2O results in an increase in the plume IR emission, as can be seen in Figs. 5.4(b), (d), and (f) by comparison with the spectra calculated using the EM2C parameters.

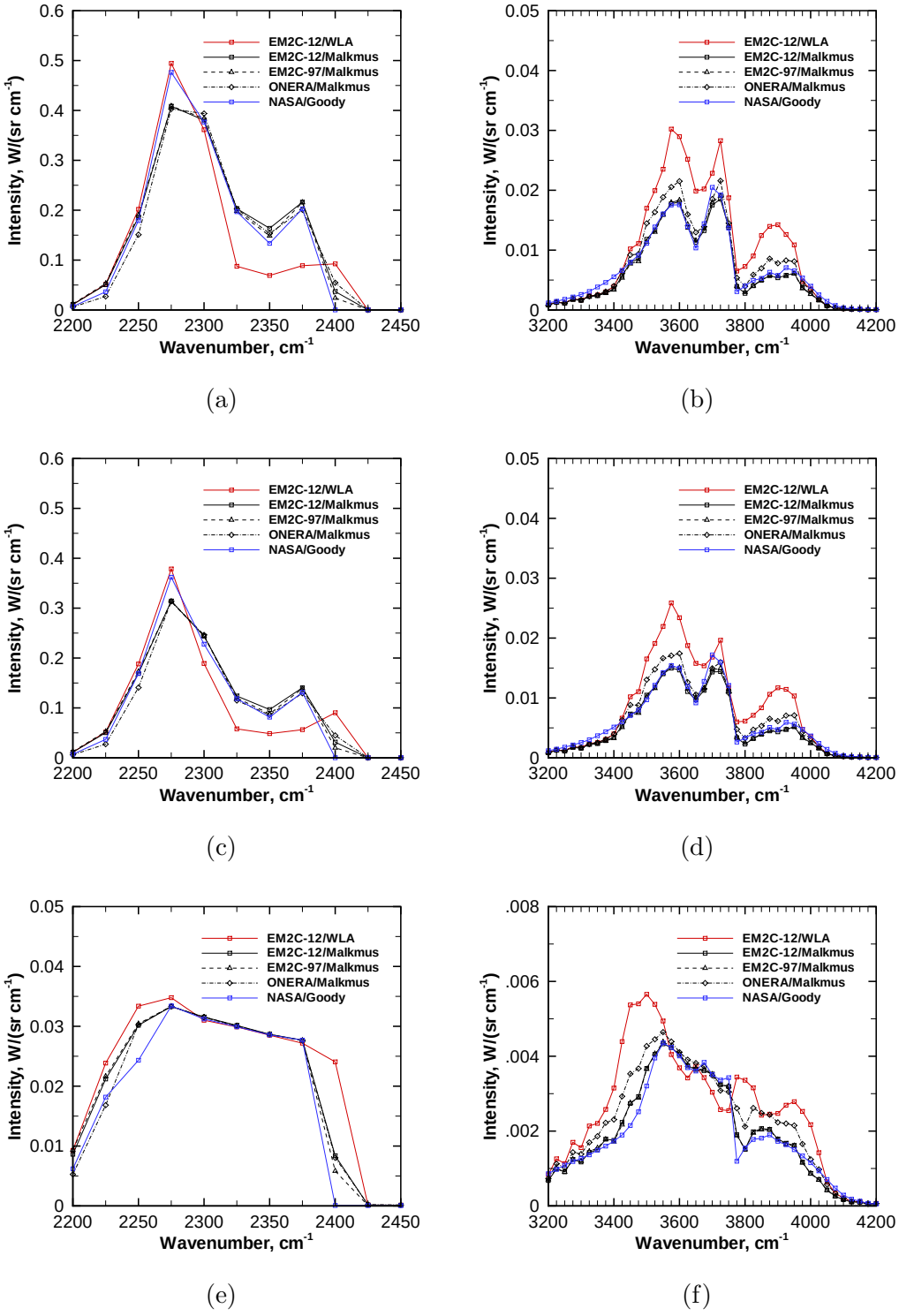

Figure 5.4: Comparison between the WLA and SNB models using various model parameters for plume spectral radiant intensities in the spectral ranges 2200 – 2450 cm^{-1} (4.3-μm band of CO_2) and 3200 – 4200 cm^{-1} (2.7-μm band of CO_2/H_2O) for three aspect angles: (a) 4.3-μm band, $\theta = 90°$, (b) 2.7-μm band, $\theta = 90°$, (c) 4.3-μm band, $\theta = 40°$, (d) 2.7-μm band, $\theta = 40°$, (e) 4.3-μm band, $\theta = 0°$, (f) 2.7-μm band, $\theta = 0°$

It is worth noting that the difference between the SNB calculations based on the old EM2C parameters (EM2C-97) [83] and on the updated EM2C parameters (EM2C-12) [116] reaches as much as 35% in the "blue spike" region. As pointed out by Rivière and Soufiani in [116], this difference simply reflects the differences between earlier and new spectroscopic data that have been utilized to generate the SNB parameters. The difference increases with gas temperature [116].

Station radiances in the plume as functions of the scaled axial position $\tilde{x} = (x - x_{min})/(x_{max} - x_{min})$ are shown in Fig. 5.5. Three narrow bands located in the CO_2 "blue spike" region, which is typically used for detection purposes [161], are considered. The corresponding 2D radiance contours (plume IR images) are given in Figs. 5.6 to 5.8. The station radiances were obtained by integrating the I_η values both spatially and spectrally, as explained in Appendix A. The radiance contours were obtained by performing only spectral integrations over $\Delta\eta = 25$ cm^{-1}. Note that Figs. 5.6 – 5.8 show the radiance distributions at the so-called object plane [19, 162] that is depicted in light blue (but not in white) in Fig. 5.1. The demonstrated data correspond to the case of the IR radiation emitted by the plume in the direction perpendicular to the x-axis (Fig. 5.1).

As expected, the WLA significantly underpredicts the plume radiation in the bands centered at 2350 and 2375 cm^{-1}. In the band centered at 2400 cm^{-1}, the radiation calculated by the WLA appears to be significantly overpredicted. The radiance distributions are similar except for the band 2387.5 – 2412.5 cm^{-1} (see Fig. 5.8). In this band, the use of various SNB model parameters can yield very diverse simulation results as seen in the present computations by comparing with the IR image obtained using the EM2C-12/Malkmus model. Note that the Goody model used along with the SNB parameters coming from the first half of the 70's resulted in zero radiance values (cf. Figs. 5.4(a), (c), and (e)). This emphasizes the importance of using the SNB parameters based on modern spectroscopic data, especially if the plume IR characteristics resolved spectrally are required. In Figs. 5.6 and 5.7 remarkable is the radiation originating from hot spots which occur in the plume due to mixing (see temperature distribution in Fig. 4.3).

The interested reader may also refer to the work by Sventitskiy and Mundt [47] for more detail on plume IR radiation computations using the SNB models.

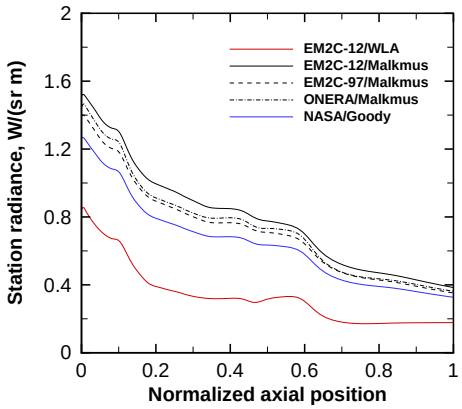

(a)

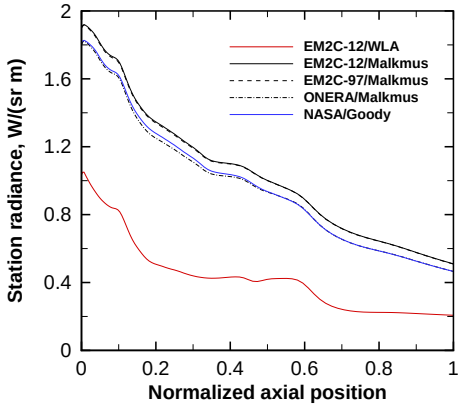

(b)

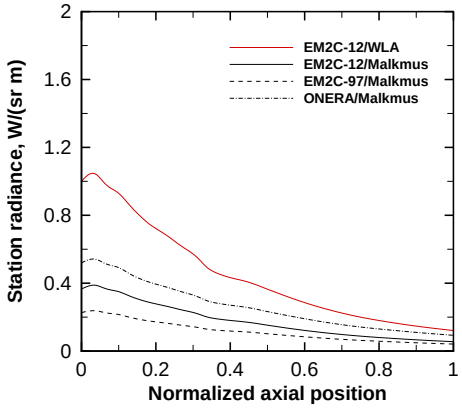

(c)

Figure 5.5: Plume radiation as a function of normalized axial position using the WLA and SNB models with various model parameters in three spectral ranges: (a) 2337.5 – 2362.5 cm^{-1}, (b) 2362.5 – 2387.5 cm^{-1}, (c) 2387.5 – 2412.5 cm^{-1}

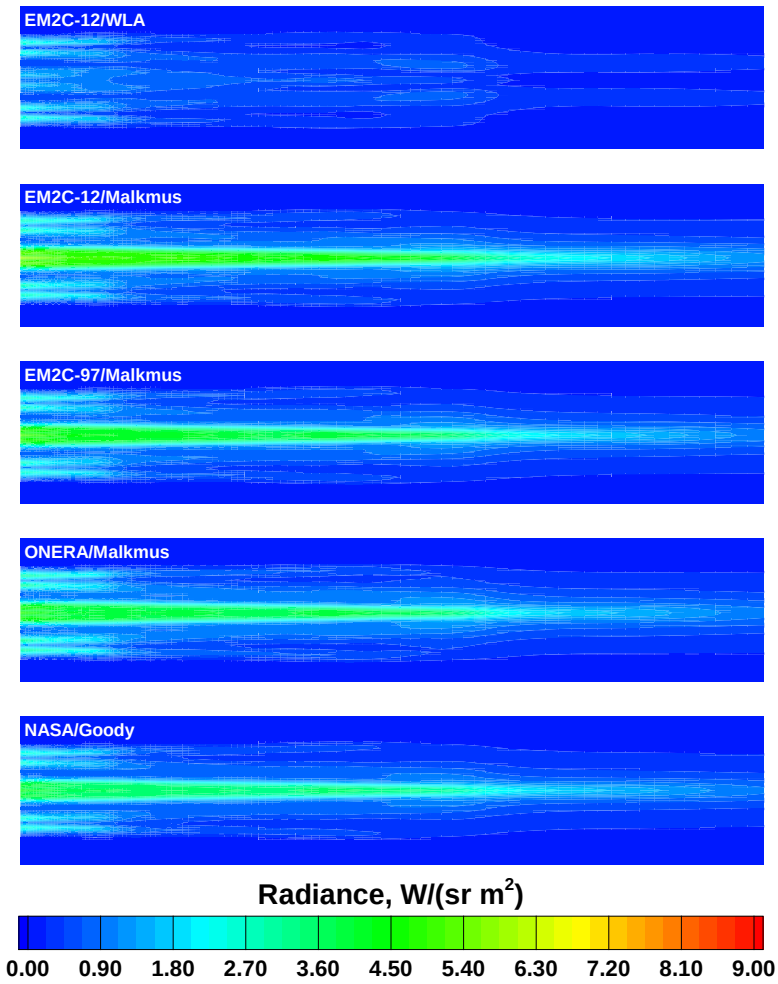

Figure 5.6: Comparison of plume radiance distributions using the WLA and SNB models, $\theta = 90°$, spectral range $2337.5 - 2362.5$ cm^{-1}

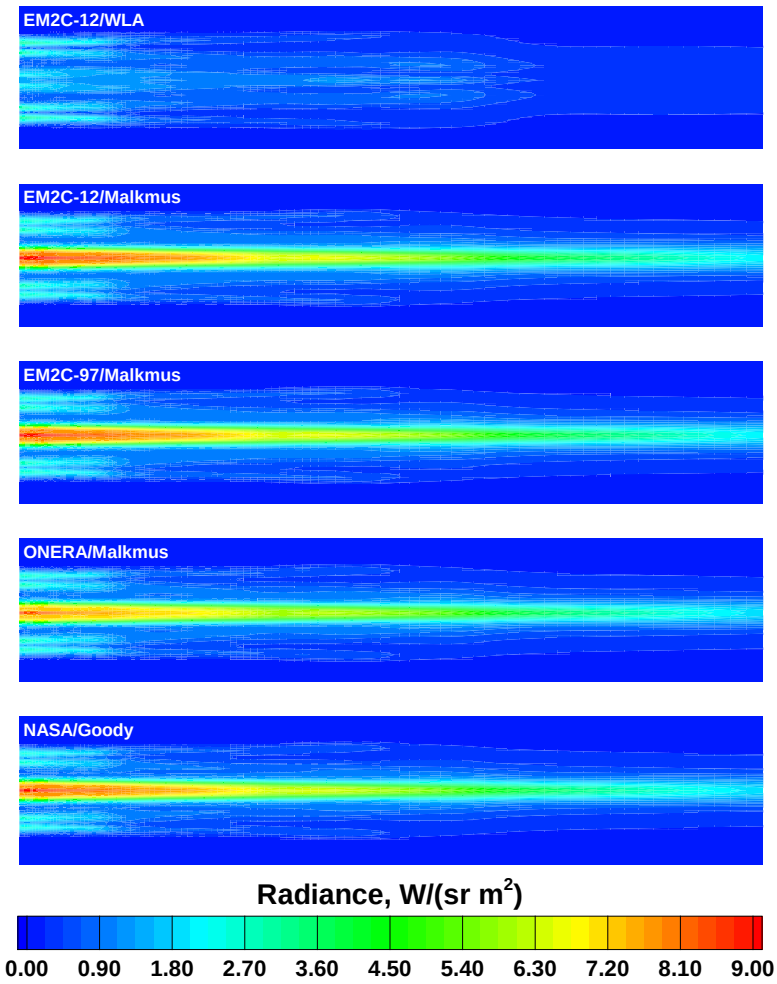

Figure 5.7: Comparison of plume radiance distributions using the WLA and SNB models, $\theta = 90°$, spectral range $2362.5 - 2387.5$ cm^{-1}

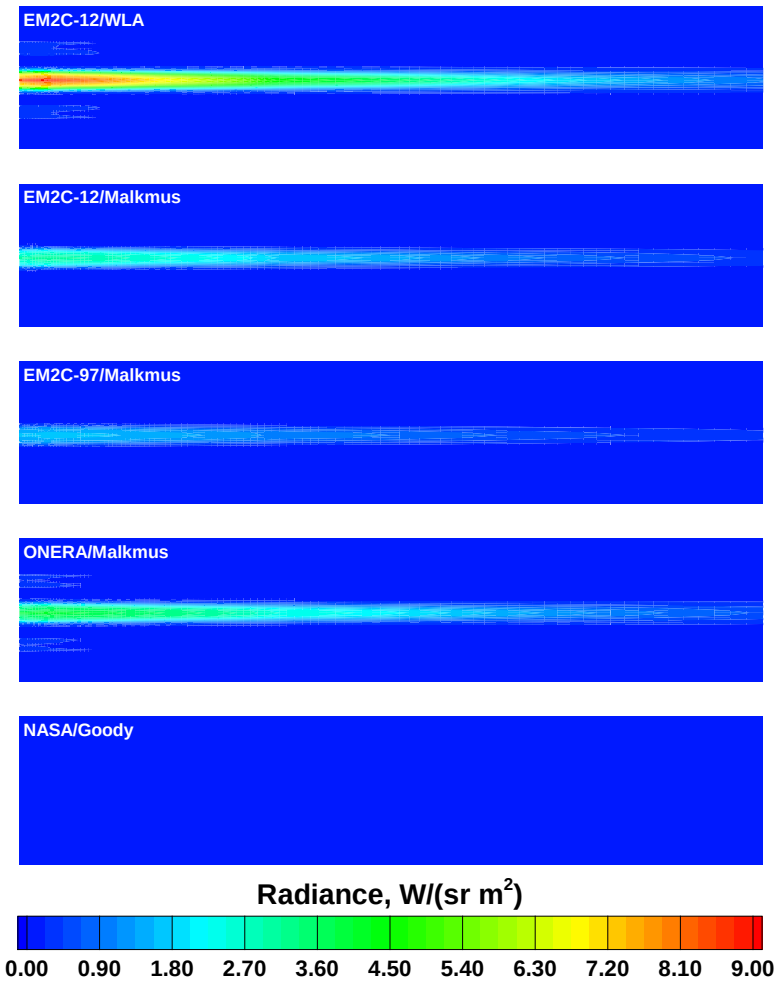

Figure 5.8: Comparison of plume radiance distributions using the WLA and SNB models, $\theta = 90°$, spectral range $2387.5 - 2412.5$ cm^{-1}

5.4 FVM Simulations

5.4.1 RT Benchmark Solution

A reference solution should first be obtained in order to assess the FVM capability of modeling exhaust plume IR signatures. A natural choice to get a benchmark is to use the RT technique. The solution obtained by integration of the RTE along a ray does not suffer from discretization errors such as false scattering and ray effect that are intrinsic to FVM.[9] Therefore, results obtained with the RT solver can be used as a benchmark with which the FVM data are to be compared.

The polar plot in Fig. 5.9 demonstrates the RT solver benchmark solutions for total emission in the spectral range 2000 – 5000 cm^{-1}. Since the FVM uses the absorption coefficient rather than transmissivity as fundamental radiative property, the RT solutions were obtained using the CK method.

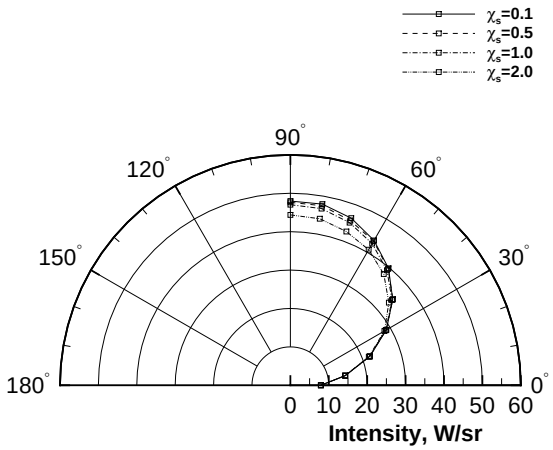

Figure 5.9: Benchmark solutions for radiant intensity obtained by coupling the CK method with the RT solver, spectral range 2000 – 5000 cm^{-1}

In Fig. 5.9, the curves for four values of the scale factor χ_s introduced in Eq. (2.18) are shown. Eq. (2.18) is intended to define the slab length that is actually a step size for numerical integration along lines-of-sight through the plume. In other words, varying the value for χ_s affects the integration error. The effect of χ_s (or equivalently, the number of slabs along LOS) on the radiant intensity is particularly pronounced for the aspect angle of 90 deg and becomes less pronounced when the plume is viewed at near $\theta = 0°$ as can be seen in the figure.

[9]Moreover, FVM calculations provide spectral intensities averaged over control solid angles. As will be demonstrated below, the use of the average intensities is the reason for the appearance of "wiggles" in a FVM solution when predicting plume IR radiation in arbitrary direction. Since the RT solution takes account of the direction of characteristic propagation, it represents the physics with greater fidelity [165], thereby providing an exact representation of the directional nature of plume radiation.

Note that for $\chi_s > 1$ some cells in the numerical grid can be missed when performing interpolation to gain the distributions of thermophysical properties along lines-of-sight. For instance, in the case of $\chi_s = 2$, roughly each second cell in the grid is missed. This explains a poor solution for $\chi_s = 2$ when compared with the data obtained using $0 < \chi_s \leqslant 1$.

In most situations a χ_s value of 1 is optimal, with exception of meshes with bad aspect ratio. For example, all simulations utilizing the SNB models in Section 5.3 were performed with $\chi_s = 1$. However, $\chi_s < 1$ will be used in further calculations to provide grid independent RT solutions.

5.4.2 Comparison with SNB Predictions

As mentioned earlier, the use of transmissivity-based band models for gas radiative properties is the accepted technique to simulate IR signatures from exhaust plumes [1, 15]. The absorptivity (or equivalent black-line width) of a gas layer is not a linear function of physical coordinate along a ray through a gaseous medium [48]. This means that the transmissivity-based models, such as SNB, are not compatible with the FVM for radiation transport. Since the FVM can naturally treat scattering without additional approximations, it is superior to the RT method that is de facto the only approach to be used in conjunction with the transmissivity-based models. To provide a solid spectral modeling procedure, the absorption-coefficient-based CK method is suggested in the present investigation for coupling with the FVM. The question then arises: if and by how much results obtained by using the transmissivity-based and absorption-coefficient-based band models differ from each other when the same RTE solver is employed?

Two calculations were carried out in order to answer this question. In the first calculation, the RT solver was used with the SNB model due to Malkmus, whereas, in the second one, the CK method was employed. The radiant intensity from the plume as a function of aspect angle and the relative percent difference between the data are shown in Figs. 5.10(a) and (b), respectively.[10] The difference is relative to SNB:

$$\text{Relative difference } \% = 100 \times \frac{|J_{\text{CK}} - J_{\text{SNB}}|}{J_{\text{SNB}}}, \tag{5.2}$$

where J is the radiant intensity.

The average relative difference between the CK and SNB predictions is 5.3%. Since the RTE solution technique used to obtain the data is identical for both the calculations, this difference is attributed to the spectral modeling only. Specifically, when compared to the SNB model by Malkmus, the CK method underpredicts the radiant intensity from the plume for all aspect angles investigated. The underprediction is likely due to the fact that the CK method overestimates the correlations between spectral lines in nonisothermal media.

[10] SNB and CK spectra have been compared in the paper [136].

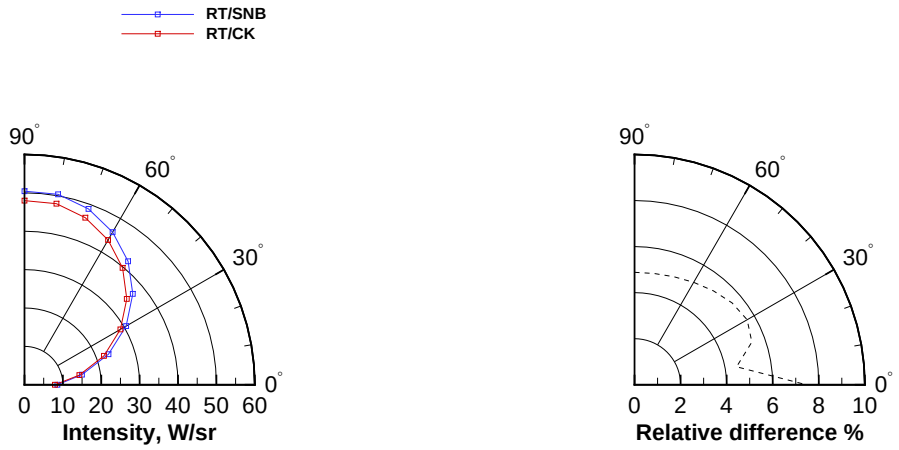

(a) (b)

Figure 5.10: Comparison of CK and SNB (Malkmus model) predictions of radiant intensities from the plume, spectral range 2000 – 5000 cm^{-1}

Another factor contributing to the difference between the predictions could be that the parameters, with which the models are implemented, are formally based on the line parameters from various spectroscopic databases. Indeed, the SNB calculation was performed using the updated parameters by EM2C [116]. These band model parameters were generated from CDSD-4000 for CO_2 and from HITEMP2010 for H_2O. The CK parameters (reordered absorption coefficients) were generated from CDSD-1000 for CO_2 and from an earlier HITEMP edition for H_2O (see Wang and Modest [131]).

In the general case, predictions based on band parameters obtained from various sources are not comparable. The following arguments, however, justify the comparison between the SNB and CK results shown in Fig. 5.10. The present calculations were carried out for temperatures less than 1000 K (see Fig. 4.3). CDSD-1000 can be confidently used for temperatures up to 1600 K [113]. Moreover, as has been demonstrated by Tashkun and Perevalov [113], the difference between CDSD-1000 and CDSD-4000 simulated spectra is marginal even at 2850 K, especially in the 2200 – 2400 cm^{-1} region. For H_2O, the earlier HITEMP1995 compilation had been fairly accurate for temperatures below and around 1000 K, and hence the purpose of HITEMP2010 was to provide a water vapor compilation for higher temperatures up to 4000 K [111].

It is therefore believed that the difference in radiant intensity seen in Fig. 5.10 is mostly attributed to the assumptions involved in the CK method and SNB models. One should not be thinking of the CK method as being worse than SNB models. These are two fundamentally different approaches to narrow-band modeling. The CK method performs with fair accuracy, provided that SNB data are treated as a benchmark. This demonstrates that the CK method can equally be applied to IR signature problems, and not just SNB which is a standard technique implemented in many codes such as NIRATAM [6, 7, 118].

5.4.3 CK Computations Using Various Angular Grids

Fig. 5.11 shows the plume radiant intensities obtained using the FVM coupled with the CK method. In order to demonstrate how the discretization of the directional domain affects the FVM solution, the results for four different solid angle grids, namely 3×6, 5×10, 7×14, and 9×18, are shown (see Section 5.2 for more detail on angular discretization). The benchmark solution of the RT/CK solver is shown by the red solid line in the figure.

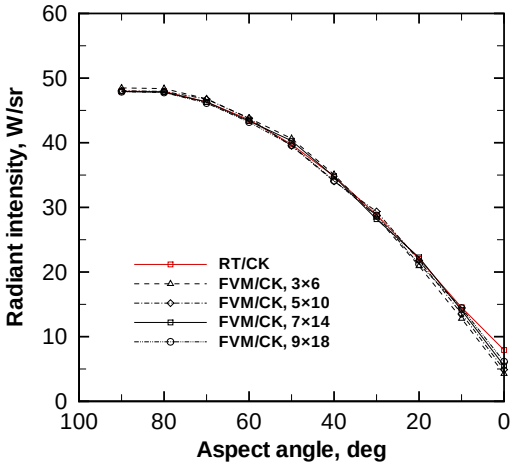

Figure 5.11: Comparison of predictions of the FVM using various angular discretizations with the RT solution for plume radiant intensity in the spectral range 2000 – 5000 cm^{-1}

While being reasonably accurate, the FVM based solution appears to slightly "oscillate" about the benchmark solution. The overshoots and undershoots are due to the fact that the FVM is implemented with uniform intensity over each control solid angle, and so the intensity in a specific observation direction is determined by assuming that it is identical to the average value (given by FVM) which is hold throughout the entire control solid angle. However, in FVM computations with uniform intensity over each control solid angle, the radiation effectively concentrates along the center of the angle [78]. This causes the plume radiative properties, which are truly directional, to be approximated with first-order accuracy in direction leading to the "wiggles" seen in Fig. 5.11.

Fig. 5.12 depicts the situation more clearly. The intensity $I(\vec{s})$ in the direction of observation defined by θ is approximated by the intensity I_P^l computed by FVM. The error associated with this approximation is proportional to the angle between the center of the control solid angle $\Delta\Omega^l$ (defined by $(\theta^- + \theta^+)/2$) and LOS. The red shaded area in the figure shows this angle.

Accuracy of the FVM solution can be improved by increasing the number of control solid angles. This strategy diminishes the error associated with ray effect and thus the directional error discussed above. Table 5.3 summarizes the plume intensities integrated over three spectral bands for the aspect angle of 90 deg (plume broadside view), whereas

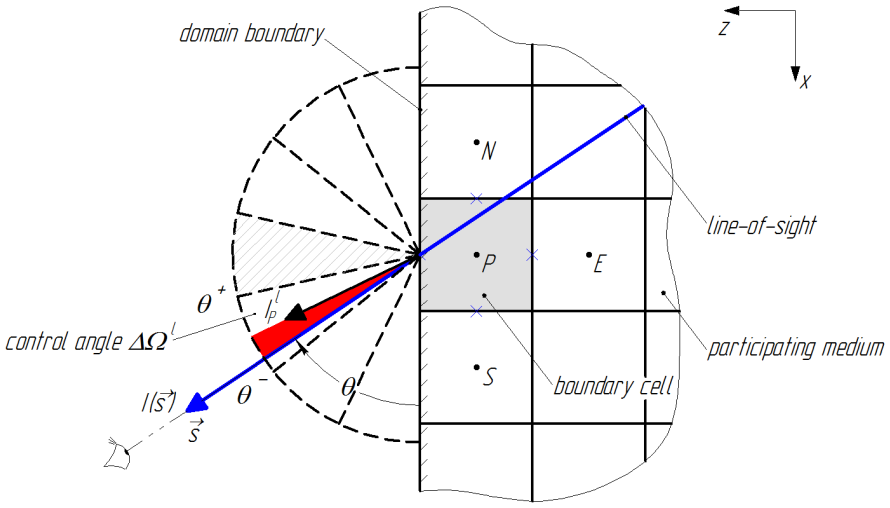

Figure 5.12: Schematic 2D representation to illustrate the error appearing in FVM predictions of plume directional emissions

Table 5.4 summarizes the intensity values for the aspect angle of 0 deg (plume tail view). Increasing the number of control solid angles from 18 (3×6 grid) to 162 (9×18 grid) decreases the band average error in Table 5.3 from 2 to 0.18%, whilst the band average error in Table 5.4 decreases from 51 to 27%.

Poor accuracy of the FVM in the direction $\theta = 0°$ can be explained by examining Fig. 5.12 that depicts the case of $N_\theta = 7$. In general, an increase of N_θ from 3 to 9 (i.e., when the angular space of 4π sr is broken up into 18, 50, 98 and 162 solid angles) results in decreasing the red shaded area shown in Fig. 5.12. This in turn decreases the error in prediction of the plume directional radiation. Since in this work the aspect angle θ is always measured from the plume centerline (see Fig. 5.1) that coincides with the x-axis of the coordinate system utilized to measure the zenith angle for angular discretization, the aspect of 0 deg is a special case in which $\theta = \theta^-$. This implies that the error for $\theta = 0°$ decreases with increasing N_θ, however it never vanishes.

If the plume is observed broadside at $\theta = 90°$, the LOS direction $\vec{s}$ always coincides with the center of a control angle (cross-hatched sector in Fig. 5.12) so that $\theta = (\theta^- + \theta^+)/2$. Consequently, the FVM provides the most accurate results as can be seen in Table 5.3.

How the solid angle mesh refinement influences the FVM calculations is demonstrated further in Fig. 5.13. This figure shows the plume spectra in the 2.7-μm band of CO_2/H_2O and in the 4.3-μm band of CO_2 obtained for various θ. As in Fig. 5.11, the spectra are computed by the 3×6, 5×10, 7×14 and 9×18 FVM and compared with the spectra computed by the RT method.

For $\theta = 90°$, Figs. 5.13(a) and (b), the FVM calculations match each other and the benchmark solution very well. A minor inaccuracy of the 3×6 FVM is solely due to errors that arise from both the spatial and directional discretizations [77, 78, 80]. The

Table 5.3: Band intensities (in W/sr) calculated using the FVM with various angular discretizations in comparison with the RT benchmark solution, aspect angle 90 deg

Model	Spectral range, cm^{-1}		
	2000 – 5000	2200 – 2450	3200 – 4200
RT/CK	47.97	40.88	5.87
FVM/CK, 3×6	48.48	41.02	6.14
FVM/CK, 5×10	48.05	40.86	5.94
FVM/CK, 7×14	47.93	40.82	5.88
FVM/CK, 9×18	47.88	40.80	5.86

Table 5.4: Band intensities (in W/sr) calculated using the FVM with various angular discretizations in comparison with the RT benchmark solution, aspect angle 0 deg

Model	Spectral range, cm^{-1}		
	2000 – 5000	2200 – 2450	3200 – 4200
RT/CK	7.93	5.11	1.877
FVM/CK, 3×6	4.28	3.80	0.370
FVM/CK, 5×10	4.91	4.23	0.514
FVM/CK, 7×14	5.51	4.61	0.672
FVM/CK, 9×18	6.13	4.98	0.843

FVM based spectra for $\theta = 40°$ depicted in Figs. 5.13(c) and (d) additionally contain the directional error explained in Fig. 5.12 so that the difference between the RT and FVM solutions becomes noticeable, especially when using the 5×10 and 9×18 angular grids. Note that, on the given spatial grid (see Fig. 5.2), the 3×6 FVM performs better than the 9×18 FVM. This is likely due to the interaction between the errors associated with ray effects and false scattering which tend to compensate each other [78, 80] (see also Section B.2). As expected, the FVM predictions for $\theta = 0°$ show large errors in comparison with the RT predictions (Figs. 5.13(e) and (f)). These particularly large errors for $\theta = 0°$ can also be attributed to the use of the step scheme which makes gas optically thin, especially in the CO_2 4.3-μm band (Fig. 5.13(e)).

The aspect angle of 90 deg is beneficial to FVM analysis because simulation results are not affected by the directional error. Fig. 5.14 shows the radiance integrated along the plume centerline as computed by the FVM with the four angular grids for $\theta = 90°$. The computations were carried out in three spectral intervals between 2325 and 2400 cm^{-1} covering the 4.3-μm band center and the "blue spike" region. When compared to the benchmark solution by RT, the accuracy of FVM increases with the number of control angles, in particular, in the 2375 – 2400 cm^{-1} spectral range (Fig. 5.14(c)).

Plume IR images near 4.3 μm (spectral range 2325 – 2350 cm^{-1}) are compared in Fig. 5.15. Each image represents the spatial distribution of plume radiance at the object plane (Fig. 5.1). It is easily seen that the FVM images at $\theta = 90°$ are almost indistinguishable and they are very similar to the benchmark image by RT. Insignificant error caused by a small number of discrete solid angles is observed in the 3×6 FVM solution.

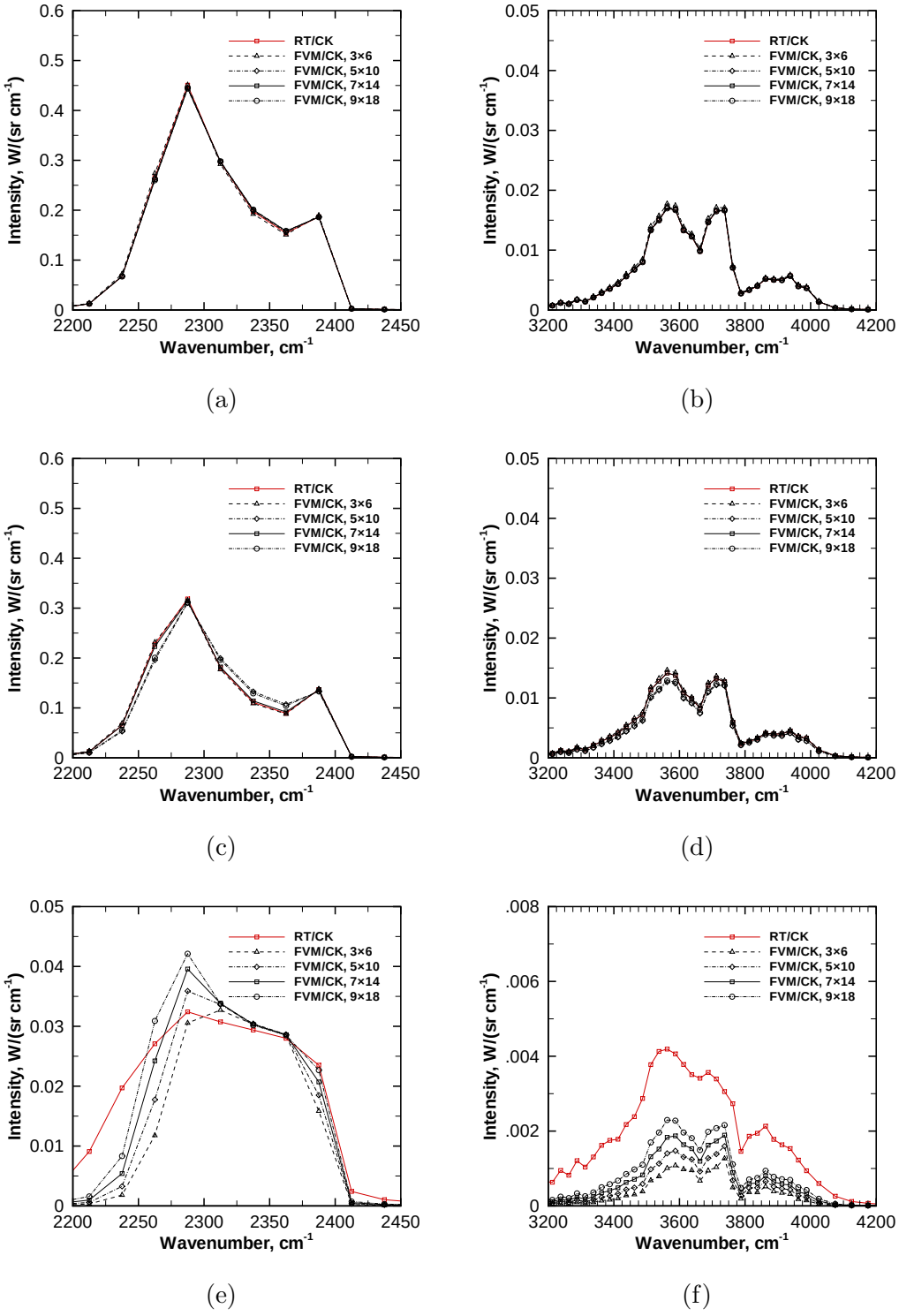

Figure 5.13: Comparison between RT and FVM using various angular discretizations for plume spectral radiant intensities in the spectral ranges 2200 – 2450 cm^{-1} (4.3-μm band of CO_2) and 3200 – 4200 cm^{-1} (2.7-μm band of CO_2/H_2O) for three aspect angles: (a) 4.3-μm band, $\theta = 90°$, (b) 2.7-μm band, $\theta = 90°$, (c) 4.3-μm band, $\theta = 40°$, (d) 2.7-μm band, $\theta = 40°$, (e) 4.3-μm band, $\theta = 0°$, (f) 2.7-μm band, $\theta = 0°$

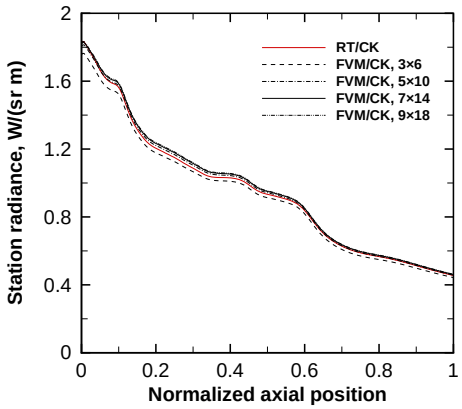

(a)

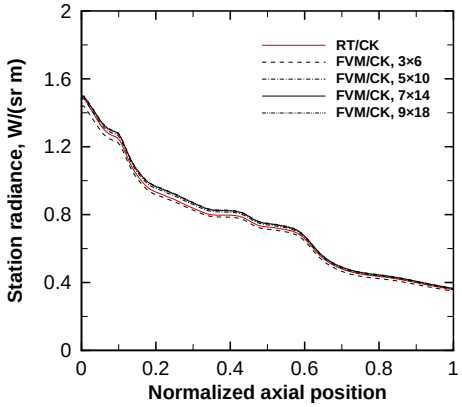

(b)

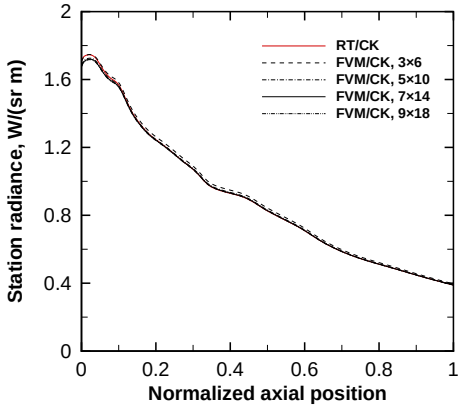

(c)

Figure 5.14: Plume radiation as a function of normalized axial position using RT and FVM with various angular discretizations in three spectral ranges: (a) 2325 – 2350 cm^{-1}, (b) 2350 – 2375 cm^{-1}, (c) 2375 – 2400 cm^{-1}

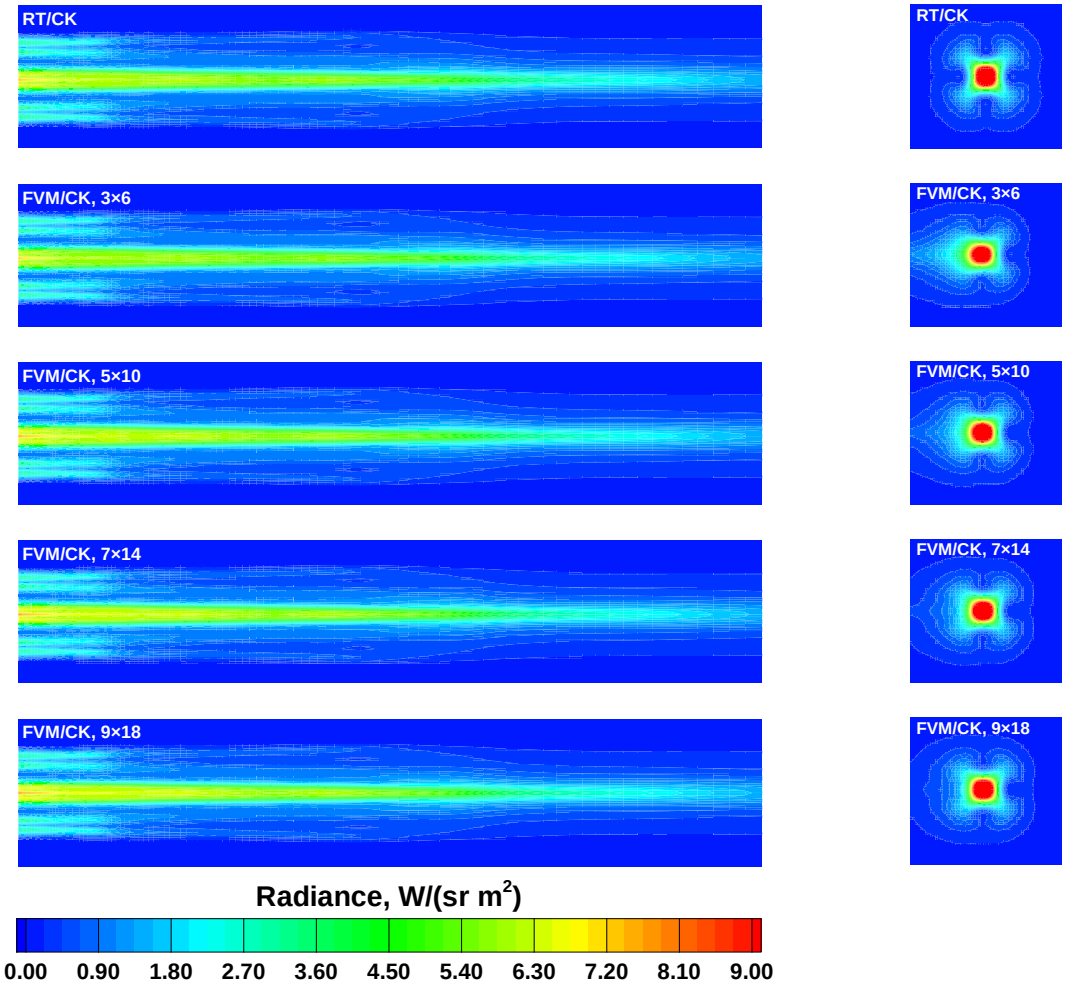

Figure 5.15: Computed distributions of plume radiances using the FVM with various angular discretizations in comparison with the RT benchmark solutions at $\theta = 90°$ (left) and $\theta = 0°$ (right), spectral range 2325 – 2350 cm^{-1}

The improvement of the FVM solution with increasing the number of control angles $N_\theta \times N_\varphi$ becomes clearly visible when changing the aspect angle from 90 to 0 deg. For $\theta = 0°$, the directional error has a diffusion-like appearance that is clearly seen in Fig. 5.15. While decreasing with increasing $N_\theta \times N_\varphi$, the error is not completely eliminated even using the 9×18 discretization. This effect is also very well seen in Fig. 5.13(f) and in Table 5.4 for both spectral and integrated band intensities.

For the given spatial domain discretization, the 7×14 FVM provided fairly accurate results within a reasonable computational time. The angular discretization of 7×14 will therefore be used in all subsequent computations.

5.4.4 Gray Narrow-Band Calculations

The results of FVM demonstrated in Fig. 5.11 and in Figs. 5.13 to 5.15 were obtained using the CK method. Fig. 5.16(a) shows the plume IR radiation that is predicted by coupling the FVM with gray narrow-band spectral models. The gray narrow-band models are those of the CKG and SNBG formulations, as discussed in Section 3.6. The mean absorption coefficient is dependent on local gas properties and calculated inside each narrow band using Eq. (3.49) for CKG and Eq. (3.50) for SNBG.

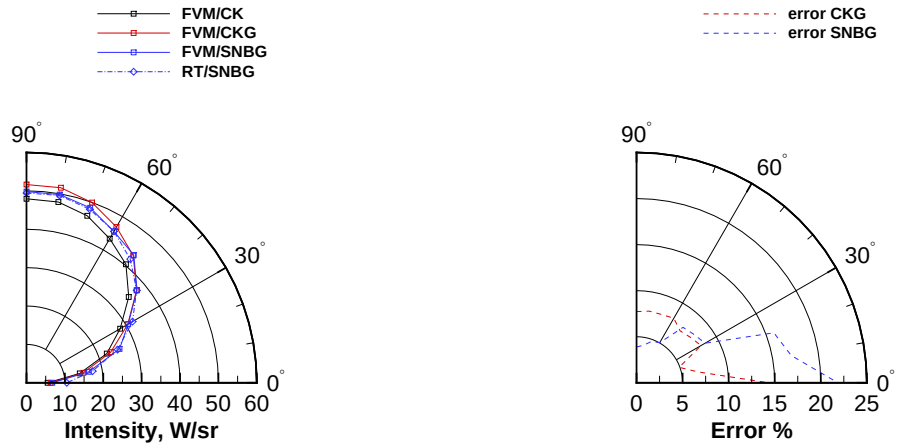

(a) (b)

Figure 5.16: Comparison of radiant intensities from the 7×14 FVM computations using the SNBG, CKG and CK spectral models in the spectral range $2000-5000$ cm^{-1}

In comparison with the CK method, the use of the CKG and SNBG models enables a decrease in computational time by a factor of about N (number of quadrature points, $N = 8$ for the current calculations, see Table 3.2). On the other hand, these models always generate errors that can be determined by comparison with CK as

$$\text{Error } \% = 100 \times \frac{J_{\text{CKG/SNBG}} - J_{\text{CK}}}{J_{\text{CK}}}. \tag{5.3}$$

Fig. 5.16(b) shows the CKG and SNBG errors as functions of aspect angle. The maximum error reaches as much as 22% for $\theta = 0°$, although it is less than 10% for θ between 30 and 90 deg. The latter is not intended to imply that the gray models are an acceptable approximation of CK.

Indeed, percentage errors shown in Fig. 5.16(b) are for intensities integrated over the entire spectral range from 2000 to 5000 cm^{-1}. The errors eliminate each other when performing spectral integrations. This can clearly be seen in Fig. 5.17 in which a comparison is done between the CK and CKG spectral intensities. When considered spectrally, i.e. with $J \equiv J_\eta$ in Eq. (5.3), the errors are very significant (overprediction by up to 193%, see Fig. 5.17(d)).

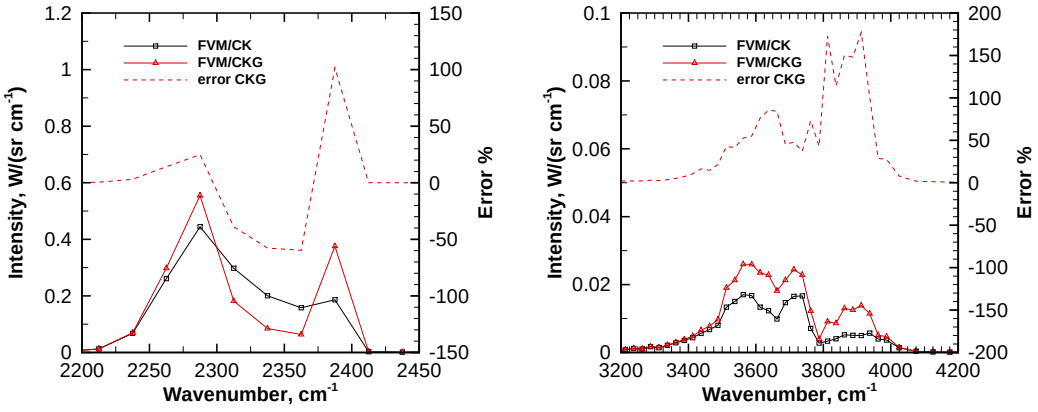

(a)

(b)

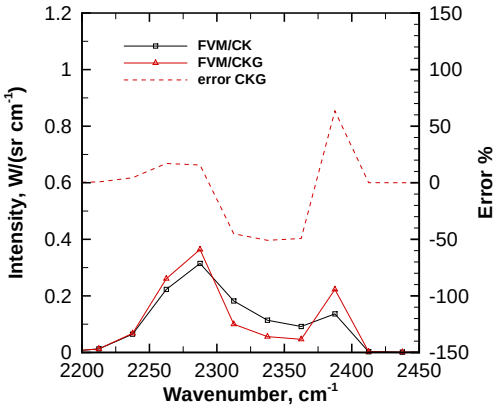

(c)

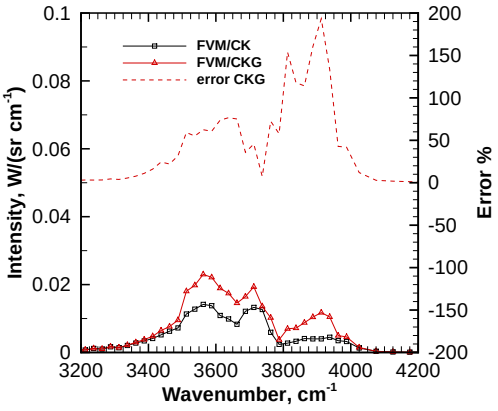

(d)

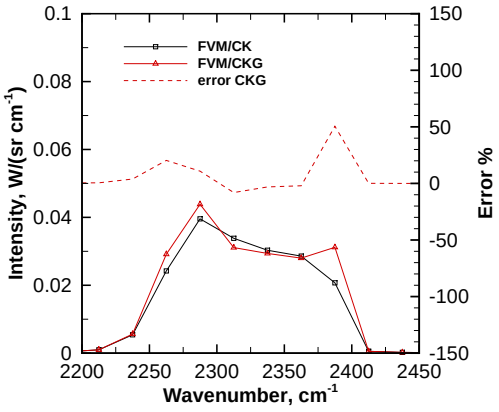

(e)

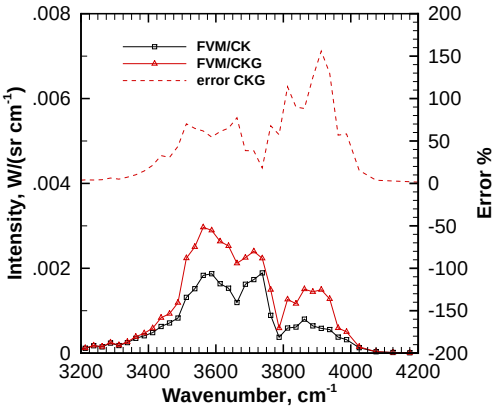

(f)

Figure 5.17: Comparison of spectral radiant intensities from the 7×14 FVM computations using the CKG and CK spectral models for three aspect angles: (a) 4.3-μm band of CO_2, $\theta = 90°$, (b) 2.7-μm band of CO_2/H_2O, $\theta = 90°$, (c) 4.3-μm band, $\theta = 40°$, (d) 2.7-μm band, $\theta = 40°$, (e) 4.3-μm band, $\theta = 0°$, (f) 2.7-μm band, $\theta = 0°$

Because of simplicity, methods based on gray-band approximation are very attractive for use in engineering applications. For example, such methods have been studied by Liu et al. [137] and applied by some researches to IR signature predictions [25, 101, 166–168]. Nevertheless, since the fine structure of spectral lines effectively disappears when the mean absorption coefficient is assumed, the gray-band approximation is accurate for WLA conditions only, i.e. at $xpl\bar{k}/\bar{\beta} \ll 1$ [98]. This is typically the case for aircraft combustion chambers and rocket engines [98]. For gas conditions encountered in aero-engine exhausts, the gray-band modeling approach leads to erroneous results in IR signature calculations as demonstrated above by the example of the CKG and SNBG models. Note that the use of CKG or SNBG may also lead to erroneous predictions of radiative heat fluxes, an aspect that is confirmed in computations (see Section B.4).

5.5 Summary

A large number of calculations have been carried out in this chapter in order to demonstrate that the FVM and the CK method are capable of accurately predicting IR emissions originating from aircraft engine plumes. A purely gaseous exhaust comprising the most important radiatively active species, carbon dioxide and water vapor, was considered. The consideration of a medium without scattering particles allowed FVM/CK computational results to be first compared to and validated against those computed by the RT technique and "traditional" SNB models. SNB calculations were performed using the Goody and Malkmus models along with various SNB parameters. It was found that the predicted plume IR radiation can differ significantly dependent upon the model and/or parameters utilized, in particular, for plume IR spectra. A comparison of the total intensities calculated by RT/CK with those computed by the most reliable of the SNB models was conducted. This comparison revealed that the maximum difference between the CK and SNB intensities does not exceed 5.3% on average. This confirms the accuracy of the CK method applied to the calculation of thermal radiation emitted by realistic aero-engine exhausts. In the FVM computations performed, a particular emphasis was placed upon the investigation of the effects of angular discretization at a given discretization of the spatial domain. Comprehensive analysis of the computational results has shown that the discretization of 7×14 gives reasonable solutions with respect to accuracy and computational costs. Finally it was demonstrated that the use of gray narrow-band models would appear to be a reason of significant errors. Such models neglect the fine structure of spectral lines by simply using mean absorption coefficients. When compared to the CK method, the CKG and SNBG formulations overpredict the total plume IR emission by up to 14% and 22%, respectively. The relative error calculated spectrally was found to be unacceptably large (up to 193% using CKG in the spectral range $3200-4200$ cm^{-1}). It is therefore not recommended to replace the band models, such as SNB or CK, by their gray-band approximation counterparts.

Chapter 6

Prediction of IR Signatures from Gas-Particle Plumes Using the Finite Volume Method

6.1 Introduction

The conventional technique applied over the years to predict radiation from plumes relies on the usage of IR band models. A number of difficulties associated with these models constitute what is known as the band model–scattering incompatibility problem [11]. An approach based upon the FVM is therefore proposed in the current work to accurately incorporate the effects of scattering into predictions of IR radiation signatures from nongray absorbing-emitting-scattering exhaust plumes.

The results of gas-particle plume IR signature calculations using the FVM computational procedure are presented in this chapter. As in Chapter 5, the plume is assumed to be observed from an infinite distance at varying aspect angles. The same grid is utilized for the spatial domain discretization. A total of 7×14 control angles are used to discretize the angular space. The CK method is applied to model the radiative properties of the mixture of exhaust gas with air.

Two different radiative signature calculation problems will be considered in this chapter. In the first calculation, IR radiation from a realistic exhaust plume will be simulated numerically. The realistic exhaust is a participating medium containing an inhomogeneous and nonisothermal CO_2–H_2O–air–soot mixture with the amount of soot added to the gaseous phase based on measurements available in the literature (the gas composition is identical to that used in Chapter 5). In the second calculation, the amount of soot present in the exhaust will be intentionally increased and "model" scattering particles will be introduced. The latter serves to illustrate the effects of scattering on plume IR emissions predicted by the FVM.

6.2 Particles in the Plume

6.2.1 Soot Particles

It is assumed that soot obeys the same transport process as the gaseous phase. This is a good assumption since the soot particles are usually very small. Consequently, the soot volume fraction is defined by

$$f_v^{soot} = f_{v,j}^{soot}\,\xi, \tag{6.1}$$

where $f_{v,j}^{soot}$ is the soot volume fraction at the nozzle exit and ξ is the mixture fraction calculated based on the distribution of CO_2 in the plume (see Fig. 4.4). Recent nonintrusive measurements [139] have shown that the average value for $f_{v,j}^{soot}$ is dependent on aero-engine operating conditions and varies between 0.06 and 1.55 ppbv.

The following assumptions were made for the prediction of IR signatures from the plume containing soot particles:

1. The optical properties of soot are those determined from Eq. (3.53) for flame soot.
2. Soot particles are present in the plume in the nonagglomerated form.
3. Soot particles are at the same temperature as the gas mixture.

The legality of the first assumption is not so obvious because the optical properties of soot formed as a result of incomplete combustion of kerosene fuels may differ from the properties of flame soot [139]. The last two assumptions are involved in most radiative transfer predictions in gas-soot mixtures [23, 134].

6.2.2 Model Particles

In the model plume calculations, which will be discussed in Section 6.4, the scattering coefficient for particles is obtained from the following equation:

$$\sigma_{s\eta}^{model} = \alpha\kappa_{p\eta}^{soot}. \tag{6.2}$$

In this formula, α is a model constant introduced to vary the single scattering albedo and $\kappa_{p\eta}^{soot}$ is the absorption coefficient calculated using Eq. (3.51) for soot. The use of Eq. (6.2) preserves the scattering coefficient to be nongray.

Scattering coefficients given by Eq. (6.2) are used to demonstrate that the finite volume radiation transport procedure is capable of calculating thermal emissions of exhaust plumes with scattering particles. It must however be stressed that the treatment of the scattering coefficient in such a very artificial manner is arbitrary and serves demonstrative purposes only.

6.3 Simulation of the Realistic Plume

In the case of the realistic exhaust it is assumed that soot is distributed within the plume medium according to Eq. (6.1) with $f_{v,j}^{soot} = 0.25 \times 10^{-9}$. This value is based on turbojet exhaust measurements at take-off regime [139]. The medium is fully participating, i.e. absorbing, emitting, and scattering. The soot's absorption coefficient is calculated using Eq. (3.51), whereas the scattering coefficient is determined by means of Eq. (3.52) with the $\bar{a}$ value of 25 nm. The scattering phase function is that for Rayleigh scattering (Eq. (3.56)).

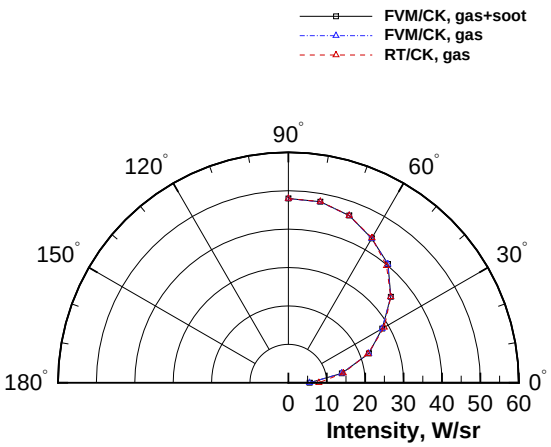

Figure 6.1: Comparison of the predicted radiant intensities from the plume containing soot particles with the pure exhaust gas mixture intensities in the spectral range 2000 – 5000 cm^{-1}

Numerical results for the radiant intensity are shown in Fig. 6.1. To ease the analysis of this particular plume case, the results for the non-sooty plume taken from Section 5.4 are shown in the figure as well.

The predictions for the soot-loaded plume and for the plume containing CO_2 and H_2O as radiators and no soot are actually different from each other but the difference is almost indistinguishable. This is very expected because soot is present in the medium at low concentration levels, and also due to the fact that scattering from soot particles is negligible in comparison to absorption. Therefore, the effects of soot on the IR radiation are not important for real-life aero-engine exhaust situations, at least within the limits of the assumptions made for the computations (see p. 98).

6.4 Model Plume Simulations

Soot volume fractions encountered in realistic aero-engine plumes have been found in the previous section to be small enough to influence the IR radiation emitted by the plume. Moreover, radiative scattering by soot particles can usually be neglected.

Therefore, model situations are suggested here in order to demonstrate the benefits of using the FVM based technique. In contrast to the realistic plume situation, the model plume scenarios assume that soot particles are present in the plume in high concentrations so that their impact on IR signatures becomes pronounced. Additionally, rather than using Eq. (3.52), the scattering coefficient for model particles is obtained from Eq. (6.2).

6.4.1 Effect of Particle Volume Fraction

The influence of an increase in particle (soot) volume fraction on the IR characteristics of the plume is first assessed. The plume is assumed to be an absorbing-emitting but nonscattering medium; that is, the gas and particle absorption/emission effects are only included.

Fig. 6.2 depicts the plume radiant intensities versus aspect angle obtained by integration over the spectral range $2000-5000$ cm^{-1} for various particle concentrations in the exhaust gas-particle mixture. In fact, an enhanced formation of soot in the combustion chamber was reproduced by fictitiously increasing the amount of soot in the plume. As can be seen from the figure, the aero-engine exhaust plume IR radiation is substantially enhanced with the amount of soot. In particular, an increase in soot volume fraction by a factor of 10^3, i.e. from 0.25 ppbv to 0.25 ppmv, enhanced the plume radiant intensity on average by 104%.

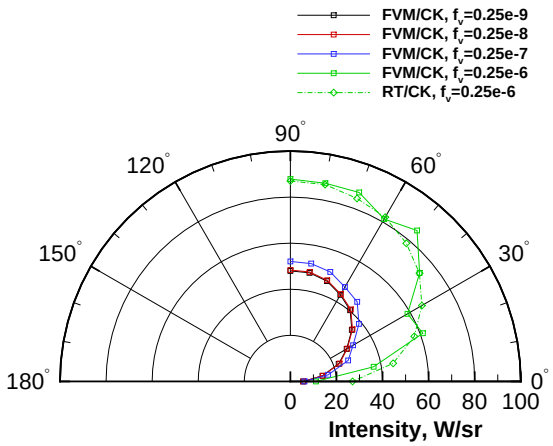

Figure 6.2: Effect of volume fraction of nonscattering particles on the predicted plume radiant intensities in the spectral range $2000-5000$ cm^{-1}

"Smoke" is one of the regulated pollutant emission standards for aircraft engines [140]. An increase in soot emission is an early indication of an engine malfunction. Such a malfunction can thus be recognized through increased thermal radiation from the engine exhaust.

Since the effects of scattering are not considered, the RT solver can also be applied to the present calculations. As before, the RT solution is used to validate the FVM

predictions. Radiant intensity overshoots and undershoots inherent in FVM solutions are then readily seen in Fig. 6.2 for the particle concentration of 0.25 ppmv. These oscillations have also been observed in the simulations for the purely gaseous exhaust (see Fig. 5.11 of Section 5.4).

Fig. 6.3 demonstrates the plume IR spectra in the 2000 – 4000 cm^{-1} spectral interval. In this figure, the particle concentrations vary from 0.25 ppbv to 2.5 ppmv. When compared to the non-sooty plume (0.25 ppbv), nongray soot radiation appears in the spectral windows and dominates over gas radiation for high volume fractions. This trend is prominent for both the directions for which the spectra are shown.

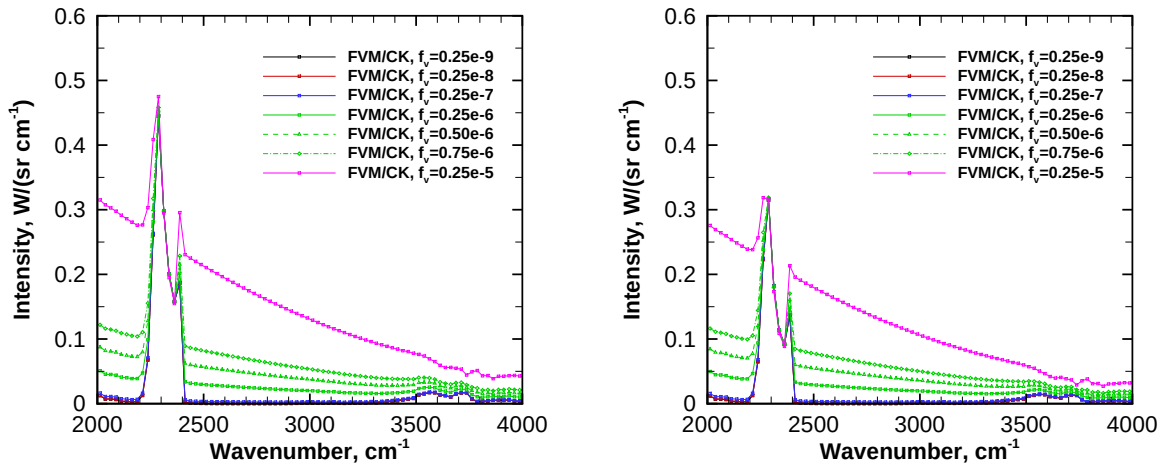

Figure 6.3: Effect of volume fraction of nonscattering particles on the predicted plume IR spectra for (a) $\theta = 90°$ and (b) $\theta = 40°$

Finally Fig. 6.4 depicts the plume radiances as computed by varying the soot volume fraction. The radiance distribution for the plume containing gas (CO_2–H_2O–air mixture) and no soot is also shown for comparison. The radiance values were obtained by integration over the important spectral region between 2375 and 2400 cm^{-1} that is typically used for CO_2 retrieval when performing IR measurements of aero-engine exhaust emissions [161]. It is readily seen that the plume's shine increases with the soot volume fraction in this CO_2 "blue spike" region.

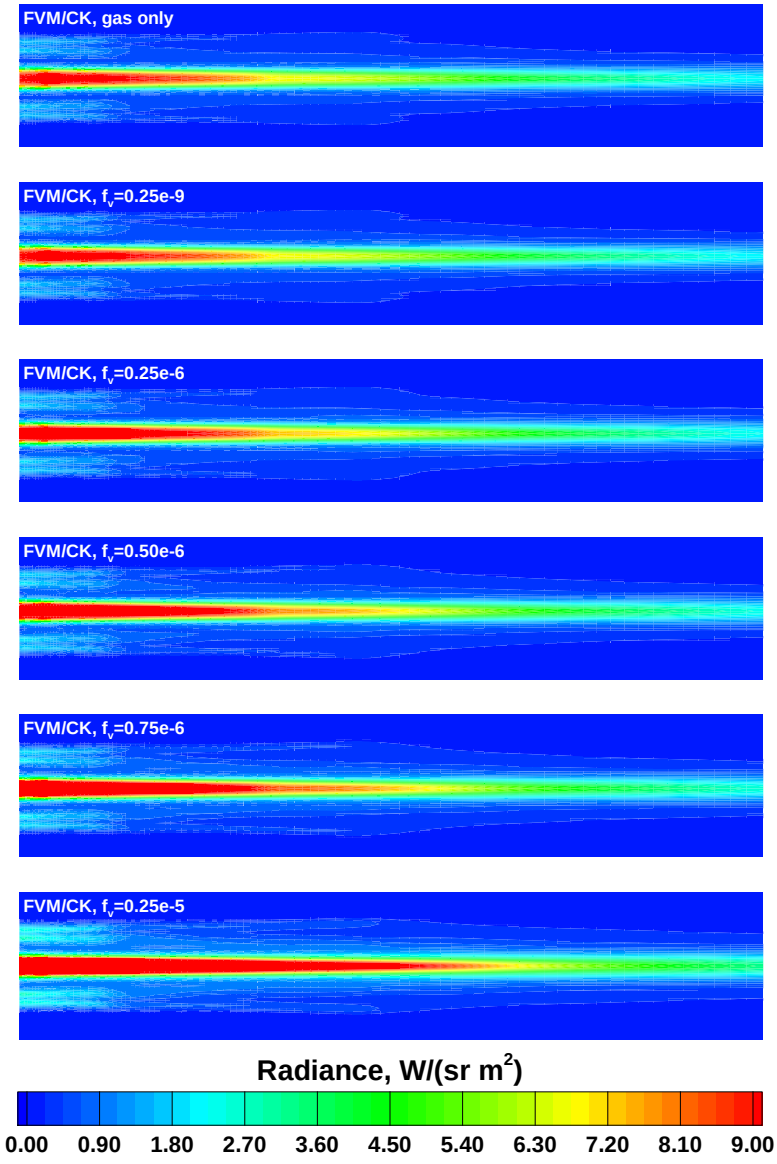

Figure 6.4: Effect of volume fraction of nonscattering particles on the predicted plume radiance, $\theta = 90°$, spectral range 2375 – 2400 cm^{-1}

6.4.2 Effect of Scattering Opacity

The effects of the scattering opacity (scattering coefficient) on the predicted plume IR emissions are examined in Figs. 6.5 to 6.7. For this particular numerical study, the plume is assumed to be absorbing, emitting, and isotropically scattering. The scattering opacity and, respectively, optical thickness for scattering are artificially increased by varying the value of α in Eq. (6.2) while keeping the particle volume fraction at the nozzle exit in Eq. (6.1) constant ($f_{v,j} = 0.5 \times 10^{-6}$). Four values of α, namely 0 (no scattering), 1, 10, and 100, are used.

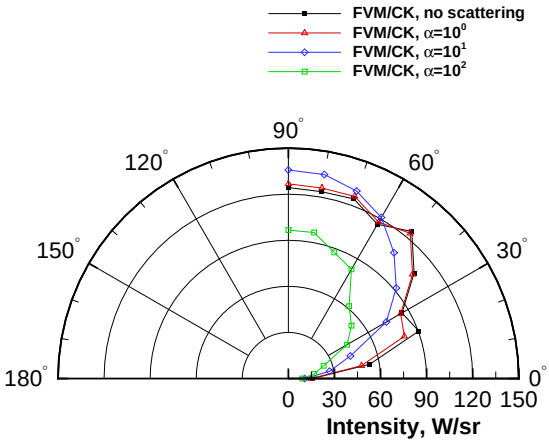

Figure 6.5: Radiant intensities of absorbing, emitting and isotropically scattering plume for $\alpha = 0$, 1, 10, and 100, spectral range 2000 – 5000 cm^{-1}

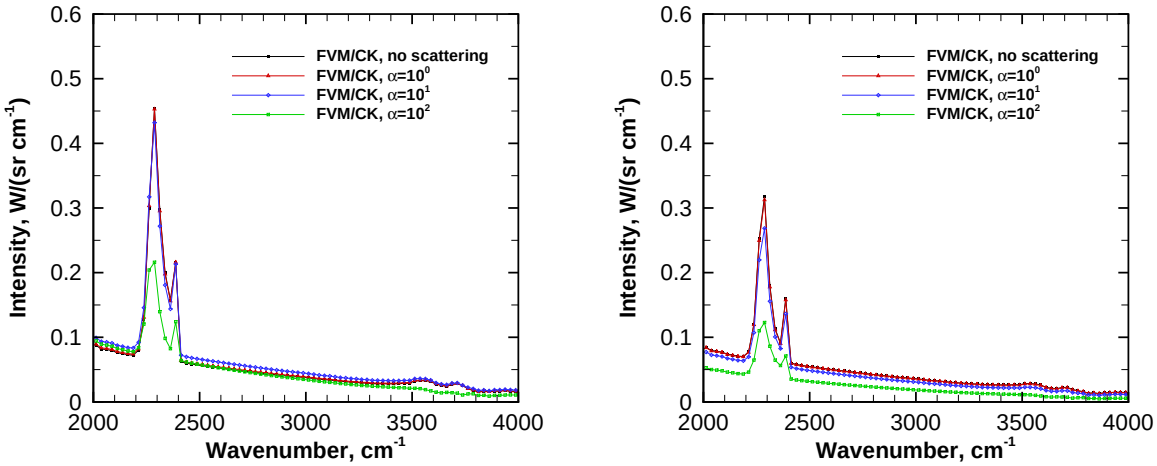

(a) (b)

Figure 6.6: IR spectra of absorbing, emitting and isotropically scattering plume for $\alpha = 0$, 1, 10, and 100, (a) $\theta = 90°$, (b) $\theta = 40°$

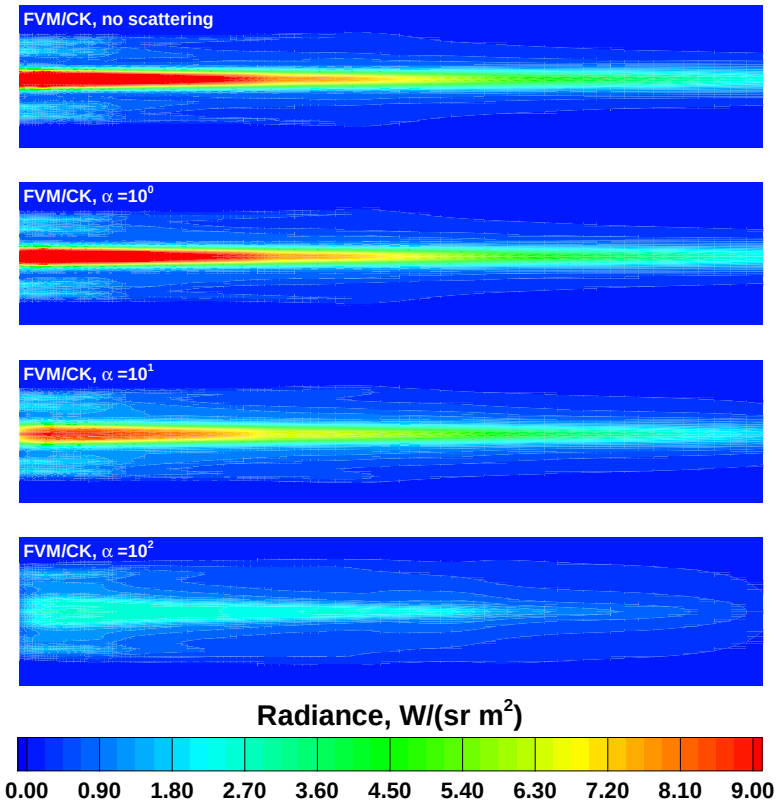

Figure 6.7: Absorbing, emitting and isotropically scattering plume radiances for $\alpha = 0$, 1, 10, and 100, $\theta = 90°$, spectral range 2375 – 2400 cm^{-1}

In the presence of scattering by particles radiative energy within the plume's medium tends to be redistributed. This trend is clearly be seen in Figs. 6.5 and 6.6 in which the angular dependency of plume IR emission varies with α. For example, if $\alpha = 10$, the plume emits more IR radiation at $\theta = 90°$ comparing to the nonscattering case.

A significant reduction in IR signature is observed when the optical thickness (for scattering) becomes very large ($\alpha = 100$). This is likely due to the fact that an increasing scattering opacity makes radiative transfer in participating media more local and the diffusion limit for radiation is reached, just like in the case of increasing absorption opacity [165]. In Fig. 6.7, which shows a comparison between the IR images obtained for the CO_2 "blue spike" region, the increase in scattering opacity appears to significantly reduce the predicted radiance of the exhaust plume viewed at $\theta = 90°$.

Table 6.1: Comparison of maximum number of iterations and CPU time for cases with different scattering opacities of the model plume

α	Maximum iterations	CPU time, s
0	2	326711.8
1	9	1136404.4
10	30	3102842.5
100	379	35639692.8

How the scattering opacity (or equivalently, α value) affects the computational costs in the present FVM/CK calculations is demonstrated in Table 6.1. When the scattering opacity is zero ($\alpha = 0$), the medium is nonscattering and the angular directions in FVM are decoupled. This leads to the number of iterations required to reach the converged solution to be 2 (actually, in nonscattering problems, only a single iteration loop is required to obtain a converged FVM solution; the second iteration is however needed to check the convergence). The maximum number of iterations (i.e., the maximum value over all the narrow bands and quadrature points) increases with increasing α. This is to be expected because the intensities within each control solid angle become strongly coupled to each other (through the source term in the discretized RTE).

The CPU time increases dramatically with scattering opacity, thereby demonstrating the importance of a parallel implementation of the FVM. A parallelization strategy based on decomposition of solution domain by angular direction (see, e.g., the work [169]) was employed in the current study. The simulations were performed on a compute server with four Intel Xeon E5-4617 hexa-core 2.90 GHz CPUs. The FVM solver was run in parallel using all the 24 processors. The calculation for the case of $\alpha = 100$ took approximately 18 days. This is the most challenging computational task performed in the present work.

In practical scattering plume signature problems, the computational time can be reduced by decreasing the number of control volumes in the spatial grid, by using a coarser angular grid, and/or by utilizing a lower-order quadrature scheme for CK. Note also that in Table 6.1 the CPU time is reported for the spectral grid consisting of 101 nodes (full spectral range, see Section 5.2).

6.4.3 Anisotropic Scattering

A number of FVM calculations using the Henyey-Greenstein scattering phase function, Eq. (3.57), are performed here in order to investigate the effect of anisotropy on the predicted directional radiation signature from the plume. The Henyey-Greenstein phase function is implemented with various values of $\bar{\mu}$, namely 0.5 (forward scattering), 0.86 (strong forward scattering), and -0.86 (strong backward scattering) (see Fig. 3.11). The phase function is evaluated numerically using 5×5 solid sub-control angles for good accuracy [170]. During this numerical experiment the values of $f_{v,j}$ and α are kept constant, i.e. $f_{v,j} = 0.5 \times 10^{-6}$ and $\alpha = 10$.

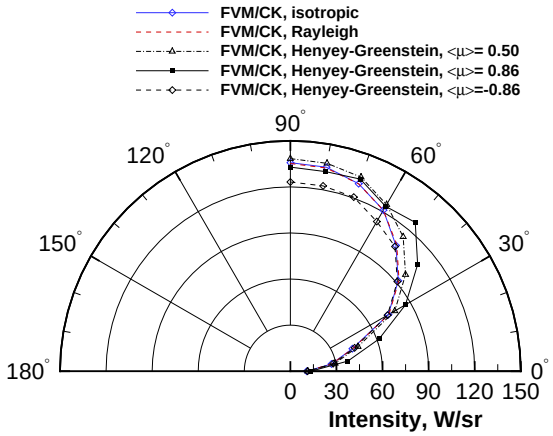

Figure 6.8: Total plume IR emission versus aspect angle resulting from the use of the FVM and various scattering phase functions ($f_{v,j} = 0.5 \times 10^{-6}$, $\alpha = 10$, spectral region 2000 – 5000 cm^{-1})

Fig. 6.8 shows the plume IR radiation integrated in the spectral range 2000 – 5000 cm^{-1} versus aspect angle. The results for the anisotropic scattering plume are compared with those obtained using phase functions for isotropic and Rayleigh scattering (evaluated analytically). Since the phase function for Rayleigh scattering does not deviate too strongly from isotropic scattering (see Fig. 3.11) [23], no difference is observed between the isotropic and Rayleigh scattering cases.

As can be seen from Fig. 6.8, anisotropic scattering plays a significant role in the radiative transfer in the plume's medium. When backward scattering dominates ($\bar{\mu} = -0.86$), the medium transfers less radiative energy than the isotropic medium. Consequently, the simulation data show a reduction in the total plume IR emission, especially for the aspect 90 to 50 deg. As $\bar{\mu}$ is increased, the medium transfers more radiative energy than the isotropic medium. An enhancement in the plume IR emission is then predicted.

Figs. 6.9 and 6.10 indicate the same effect of the degree of anisotropy associated with the Henyey-Greenstein phase function. When compared to the isotropic scattering plume, the backward scattering phase function reduces the IR signature. The forward scattering phase function enhances the IR signature of the plume.

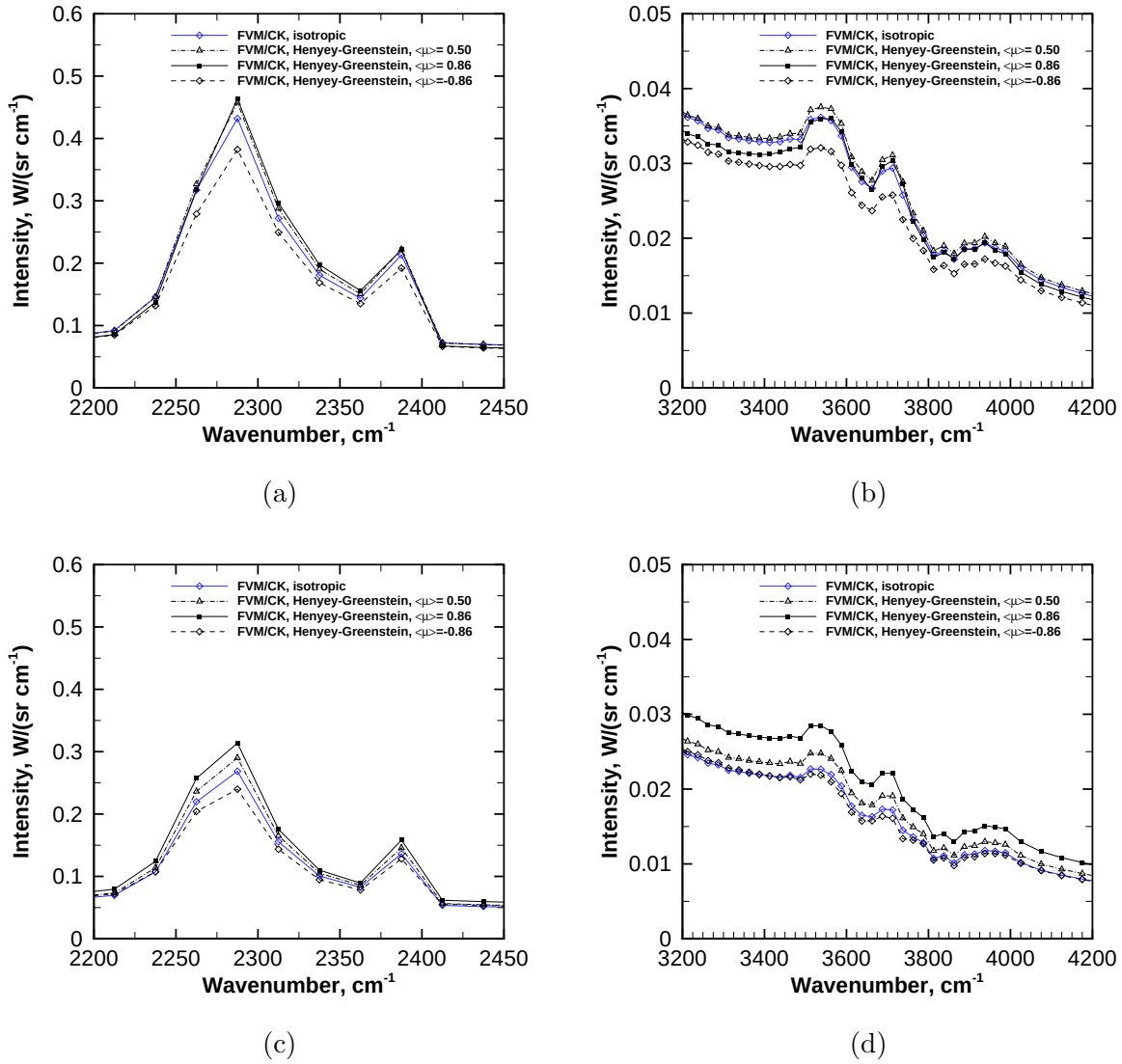

Figure 6.9: Effects of anisotropic scattering on the plume spectra between 2200 and 2450 cm^{-1} (4.3-μm band of CO_2) and between 3200 and 4200 cm^{-1} (2.7-μm band of CO_2/H_2O); results of the calculations using the FVM with isotropic and Henyey-Greenstein phase functions ($f_{v,j} = 0.5 \times 10^{-6}$, $\alpha = 10$) for two aspect angles: (a) 4.3-μm band, $\theta = 90°$, (b) 2.7-μm band, $\theta = 90°$, (c) 4.3-μm band, $\theta = 40°$, (d) 2.7-μm band, $\theta = 40°$

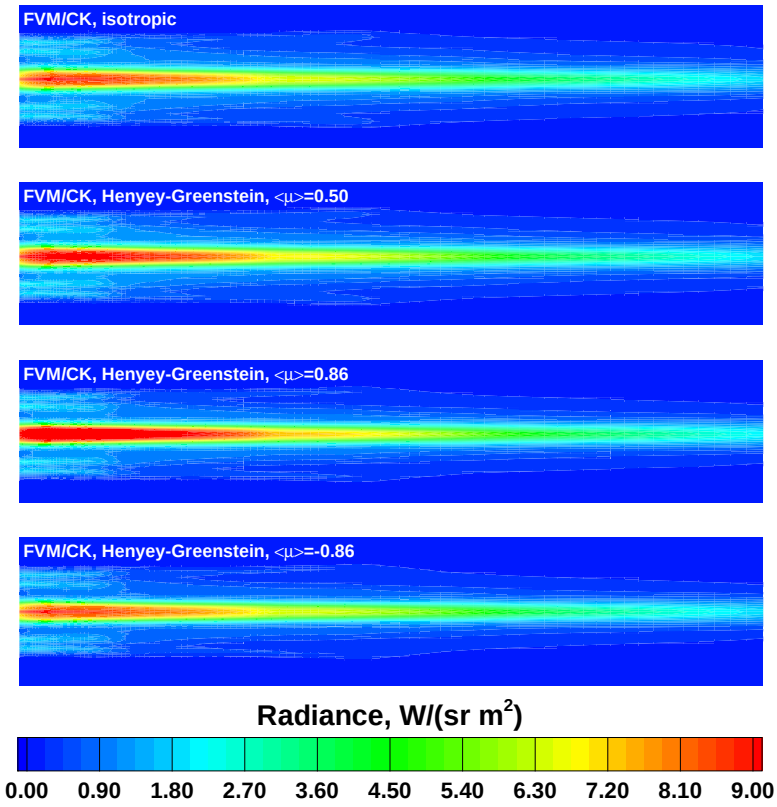

Figure 6.10: Plume IR images computed by the FVM using Henyey-Greenstein and isotropic phase functions ($f_{v,j} = 0.5 \times 10^{-6}$, $\alpha = 10$, $\theta = 90°$, spectral region 2375 – 2400 cm^{-1})

6.5 Summary

It has been demonstrated by means of performing several numerical studies using the FVM that radiation scattering by particles can have significant effects on the IR signature from plumes. Although not important for realistic aircraft engine exhausts, which typically contain soot at relatively low concentrations (up to 0.25 ppbv at MTO according to the data reported in the open literature), these effects were found to be pronounced in the model radiation problems considered in this chapter. Specifically, an increase in soot volume fraction by a factor of 10^3 results in the enhancement of the total plume IR emission by approximately 100%. When compared to the nonscattering case, isotropic scattering by (model) particles tends to redistribute radiative energy within the plume's medium at moderate optical thickness (for scattering). When the optical thickness becomes very large, the presence of scattering results in a reduction in IR signature, especially for the broadside viewed plume. As the scattering opacity is increased, the radiative intensities become strongly coupled. The number of iterations needed to achieve the converged solution for each narrow band and, therefore, the CPU time of overall FVM computations are increased. Calculations using the Henyey-Greenstein phase function with various asymmetry factors have been conducted to study the effect of scattering anisotropy. It was shown that the backward scattering phase function reduces the IR signature, whereas the forward scattering phase function enhances it.

Chapter 7

Conclusions

The modeling of IR radiation from exhaust plumes of aerospace vehicles is an important aspect for various engineering applications. Conventional methods used to predict IR signatures from plumes are based upon SNB models which formulate the radiative properties of exhaust gas in terms of the gaseous column transmissivity averaged over a narrow band. This technique has been implemented in many codes such as NIRATAM.

The most significant shortcoming of the conventional approach is the incompatibility with scattering by particles that cannot be eliminated without using additional approximate assumptions. Errors associated with those assumptions are difficult to ascertain. In addition, in scattering media, the radiative transfer becomes essentially three-dimensional. Consequently, situations with scattering cannot be treated rigorously by employing 1D line-of-sight radiance calculations as in gaseous radiation.

In the present work, the above difficulties of the conventional technique have been overcome. This was achieved by using the FVM for numerical calculation of radiative heat transfer coupled with the CK method for modeling of the spectral radiative properties of mixtures of exhaust gas with air.

The FVM is the most general RTE solution method. This method was historically developed to fit the finite volume approach of CFD in order to solve fluid flow problems in which radiation is an important heat transfer mode. The method provides strict conservation of radiative energy, shares the same computational grid, can be applied to complex geometries, etc. Although suffering from discretization errors (which are encountered in all numerical methods), the FVM is capable of producing accurate numerical results with fine spatial and angular grids.

In the current research, the FVM has been extended to the calculation of directional thermal emissions from absorbing, emitting, and scattering media at high temperature. It has been demonstrated that this method can be applied to plume IR signature prediction problems. The FVM is a 3D approach and it therefore treats radiation transport in scattering plumes in a rigorous manner without involving any approximation assumptions.

The CK method formulates the gaseous spectral properties in terms of the absorption coefficient, and so it can readily be incorporated into the FVM scattering model. The incompatibility with scattering of conventional SNB models is therefore eliminated. Test problem simulations performed have demonstrated that in comparison with exact LBL computations, the CK method provides fairly accurate results for narrow-band radiances along a LOS through a typical aircraft plume.

The newly developed FVM/CK approach has been applied to predict intrinsic (source) IR emissions from the plume of a full-scale mixed turbofan engine running at MTO thrust. Nonscattering (gas only) plume calculations were carried out in order to demonstrate that the method is capable of accurately modeling the directional IR characteristics from the plume. It has been shown that the FVM/CK is able to provide physically consistent results when simulating directional IR emissions of jet exhausts loaded with soot and anisotropically scattering particles.

All computations in the current study have been conducted with a new radiation prediction software package called JERAD. This software includes the FVM/CK approach as well as the conventional RT/SNB plume signature predictive technique. The user can choose from various models and algorithms (for instance, for SNB calculations, the models by Goody and Malkmus are available which are implemented with the SNB model parameters from NASA, ONERA, and EM2C; for CK calculations, various interpolation methods in p–T–x space and different quadrature schemes provided by the SRCS spectral module can be chosen). The simulations can be performed in either serial or parallel mode.

The development and verification of JERAD took more than six years and has resulted in a robust code applicable to practical engineering computations. The construction of the program is flexible so that new models and methods can easily be implemented (e.g., a radiative property model for Al_2O_3 particles).

The FVM/CK approach suggested within the framework of the work is not restricted to exhausts from aircraft engines. The method and developed computer software can surely be applied to predictions of thermal radiation from rocket motor exhaust plumes, and wakes.

Further development of the new FVM/CK model may involve the following.

In this study, the simplest step scheme was used as the spatial differencing scheme. While being numerically stable, this scheme results in strong smearing of the intensity field (false scattering). Therefore, to reduce false scattering, higher-order schemes (HRS) have to be employed. In order to reduce the ray effect, which is a consequence of directional discretization in the FVM, unstructured angular grids may be used.

The FVM was implemented with uniform intensity within each control solid angle. It was found that such an implementation, which is adequate for computing total radiative quantities, is likely to be the reason of “wiggles” in the predicted plume radiant intensities considered as a function of aspect angle. Therefore, to improve the prediction accuracy of plume directional emissions, the standard FVM has to be modified. This

can be done by introducing a directional interpolation procedure for cases when the LOS is not aligned with the average solid angle direction vector.

Alternatively a method can be used in which the FVM is assumed to be applied to the calculation of the source term in the RTE. After the source terms are calculated, a conventional RT solver is used to obtain the radiation intensities along many lines-of-sight through the plume in a given direction. The very first results of this method referred to as MOC–FVM may be found in the paper [138]. The method is however far from completeness and requires further development.

Plume emissions transmitted through the atmosphere are often of interest in practical thermal signature prediction problems. Radiative transfer computations for such problems involve the evaluation of atmospheric transmittance (if an uncorrelated method is employed). The benefit of using the presently developed FVM based approach is that the source IR radiation from a scattering plume can be computed separately. The apparent IR signature is then obtained by multiplying the predicted hot gas spectra from the plume by cold gas atmospheric transmittance that can be computed by an atmospheric transmission software tool such as MODTRAN.

Since the CK method fails for IR long-range sensing of high-temperature plumes, fictitious gas spectral models, such as SNBFG and CKFG, have to be utilized. These models were not considered in the present study.

The plume IR emission is only a part of overall radiation from aircraft. The consideration of complete radiation pattern requires inclusion of other emission sources such as exhaust nozzles. This imposes additional challenges on performing radiation computations as the radiative transfer processes in the medium bounded by nozzle walls and plume medium are coupled.

The suggested improvements and proposals can be subject to future research.

Bibliography

[1] F. S. Simmons. *Rocket Exhaust Plume Phenomenology*. The Aerospace Press, El Segundo, California, 2000.

[2] G. A. Rao and S. P. Mahulikar. Integrated review of stealth technology and its role in airpower. *The Aeronautical Journal*, 106(1066):629–641, 2002.

[3] S. P. Mahulikar, H. R. Sonawane, and G. A. Rao. Infrared signature studies of aerospace vehicles. *Progress in Aerospace Sciences*, 43(7–8):218–245, 2007.

[4] R. Dirscherl. Plume radiation. In *Rocket Motor Plume Technology*, AGARD-LS-188, pages 6–1 – 6–47. Advisory Group for Aerospace Research & Development, June 1993.

[5] S. S. Heragu, K. V. L. Rao, and B. N. Raghunandan. Generalized model for infrared perception from an engine exhaust. *Journal of Thermophysics and Heat Transfer*, 16(1):68–76, 2002.

[6] K. Beier and E. Lindermeir. Comparison of line-by-line and molecular band IR modeling of high altitude missile plume. *Journal of Quantitative Spectroscopy and Radiative Transfer*, 105(1):111–127, 2007.

[7] M. A. Noah, J. A. Kristl, J. W. Schroeder, and B. P. Sandford. NIRATAM – NATO infrared air target model. In *Proceedings of SPIE*, volume 1479: Surveillance Technologies, pages 275–282, August 1991.

[8] M. Johansson and M. Dalenbring. SIGGE, a prediction tool for aeronautical IR signatures, and its applications. In *Proceedings of the 9th AIAA/ASME Joint Thermophysics and Heat Transfer Conference*, San Francisco, June 2006. AIAA 2006-3276.

[9] E. Coiro, C. Chatelard, G. Durand, S. Langlois, and J. P. Martinenq. Experimental validation of an aircraft infrared signature code for commercial airliners. In *Proceedings of the 43rd AIAA Thermophysics Conference*, New Orleans, June 2012. AIAA 2012-3190.

[10] E. Lindermeir and M. Rütten. Infrarotsignaturbewertung von agilen und hoch gepfeilten Flugzeugkonfigurationen. Deutscher Luft- und Raumfahrtkongress 2015, 22–24 September 2015. Rostock, Germany.

[11] R. A. Reed, D. G. Brown, R. S. Hiers III, B. K. Cromwell, and V. A. Zaccardi. Compatibility of infrared band models with scattering. *Journal of Thermophysics and Heat Transfer*, 8(2):208–215, 1994.

[12] S. T. Surzhikov. The use of Monte Carlo simulation methods to calculate the radiation of jets of combustion products in view of rotational spectral structure. *High Temperature*, 41(5):694–707, 2003.

[13] F. Liu, G. J. Smallwood, and Ö. L. Gülder. Application of statistical narrow-band model to three-dimensional absorbing-emitting-scattering media. *Journal of Thermophysics and Heat Transfer*, 13(3):285–291, 1999.

[14] J.-B. Pautrizel, A. Roblin, P. Perez, and V. Rialland. Absorption-scattering coupling for the infrared signature of an aluminized solid rocket motor. In *Proceedings of the 6th International Symposium on Radiative Transfer*, Antalya, Turkey, June 2010.

[15] JANNAF Handbook. Rocket exhaust plume technology, Chapter 3: Rocket exhaust plume radiation. Chemical Propulsion Information Agency, May 1980. CPIA Publication 263.

[16] C. B. Ludwig, W. Malkmus, J. Walker, M. Slack, and R. Reed. The standard infrared radiation model. In *Proceedings of the 16th AIAA Thermophysics Conference*, Palo Alto, June 1981. AIAA 1981-1051.

[17] H. F. Nelson. Influence of scattering on infrared signatures of rocket plumes. *Journal of Spacecraft and Rockets*, 21(5):508–510, 1984.

[18] H. F. Nelson. Influence of particulates on infrared emission from tactical rocket exhausts. *Journal of Spacecraft and Rockets*, 21(5):425–432, 1984.

[19] Yu. Plastinin, G. Karabdzhak, B. Khmelinin, G. Baula, and A. Rodionov. Ultraviolet, visible and infrared spectra modeling for solid and liquid-fuel rocket exhausts. In *Proceedings of the 39th Aerospace Sciences Meeting and Exhibit*, Reno, January 2001. AIAA 2001-0660.

[20] L. A. Dombrovsky and L. G. Barkova. Solving the two-dimensional problem of thermal-radiation transfer in an anisotropically scattering medium using the finite element method. *Teplofizika Vysokikh Temperatur (High Temperature)*, 24 (4):762–769, 1986. In Russian.

[21] L. A. Dombrovsky and W. Lipiński. A combined P_1 and Monte Carlo model for multidimensional radiative transfer problems in scattering media. *Computational Thermal Sciences*, 2(6):549–560, 2010.

[22] L. A. Dombrovsky. The use of transport approximation and diffusion-based models in radiative transfer calculations. *Computational Thermal Sciences*, 4(4):297–315, 2012.

[23] M. F. Modest. *Radiative Heat Transfer*. Academic Press, Elsevier Science, San Diego, California, 2nd edition, 2003.

[24] E. I. Vitkin, V. G. Karelin, A. A. Kirillov, A. S. Suprun, and Ju. V. Khadyka. A physico-mathematical model of rocket exhaust plumes. *International Journal of Heat and Mass Transfer*, 40(5):1227–1241, 1997.

[25] G. Cai, D. Zhu, and X. Zhang. Numerical simulation of the infrared radiative signatures of liquid and solid rocket plumes. *Aerospace Science and Technology*, 11(6):473–480, 2007.

[26] H. F. Nelson and E. O. Tucker. Boron slurry-fueled jet engine exhaust plume infrared signatures. *Journal of Spacecraft and Rockets*, 23(5):527–533, 1986.

[27] Yu. A. Plastinin, N. A. Anfimov, G. G. Baula, G. F. Karabadzhak, B. A. Khmelinin, and A. V. Rodionov. Modeling of aluminum oxide particle radiation in a solid propellant motor exhaust. In *Proceedings of the 31st AIAA Thermophysics Conference*, New Orleans, June 1996. AIAA 1996-1879.

[28] S. P. Mahulikar, G. A. Rao, S. K. Sane, and A. G. Marathe. Aircraft plume infrared signature in nonafterburning mode. *Journal of Thermophysics and Heat Transfer*, 19(3):413–415, 2005.

[29] G. A. Rao and S. P. Mahulikar. Aircraft powerplant and plume infrared signature modelling and analysis. In *Proceedings of the 43rd AIAA Aerospace Sciences Meeting and Exhibit*, Reno, January 2005. AIAA 2005-221.

[30] A. Devir, A. Lessin, M. Lev, J. Stricker, S. Yaniv, Y. Cohen, Y. Kanelbaum, G. Avital, L. Gamss, J. Macales, B. Trieman, and A. Sternlieb. Comparison of calculated and measured radiation from a rocket motor plume. In *Proceedings of the 39th AIAA Aerospace Sciences Meeting and Exhibit*, Reno, January 2001. AIAA 2001-0358.

[31] G. Avital, Y. Cohen, L. Gamss, Y. Kanelbaum, J. Macales, B. Trieman, S. Yaniv, M. Lev, J. Stricker, and A. Sternlieb. Experimental and computational study of infrared emission from underexpanded rocket exhaust plumes. *Journal of Thermophysics and Heat Transfer*, 15(4):377–383, 2001.

[32] Yu. A. Plastinin, G. F. Karabadzhak, B. A. Khmelinin, G. G. Baula, and A. V. Rodionov. Advanced model for soot radiation in the plume. In *Proceedings of the 40th AIAA Aerospace Sciences Meeting and Exhibit*, Reno, January 2002. AIAA 2002-0798.

[33] Yu. A. Plastinin, G. F. Karabadzhak, B. A. Khmelinin, G. G. Baula, and A. V. Rodionov. Modeling of OH ultraviolet radiation in Atlas motor plume and comparison with recent experimental data. In *Proceedings of the 41st AIAA Aerospace Sciences Meeting and Exhibit*, Reno, January 2003. AIAA 2003-507.

[34] A. A. Alexeenko, N. E. Gimelshein, D. A. Levin, S. F. Gimelshein, J. S. Hong, T. Schilling, R. J. Collins, R. Rao, and G. Candler. Modeling of radiation in the Atlas plume-flow. In *Proceedings of the 39th AIAA Aerospace Sciences Meeting and Exhibit*, Reno, January 2001. AIAA 2001-0355.

[35] J. S. Hong, D. A. Levin, R. J. Collins, J. Emery, and A. Tietjen. Comparison of Atlas ground based plume imagery with chemically reacting flow solutions. In *Proceedings of the 32nd AIAA Thermophysics Conference*, Atlanta, June 1997. AIAA 1997-2537.

[36] S. T. Surzhikov. Direct simulation Monte-Carlo algorithms for the rocket exhaust plumes emissivity prediction. In *Proceedings of the 40th AIAA Aerospace Sciences Meeting and Exhibit*, Reno, January 2002. AIAA 2002-0795.

[37] S. T. Surzhikov. Monte Carlo simulation of plumes spectral emission. In *Proceedings of the 36th AIAA Thermophysics Conference*, Orlando, June 2003. AIAA 2003-3895.

[38] S. T. Surzhikov. Three-dimensional model of the spectral emissivity of light-scattering exhaust plumes. *High Temperature*, 42(5):763–775, 2004.

[39] Y. Shuai, S. K. Dong, and H. P. Tan. Simulation of the infrared radiation characteristics of high-temperature exhaust plume including particles using the backward Monte Carlo method. *Journal of Quantitative Spectroscopy and Radiative Transfer*, 95(2):231–240, 2005.

[40] S. W. Baek and M. Y. Kim. Analysis of radiative heating of a rocket plume base with the finite-volume method. *International Journal of Heat and Mass Transfer*, 40(7):1501–1508, 1997.

[41] R. Decher. Infrared emissions from turbofans with high aspect ratio nozzles. *Journal of Aircraft*, 18(12):1025–1031, 1981.

[42] G. J. Banken, W. M. Cornette, and K. M. Gleason. Investigation of infrared characteristics of three generic nozzle concepts. In *Proceedings of the 16th AIAA/SAE/ASME Joint Propulsion Conference*, Hartford, June–July 1980. AIAA 1980-1160.

[43] Y. Sugiyama, K. Adachi, and I. Tokaji. Aspect-ratio effects on infrared radiation intensity of 2-D nozzle exhaust plume. In *Proceedings of the 10th International Symposium on Air Breath Engines*, pages 1111–1115, 1991. ISABE 91-7119.

[44] J. Dix, A. J. Saddington, K. Knowles, and M. A. Richardson. Infra-red signature reduction study on a small-scale jet engine. *The Aeronautical Journal*, 109(1092): 83–88, 2005.

[45] K. Knowles and A. J. Saddington. A review of jet mixing enhancement for aircraft propulsion applications. *Proceedings of the Institution of Mechanical Engineers, Part G: Journal of Aerospace Engineering*, 220(2):103–127, 2006.

[46] A. Sventitskiy and Ch. Mundt. A study of the infrared emission properties from full-scale exhaust plumes. *International Review of Mechanical Engineering*, 4(4): 425–432, 2010.

[47] A. Sventitskiy and Ch. Mundt. Simulation of the infrared emission from non-scattering aircraft engine exhaust plumes using statistical narrowband models in conjunction with model parameters based on the modern spectroscopic data. In *Proceedings of the 43rd AIAA Thermophysics Conference*, New Orleans, June 2012. AIAA 2012-3315.

[48] S. T. Surzhikov. *Thermal Radiation of Gases and Plasmas*. The Bauman University Publishing House, Moscow, 2004. In Russian.

[49] W. A. Fiveland and J. P. Jessee. Comparison of discrete ordinates formulations for radiative heat transfer in multidimensional geometries. *Journal of Thermophysics and Heat Transfer*, 9(1):47–54, 1995.

[50] F. Liu, H. A. Becker, and A. Pollard. Spatial differencing schemes of the discrete-ordinates method. *Numerical Heat Transfer, Part B: Fundamentals*, 30(1):23–43, 1996.

[51] G. D. Raithby and E. H. Chui. A finite-volume method for predicting a radiant heat transfer in enclosures with participating media. *ASME Journal of Heat Transfer*, 112(2):415–423, 1990.

[52] E. H. Chui, G. D. Raithby, and P. M. J. Hughes. Prediction of radiative transfer in cylindrical enclosures with the finite volume method. *Journal of Thermophysics and Heat Transfer*, 6(4):605–611, 1992.

[53] E. H. Chui and G. D. Raithby. Computation of radiant heat transfer on a nonorthogonal mesh using the finite-volume method. *Numerical Heat Transfer, Part B: Fundamentals*, 23(3):269–288, 1993.

[54] J. C. Chai, H. S. Lee, and S. V. Patankar. Finite volume method for radiation heat transfer. *Journal of Thermophysics and Heat Transfer*, 8(3):419–425, 1994.

[55] J. C. Chai, H. S. Lee, and S. V. Patankar. Treatment of irregular geometries using a Cartesian coordinates finite-volume radiation heat transfer procedure. *Numerical Heat Transfer, Part B: Fundamentals*, 26(2):225–235, 1994.

[56] J. C. Chai, G. Parthasarathy, H. S. Lee, and S. V. Patankar. Finite volume radiative heat transfer procedure for irregular geometries. *Journal of Thermophysics and Heat Transfer*, 9(3):410–415, 1995.

[57] J. Y. Murthy and S. R. Mathur. Finite volume method for radiative heat transfer using unstructured meshes. *Journal of Thermophysics and Heat Transfer*, 12(3): 313–321, 1998.

[58] G. D. Raithby. Discussion of the finite-volume method for radiation, and its application using 3D unstructured meshes. *Numerical Heat Transfer, Part B: Fundamentals*, 35(4):389–405, 1999.

[59] J. C. Chai and S. V. Patankar. Finite-volume method for radiation heat transfer. In *Advances in Numerical Heat Transfer*, volume 2, chapter 4, pages 109–141. Taylor & Francis, 2000.

[60] G. N. Lygidakis and I. K. Nikolos. Using the finite-volume method and hybrid unstructured meshes to compute radiative heat transfer in 3-D geometries. *Numerical Heat Transfer, Part B: Fundamentals*, 62(5):289–314, 2012.

[61] P. Boulet, A. Collin, and J. L. Consalvi. On the finite volume method and the discrete ordinates method regarding radiative heat transfer in acute forward anisotropic scattering media. *Journal of Quantitative Spectroscopy and Radiative Transfer*, 104(3):460–473, 2007.

[62] W. A. Fiveland. Discrete ordinate methods for radiative heat transfer in isotropically and anisotropically scattering media. *ASME Journal of Heat Transfer*, 109 (3):809–812, 1987.

[63] W. A. Fiveland. Three-dimensional radiative heat-transfer solutions by the discrete-ordinates method. *Journal of Thermophysics and Heat Transfer*, 2(4): 309–316, 1988.

[64] C. P. Thurgood, A. Pollard, and H. A. Becker. The T_N quadrature set for the discrete ordinates method. *ASME Journal of Heat Transfer*, 117(4):1068–1070, 1995.

[65] W. A. Fiveland and A. S. Jamaluddin. Three-dimensional spectral radiative heat transfer solutions by the discrete-ordinates method. *Journal of Thermophysics and Heat Transfer*, 5(3):335–339, 1991.

[66] J. C. Chai, S. V. Patankar, and H. S. Lee. Evaluation of spatial differencing practices for the discrete-ordinates method. *Journal of Thermophysics and Heat Transfer*, 8(1):140–144, 1994.

[67] N. Berour, D. Lacroix, and G. Jeandel. Radiative and conductive heat exchanges in high-temperature glass melt with the finite-volume method approach. Influence of several spatial differencing schemes on RTE solution. *Numerical Heat Transfer, Part A: Applications*, 49(6):567–588, 2006.

[68] H. K. Versteeg and W. Malalasekera. *An Introduction to Computational Fluid Dynamics. The Finite Volume Method*. Pearson Education, Harlow, Essex, England, 2nd edition, 2007.

[69] J. P. Jessee and W. A. Fiveland. Bounded, high-resolution differencing schemes applied to the discrete ordinates method. *Journal of Thermophysics and Heat Transfer*, 11(4):540–548, 1997.

[70] R. Capdevila, C. D. Pérez-Segarra, and A. Oliva. Development and comparison of different spatial numerical schemes for the radiative transfer equation resolution using three-dimensional unstructured meshes. *Journal of Quantitative Spectroscopy and Radiative Transfer*, 111(2):264–273, 2010.

[71] M. S. Darwish and F. H. Moukalled. Normalized variable and space formulation methodology for high-resolution schemes. *Numerical Heat Transfer, Part B: Fundamentals*, 26(1):79–96, 1994.

[72] P. J. Coelho. Bounded skew high-order resolution schemes for the discrete ordinates method. *Journal of Computational Physics*, 175(2):412–473, 2002.

[73] W. F. Godoy and P. E. DesJardin. On the use of flux limiters in the discrete ordinates method for 3D radiation calculations in absorbing and scattering media. *Journal of Computational Physics*, 229(9):3189–3213, 2010.

[74] P. J. Coelho. A comparison of spatial discretization schemes for differential solution methods of the radiative transfer equation. *Journal of Quantitative Spectroscopy and Radiative Transfer*, 109(2):189–200, 2008.

[75] J. C. Chai, H. S. Lee, and S. V. Patankar. Improved treatment of scattering using the discrete ordinates method. *ASME Journal of Heat Transfer*, 116(1):260–263, 1994.

[76] S. H. Kim and K. Y. Huh. A new angular discretization scheme of the finite volume method for 3-D radiative heat transfer in absorbing, emitting and anisotropically scattering media. *International Journal of Heat and Mass Transfer*, 43(7):1233–1242, 2000.

[77] J. C. Chai, H. S. Lee, and S. V. Patankar. Ray effect and false scattering in the discrete ordinates method. *Numerical Heat Transfer, Part B: Fundamentals*, 24 (4):373–389, 1993.

[78] G. D. Raithby. Evaluation of discretization errors in finite-volume radiant heat transfer predictions. *Numerical Heat Transfer, Part B: Fundamentals*, 36(3):241–264, 1999.

[79] M. Y. Kim, S. W. Baek, and J. H. Park. Unstructured finite-volume method for radiative heat transfer in a complex two-dimensional geometry with obstacles. *Numerical Heat Transfer, Part B: Fundamentals*, 39(6):617–635, 2001.

[80] P. J. Coelho. The role of ray effects and false scattering on the accuracy of the standard and modified discrete ordinates methods. *Journal of Quantitative Spectroscopy and Radiative Transfer*, 73(2–5):231–238, 2002.

[81] M. P. Galanin, V. V. Lukin, and V. M. Chechetkin. Methods of radiation transfer equation solution for the astrophysical models. *Keldysh Institute Preprints*, 59, 2010. In Russian.

[82] F. Liu, G. J. Smallwood, and Ö. L. Gülder. Application of the statistical narrow-band correlated-k method to low-resolution spectral intensity and radiative heat transfer calculations – effects of the quadrature scheme. *International Journal of Heat and Mass Transfer*, 43(17):3119–3135, 2000.

[83] A. Soufiani and J. Taine. High temperature gas radiative property parameters of statistical narrow-band model for H_2O, CO_2 and CO, and correlated-K model for H_2O and CO_2. *International Journal of Heat and Mass Transfer*, 40(4):987–991, 1997.

[84] P. Hassanzadeh and G. D. Raithby. Finite-volume solution of the second-order radiative transfer equation: Accuracy and solution cost. *Numerical Heat Transfer, Part B: Fundamentals*, 53(4):374–382, 2008.

[85] L. Ibgui and J.-M. Hartmann. An optimized line by line code for plume signature calculations—I: model and data. *Journal of Quantitative Spectroscopy and Radiative Transfer*, 75(3):273–295, 2002.

[86] L. Ibgui, A. Valentin, M.-F. Merienne, A. Jenouvrier, J. P. Lux, R. Le Doucen, B. Khalil, and J.-M. Hartmann. An optimized line by line code for plume signature calculations II. Comparisons with measurements. *Journal of Quantitative Spectroscopy and Radiative Transfer*, 74(4):401–415, 2002.

[87] D. K. Edwards. Molecular gas band radiation. In *Advances in Heat Transfer*, volume 12, pages 115–193. Academic Press, 1976.

[88] T. F. Smith, Z. F. Shen, and J. N. Friedman. Evaluation of coefficients for the weighted sum of gray gases model. *ASME Journal of Heat Transfer*, 104(4):602–608, 1982.

[89] M. F. Modest. The weighted-sum-of-gray-gases model for arbitrary solution methods in radiative transfer. *ASME Journal of Heat Transfer*, 113(3):650–656, 1991.

[90] M. K. Denison and B. W. Webb. A spectral line-based weighted-sum-of-gray-gases model for arbitrary RTE solvers. *ASME Journal of Heat Transfer*, 115(4): 1004–1012, 1993.

[91] M. K. Denison and B. W. Webb. The spectral line-based weighted-sum-of-gray-gases model in nonisothermal nonhomogeneous media. *ASME Journal of Heat Transfer*, 117(2):359–365, 1995.

[92] M. K. Denison and B. W. Webb. The spectral-line weighted-sum-of-gray-gases model for H_2O/CO_2 mixtures. *ASME Journal of Heat Transfer*, 117(3):788–792, 1995.

[93] V. P. Solovjov and B. W. Webb. SLW modeling of radiative transfer in multicomponent gas mixtures. *Journal of Quantitative Spectroscopy and Radiative Transfer*, 65(4):655–672, 2000.

[94] L. Pierrot, A. Soufiani, and J. Taine. Accuracy of narrow-band and global models for radiative transfer in H_2O, CO_2, and H_2O–CO_2 mixtures at high temperature. *Journal of Quantitative Spectroscopy and Radiative Transfer*, 62(5):523–548, 1999.

[95] M. F. Modest and H. Zhang. The full-spectrum correlated-k distribution for thermal radiation from molecular gas-particulate mixtures. *ASME Journal of Heat Transfer*, 124(1):30–38, 2002.

[96] J.-M. Lamet, Ph. Rivière, M.-Y. Perrin, and A. Soufiani. Narrow-band model for nonequilibrium air plasma radiation. *Journal of Quantitative Spectroscopy and Radiative Transfer*, 111(1):87–104, 2010.

[97] A. Bansal, M. Modest, and D. Levin. k-Distributions for gas mixtures in hypersonic nonequilibrium flows. In *Proceedings of the 48th AIAA Aerospace Sciences Meeting*, Orlando, January 2010. AIAA 2010-234.

[98] J. Taine and A. Soufiani. Gas IR radiative properties: From spectroscopic data to approximate models. In *Advances in Heat Transfer*, volume 33, pages 295–414. Academic Press, 1999.

[99] J. Koo, R. Goulard, C. B. Ludwig, and W. Malkmus. Radiative properties of combustion gases. In *Proceedings of the 14th AIAA Thermophysics Conference*, Orlando, June 1979. AIAA 1979-1041.

[100] W. Malkmus. Random Lorentz band model with exponential-tailed S^{-1} line-intensity distribution function. *Journal of the Optical Society of America*, 57 (3):323–329, 1967.

[101] S. T. Surzhikov. Spectral and narrow band directional emissivity of light-scattering and non-scattering volumes. In *Proceedings of the 8th AIAA/ASME Joint Thermophysics and Heat Transfer Conference*, St. Louis, June 2002. AIAA 2002-3324.

[102] C. B. Ludwig, W. Malkmus, J. E. Reardon, and J. A. L. Thomson. Handbook of infrared radiation from combustion gases. SP-3080, NASA, January 1973.

[103] C. D. Rodgers and A. P. Williams. Integrated absorption of a spectral line with the Voigt profile. *Journal of Quantitative Spectroscopy and Radiative Transfer*, 14(4):319–323, 1974.

[104] Ph. Rivière and A. Soufiani. Generalized Malkmus line intensity distribution for CO_2 infrared radiation in Doppler broadening regime. *Journal of Quantitative Spectroscopy and Radiative Transfer*, 112(3):475–485, 2011.

[105] A. Soufiani, F. André, and J. Taine. A fictitious-gas based statistical narrow-band model for IR long-range sensing of H_2O at high temperature. *Journal of Quantitative Spectroscopy and Radiative Transfer*, 73(2–5):339–347, 2002.

[106] A. Soufiani, J. M. Hartmann, and J. Taine. Validity of band-model calculations for CO_2 and H_2O applied to radiative properties and conductive-radiative transfer. *Journal of Quantitative Spectroscopy and Radiative Transfer*, 33(3):243–257, 1985.

[107] M. F. Modest and R. J. Riazzi. Assembly of full-spectrum k-distributions from a narrow-band database; effects of mixing gases, gases and nongray absorbing particles, and mixtures with nongray scatterers in nongray enclosures. *Journal of Quantitative Spectroscopy and Radiative Transfer*, 90(2):169–189, 2005.

[108] G. Shi, N. Xu, B. Wang, T. Dai, and J. Zhao. An improved treatment of overlapping absorption bands based on the correlated k distribution model for thermal infrared radiative transfer calculations. *Journal of Quantitative Spectroscopy and Radiative Transfer*, 110(8):435–451, 2009.

[109] L. S. Rothman, C. P. Rinsland, A. Goldman, S. T. Massie, D. P. Edwards, J.-M. Flaud, A. Perrin, C. Camy-Peyret, V. Dana, J.-Y. Mandin, J. Schroeder, A. McCann, R. R. Gamache, R. B. Wattson, K. Yoshino, K. V. Chance, K. W. Jucks, L. R. Brown, V. Nemtchinov, and P. Varanasi. The HITRAN molecular spectroscopic database and HAWKS (HITRAN atmospheric workstation): 1996 edition. *Journal of Quantitative Spectroscopy and Radiative Transfer*, 60(5):665–710, 1998.

[110] L. S. Rothman, I. E. Gordon, Y. Babikov, A. Barbe, D. Chris Benner, P. F. Bernath, M. Birk, L. Bizzocchi, V. Boudon, L. R. Brown, A. Campargue, K. Chance, E. A. Cohen, L. H. Coudert, V. M. Devi, B. J. Drouin, A. Fayt, J.-M. Flaud, R. R. Gamache, J. J. Harrison, J.-M. Hartmann, C. Hill, J. T. Hodges, D. Jacquemart, A. Jolly, J. Lamouroux, R. J. Le Roy, G. Li, D. A. Long, O. M. Lyulin, C. J. Mackie, S. T. Massie, S. Mikhailenko, H. S. P. Müller, O. V. Naumenko, A. V. Nikitin, J. Orphal, V. Perevalov, A. Perrin, E. R. Polovtseva, C. Richard, M. A. H. Smith, E. Starikova, K. Sung, S. Tashkun, J. Tennyson, G. C. Toon, Vl. G. Tyuterev, and G. Wagner. The HITRAN2012 molecular spectroscopic database. *Journal of Quantitative Spectroscopy and Radiative Transfer*, 130:4–50, November 2013.

[111] L. S. Rothman, I. E. Gordon, R. J. Barber, H. Dothe, R. R. Gamache, A. Goldman, V. I. Perevalov, S. A. Tashkun, and J. Tennyson. HITEMP, the high-temperature molecular spectroscopic database. *Journal of Quantitative Spectroscopy and Radiative Transfer*, 111(15):2139–2150, 2010.

[112] S. A. Tashkun, V. I. Perevalov, J-L. Teffo, A. D. Bykov, and N. N. Lavrentieva. CDSD-1000, the high-temperature carbon dioxide spectroscopic databank. *Journal of Quantitative Spectroscopy and Radiative Transfer*, 82(1–4):165–196, 2003.

[113] S. A. Tashkun and V. I. Perevalov. CDSD-4000: High-resolution, high-temperature carbon dioxide spectroscopic databank. *Journal of Quantitative Spectroscopy and Radiative Transfer*, 112(9):1403–1410, 2011.

[114] B. A. Khmelinin and Yu. A. Plastinin. Emissive and absorptive properties of H_2O, CO_2, CO and HCl molecules at temperatures of 300-3000 K. *TsAGI Transactions*, 1656:102–147, 1975. In Russian.

[115] S. J. Young. Band model parameters for the 2.7-μm bands of H_2O and CO_2 in the 100 to 3000°K temperature range. The Aerospace Corporation, El Segundo, California, July 1975. SAMSO-TR-75-209.

[116] Ph. Rivière and A. Soufiani. Updated band model parameters for H_2O, CO_2, CH_4 and CO radiation at high temperature. *International Journal of Heat and Mass Transfer*, 55(13–14):3349–3358, 2012.

[117] P. Perez, A. Boischot, L. Ibgui, and A. Roblin. A spectroscopic database for water vapor adapted to spectral properties at high temperature, and moderate resolution. *Journal of Quantitative Spectroscopy and Radiative Transfer*, 103(2): 231–244, 2007.

[118] E. Lindermeir and K. Beier. HITEMP derived spectral database for the prediction of jet engine exhaust infrared emission using a statistical band model. *Journal of Quantitative Spectroscopy and Radiative Transfer*, 113(12):1575–1593, 2012.

[119] M. F. Modest. Narrow-band and full-spectrum k-distributions for radiative heat transfer—correlated-k vs. scaling approximation. *Journal of Quantitative Spectroscopy and Radiative Transfer*, 76(1):69–83, 2003.

[120] H. Zhang and M. F. Modest. Scalable multi-group full-spectrum correlated-k distributions for radiative transfer calculations. *ASME Journal of Heat Transfer*, 125(3):454–461, 2003.

[121] Q. Fu and K. N. Liou. On the correlated k-distribution method for radiative transfer in nonhomogeneous atmospheres. *Journal of the Atmospheric Sciences*, 49(22):2139–2156, 1992.

[122] S. N. Mikhailenko, Yu. L. Babikov, and V. F. Golovko. Information-calculating system Spectroscopy of Atmospheric Gases. The structure and main functions. *Atmospheric and Oceanic Optics*, 18(9):685–695, 2005.

[123] R. Goody, R. West, L. Chen, and D. Crisp. The correlated-k method for radiation calculations in nonhomogeneous atmospheres. *Journal of Quantitative Spectroscopy and Radiative Transfer*, 42(6):539–550, 1989.

[124] M. F. Gerstell. Obtaining the cumulative k-distribution of a gas mixture from those of its components. *Journal of Quantitative Spectroscopy and Radiative Transfer*, 49(1):15–38, 1993.

[125] F. Liu, G. J. Smallwood, and Ö. L. Gülder. Application of the statistical narrow-band correlated-k method to non-grey gas radiation in CO_2–H_2O mixtures: approximate treatments of overlapping bands. *Journal of Quantitative Spectroscopy and Radiative Transfer*, 68(4):401–417, 2001.

[126] C. Caliot, Y. Le Maoult, M. El Hafi, and G. Flamant. Remote sensing of high temperature H_2O–CO_2–CO mixture with a correlated k-distribution fictitious gas method and the single-mixture gas assumption. *Journal of Quantitative Spectroscopy and Radiative Transfer*, 102(2):304–315, 2006.

[127] C. Caliot, G. Flamant, M. El Hafi, and Y. Le Maoult. Assessment of the single-mixture gas assumption for the correlated k-distribution fictitious gas method in H_2O–CO_2–CO mixture at high temperature. *ASME Journal of Heat Transfer*, 130(10):104501–1–104501–6, 2008.

[128] S. Dembele and J. X. Wen. Investigation of a spectral formulation for radiative heat transfer in one-dimensional fires and combustion systems. *International Journal of Heat and Mass Transfer*, 43(21):4019–4030, 2000.

[129] F. Liu and G. J. Smallwood. An efficient approach for the implementation of the SNB based correlated-k method and its evaluation. *Journal of Quantitative Spectroscopy and Radiative Transfer*, 84(4):465–475, 2004.

[130] S. Dembele and J. X. Wen. Evaluation of a fast correlated-k approach for radiation calculations in combustion systems. *Numerical Heat Transfer, Part B: Fundamentals*, 44(4):365–385, 2003.

[131] A. Wang and M. F. Modest. High-accuracy, compact database of narrow-band k-distributions for water vapor and carbon dioxide. *Journal of Quantitative Spectroscopy and Radiative Transfer*, 93(1–3):245–261, 2005.

[132] J. Cai and M. F. Modest. Improved full-spectrum k-distribution implementation for inhomogeneous media using a narrow-band database. *Journal of Quantitative Spectroscopy and Radiative Transfer*, 141:65–72, July 2014.

[133] G. Pal, A. Wang, and M. F. Modest. A k-distribution-based spectral module for radiation calculations in multi-phase mixtures. In *Proceedings of the ASME 2009 Heat Transfer Summer Conference*, San Francisco, July 2009. HT2009-88245.

[134] G. Pal. *Spectral Modeling of Radiation in Combustion Systems*. PhD thesis, The Pennsylvania State University, May 2010.

[135] Ph. Rivière, A. Soufiani, and J. Taine. Correlated-k and fictitious gas methods for H_2O near 2.7 μm. *Journal of Quantitative Spectroscopy and Radiative Transfer*, 48(2):187–203, 1992.

[136] A. Sventitskiy and Ch. Mundt. Application of the narrowband correlated-k method to numerical simulation of nonscattering exhaust plume IR emissions. In *Proceedings of the 48th AIAA/ASME/SAE/ASEE Joint Propulsion Conference and Exhibit*, Atlanta, July–August 2012. AIAA 2012-4222.

[137] F. Liu, Ö. L. Gülder, G. J. Smallwood, and Y. Ju. Non-gray gas radiative transfer analyses using the statistical narrow-band model. *International Journal of Heat and Mass Transfer*, 41(14):2227–2236, 1998.

[138] A. Sventitskiy and Ch. Mundt. A finite volume based method for narrow-band simulations of thermal radiation from participating media. In *Proceedings of the 11th AIAA/ASME Joint Thermophysics and Heat Transfer Conference*, Atlanta, June 2014. AIAA 2014-2677.

[139] J. Delhay, P. Desgroux, E. Therssen, H. Bladh, P.-E. Bengtsson, H. Hönen, J. D. Black, and I. Vallet. Soot volume fraction measurements in aero-engine exhausts using extinction-calibrated backward laser-induced incandescence. *Applied Physics B: Lasers and Optics*, 95(4):825–838, 2009.

[140] B. Owen and D. S. Lee. Aviation emissions. In *Encyclopedia of Aerospace Engineering*, volume 6, chapter 300, pages 3651–3660. John Wiley & Sons, 2010.

[141] H. Chang and T. T. Charalampopoulos. Determination of the wavelength dependence of refractive indices of flame soot. *Proceedings of the Royal Society of London, Series A: Mathematical and Physical Sciences*, 430(1880):577–591, 1990.

[142] D. N. Trivic, T. J. O'Brien, and C. H. Amon. Modeling the radiation of anisotropically scattering media by coupling Mie theory with finite volume method. *International Journal of Heat and Mass Transfer*, 47(26):5765–5780, 2004.

[143] N. E. Gimelshein, R. B. Lyons, J. G. Reuster, and S. F. Gimelshein. Numerical prediction of ultraviolet radiation from two-phase plumes at high altitudes. *AIAA Journal*, 46(7):1764–1772, 2008.

[144] T.-K. Kim and H. Lee. Effect of anisotropic scattering on radiative heat transfer in two-dimensional rectangular enclosures. *International Journal of Heat and Mass Transfer*, 31(8):1711–1721, 1988.

[145] D. N. Trivic and C. H. Amon. Modeling the 3-D radiation of anisotropically scattering media by two different numerical methods. *International Journal of Heat and Mass Transfer*, 51(11–12):2711–2732, 2008.

[146] Ch. Mundt and J. Lieser. Performance improvement of propulsion systems by optimization of the mixing efficiency and pressure loss of forced mixers. In *Proceedings of the 8th CEAS European Propulsion Forum*, Nottingham, March 2001.

[147] S. F. Saegeler and Ch. Mundt. Advanced numerical simulation of mixing hot core and cold bypass flow in modern propulsion systems with internal lobed forced mixer. In *Proceedings of the 21st AIAA Computational Fluid Dynamics Conference*, San Diego, June 2013. AIAA 2013-2424.

[148] S. F. Saegeler. *Verbesserung der numerischen Simulation der Mischung von Triebwerksstrahlen*. PhD thesis, Universität der Bundeswehr München, March 2014.

[149] J. Trümner and Ch. Mundt. Advanced modelling of turbulent heat-flux in turbofan engines with lobed mixers. In *Proceedings of the 46th AIAA Fluid Dynamics Conference*, Washington, June 2016. AIAA 2016-4389.

[150] S. P. Mahulikar, S. K. Sane, U. N. Gaitonde, and A. G. Marathe. Numerical studies of infrared signature levels of complete aircraft. *The Aeronautical Journal*, 105 (1046):185–192, 2001.

[151] *ANSYS FLUENT User's Guide, Release 14.5*. ANSYS, Inc., Canonsburg, PA, USA, October 2012.

[152] Guide to reference and standard atmosphere models. American Institute of Aeronautics and Astronautics, November 2004. ANSI/AIAA-G-003B-2004.

[153] T. W. Schlatter. Vertical structure of the atmosphere. In *Encyclopedia of Aerospace Engineering*, volume 6, chapter 274, pages 3341–3351. John Wiley & Sons, 2010.

[154] *ANSYS FLUENT Theory Guide, Release 14.5*. ANSYS, Inc., Canonsburg, PA, USA, October 2012.

[155] F. X. Kneizys, L. W. Abreu, G. P. Anderson, J. H. Chetwynd, E. P. Shettle, A. Berk, L. S. Bernstein, D. C. Robertson, P. Acharya, L. S. Rothman, J. E. A. Selby, W. O. Gallery, and S. A. Clough. The MODTRAN 2/3 Report and LOWTRAN 7 MODEL. Technical report, Phillips Laboratory, Geophysics Directorate, November 1996.

[156] G. A. Rao and S. P. Mahulikar. Effect of atmospheric transmission and radiance on aircraft infrared signatures. *Journal of Aircraft*, 42(4):1046–1054, 2005.

[157] U.S. Standard Atmosphere, 1976. Prepared jointly by the National Oceanic and Atmospheric Administration, National Aeronautics and Space Administration, and the United States Air Force, Washington, D.C., October 1976. NASA-TM-X-74335.

[158] G. W. Petty. *A First Course in Atmospheric Radiation*. Sundog Publishing, Madison, Wisconsin, 2nd edition, 2006.

[159] T. W. Schlatter. Atmospheric composition. In *Encyclopedia of Aerospace Engineering*, volume 6, chapter 273, pages 3329–3339. John Wiley & Sons, 2010.

[160] B. J. McBride and S. Gordon. Computer program for calculation of complex chemical equilibrium compositions and applications – Part II. Users manual and program description. RP-1311, NASA, June 1996.

[161] K. Schäfer, J. Heland, D. H. Lister, C. W. Wilson, R. J. Howes, R. S. Falk, E. Lindermeir, M. Birk, G. Wagner, P. Haschberger, M. Bernard, O. Legras, P. Wiesen, R. Kurtenbach, K. J. Brockmann, V. Kriesche, M. Hilton, G. Bishop, R. Clarke, J. Workman, M. Caola, R. Geatches, R. Burrows, J. D. Black, P. Hervé, and J. Vally. Nonintrusive optical measurements of aircraft engine exhaust emissions and comparison with standard intrusive techniques. *Applied Optics*, 39(3):441–455, 2000.

[162] F. Mei, S. Chen, Y. Jiang, and J. Cai. A preliminary model of infrared image generation for exhaust plume. *International Journal of Image, Graphics and Signal Processing*, 3(4):46–52, 2011.

[163] Ph. Rivière, A. Soufiani, and J. Taine. Correlated-k fictitious gas model for H_2O infrared radiation in the Voigt regime. *Journal of Quantitative Spectroscopy and Radiative Transfer*, 53(3):335–346, 1995.

[164] A. Wang and M. F. Modest. Importance of combined Lorentz-Doppler broadening in high-temperature radiative heat transfer applications. *ASME Journal of Heat Transfer*, 126(5):858–861, 2004.

[165] D. Balsara. Fast and accurate discrete ordinates methods for multidimensional radiative transfer. Part I, basic methods. *Journal of Quantitative Spectroscopy and Radiative Transfer*, 69(6):671–707, 2001.

[166] Y. Shan and J. Zhang. Numerical investigation of flow mixture enhancement and infrared radiation shield by lobed forced mixer. *Applied Thermal Engineering*, 29 (17–18):3687–3695, 2009.

[167] C. Pan, J. Zhang, and Y. Shan. Effects of exhaust temperature on helicopter infrared signature. *Applied Thermal Engineering*, 51(1–2):529–538, 2013.

[168] X. Zhang and R. Li. Numerical study on similarity of plume's infrared radiation from reduced scaling solid rocket. *Journal of Applied Mathematics*, 2015. Article ID 627351, 11 pages.

[169] J. Gonçalves and P. J. Coelho. Parallelization of the discrete ordinates method. *Numerical Heat Transfer, Part B: Fundamentals*, 32(2):151–173, 1997.

[170] D. N. Trivic. 3-D radiation modeling of nongray gases-particles mixture by two different numerical methods. *International Journal of Heat and Mass Transfer*, 70:298–312, March 2014.

[171] M. J. Wright, R. M. Rao, G. V. Candler, J. S. Hong, T. A. Schilling, and D. A. Levin. Modeling issues in the computation of plume radiation signatures. In *Proceedings of the 34th AIAA/ASME/SAE/ASEE Joint Propulsion Conference and Exhibit*, Cleveland, July 1998. AIAA 1998-3622.

[172] F. Liu. Numerical solutions of three-dimensional non-grey gas radiative transfer using the statistical narrow-band model. *ASME Journal of Heat Transfer*, 121(1): 200–203, 1999.

[173] D. N. Trivic. Modeling of 3-D non-gray gases radiation by coupling the finite volume method with weighted sum of gray gases model. *International Journal of Heat and Mass Transfer*, 47(6–7):1367–1382, 2004.

[174] S. H. Kim and K. Y. Huh. Assessment of the finite-volume method and the discrete ordinate method for radiative heat transfer in a three-dimensional rectangular enclosure. *Numerical Heat Transfer, Part B: Fundamentals*, 35(1):85–112, 1999.

[175] P. J. Coelho. Numerical simulation of radiative heat transfer from non-gray gases in three-dimensional enclosures. *Journal of Quantitative Spectroscopy and Radiative Transfer*, 74(3):307–328, 2002.

[176] T. K. Kim, J. A. Menart, and H. S. Lee. Nongray radiative gas analyses using the S-N discrete ordinates method. *ASME Journal of Heat Transfer*, 113(4):946–952, 1991.

[177] L. Zhang, A. Soufiani, and J. Taine. Spectral correlated and non-correlated radiative transfer in a finite axisymmetric system containing an absorbing and emitting real gas-particle mixture. *International Journal of Heat and Mass Transfer*, 31 (11):2261–2272, 1988.

[178] X. He, E. Lee, L. Wilcox, R. Munipalli, and L. Pilon. A high-order-accurate GPU-based radiative transfer equation solver for combustion and propulsion applications. *Numerical Heat Transfer, Part B: Fundamentals*, 63(6):457–484, 2013.

[179] X. Cui and B. Q. Li. A discontinuous finite-element formulation for multidimensional radiative transfer in absorbing, emitting, and scattering media. *Numerical Heat Transfer, Part B: Fundamentals*, 46(5):399–428, 2004.

[180] J. M. Zhao and L. H. Liu. Discontinuous spectral element method for solving radiative heat transfer in multidimensional semitransparent media. *Journal of Quantitative Spectroscopy and Radiative Transfer*, 107(1):1–16, 2007.

Appendix A

IR Radiative Properties of Exhaust Plumes

Provided that the distributions of spectral radiances $I_\eta(\vec{s})$ throughout the entire exhaust plume are known, the IR radiative properties of the plume can readily be calculated by integrating the I_η values using several options. All IR characteristics (signatures) of the plume are directional quantities.

The spectral (radiant) intensity $J_\eta(\vec{s})$ is the IR radiation emitted by the entire plume per unit wavenumber. The spectral intensity plotted versus wavenumber exhibits the emission spectrum of the plume. An integration of I_η over the plume's surface projected into the direction of interest $\vec{s}$ yields this quantity[1]

$$J_\eta(\vec{s}) = \int_A I_\eta(\vec{s})\, \vec{s}\cdot\vec{n}\, dA, \qquad \vec{s}\cdot\vec{n} > 0, \tag{A.1}$$

where A is the plume surface area and $\vec{n}$ is the outward surface normal. In the JERAD code (Appendix D), the integration in Eq. (A.1) is performed over the boundary faces of the computational domain.

The radiant (total) intensity $J(\vec{s})$ represents the total plume IR emission in a particular spectral interval, $\Delta\eta$. Thus, this quantity is obtained by integrating the J_η values, Eq. (A.1), over $\Delta\eta$

$$J(\vec{s}) = \int_{\Delta\eta} J_\eta(\vec{s})\, d\eta, \tag{A.2}$$

where $\Delta\eta = \eta_{max} - \eta_{min}$, with η_{min} and η_{max} being the lower and upper bounds of the spectral interval, respectively.

[1]The plane onto which the plume's surface is projected is sometimes called "object plane" [19, 162]; the object plane for a broadside viewed plume is shown in Fig. 5.1.

In order to obtain the distribution of IR emission along the plume axis, the spectral radiance can be integrated in the dimension transverse to the plume axis (and over a wavenumber range of interest, if required). The resulting quantity is called the station radiance [1] and can therefore be defined as

$$I_{\zeta_1} = \int_{\Delta\eta} \int_{\zeta_2} I_\eta(\zeta_1, \zeta_2)\, d\zeta_2\, d\eta, \tag{A.3}$$

where ζ_1 and ζ_2 are the axial and transverse coordinates associated with the object plane (as shown in Fig. 5.1). The station radiance I_{ζ_1}, which is expressed in $\mathrm{W\,m^{-1}\,sr^{-1}}$, is useful for comparisons with data collected by a sensor capable of resolving the plume axially but not transversely [1].

Integration of I_η over $\Delta\eta$ provides the radiance distribution in a particular bandpass, for example, that is defined by the spectral filter in an IR camera [1],

$$I_{\zeta_1,\zeta_2} = \int_{\Delta\eta} I_\eta(\zeta_1, \zeta_2)\, d\eta. \tag{A.4}$$

Radiance maps can be useful for the identification of the plume structure [30, 31]. They can also be useful for comparisons of calculated and measured radiation data [34, 171].

Figs. 5.5 to 5.8 are examples of plume IR characteristics resolved in one and two dimensions. Fig. 5.5 shows 1D distributions of station radiances. Figs. 5.6 to 5.8 show the corresponding 2D radiance contours (synthetic IR images of plume).

Appendix B

Simulation of Radiative Heat Transfer in Three-Dimensional Rectangular Enclosures

B.1 General Considerations

In this appendix, computational results for the total radiative heat flux and for the divergence of the total radiative heat flux (or radiative heat source, see Appendix C) are presented and compared with those reported in the literature to demonstrate the validity of the FVM based RTE solver implemented in the present work. Nongray gas radiation analysis by coupling the FVM with the CK method, which is used here for modeling of the gas IR radiative properties, has not been previously conducted to the author's best knowledge.

Four test problems for the radiative transfer in gas mixtures suggested by Liu [172] and by Trivic [173] are considered. The fifth problem proposed by Trivic in the work [170] deals with a gas mixture containing nonscattering soot particles.

A 3D rectangular enclosure of $2\,\mathrm{m} \times 2\,\mathrm{m} \times 4\,\mathrm{m}$ in the x, y and z coordinate directions, respectively, is employed in all test cases. The enclosure's six walls are black and hold at 300 K. The total pressure of the gas mixture in the enclosure is 1 atm. In order to obtain the total radiative heat flux and its divergence, the spectral integration is carried out over a range of $200 - 9300\ \mathrm{cm}^{-1}$ that is composed by 221 narrow bands of the SRCS k-distribution database. To satisfy the half-range first moment when calculating heat fluxes incident on the walls, an angular discretization of $2n_\theta \times 4n_\varphi$ is used, where n_θ and n_φ are positive integers [174]. The 8-point quadrature scheme (see Table 3.2) is employed in the CK method, and the narrow-band mixing model of Modest and Riazzi [107] is used to treat (where appropriate) overlapping bands.

B.2 Test Case 1: Homogeneous, Isothermal Medium

A homogeneous and isothermal medium is assumed first, i.e. the gas is pure H_2O at a uniform temperature of 1000 K. Accurate numerical solutions for this and two other problems, which are described below in Sections B.3 and B.4, were provided by Liu [172] who employed a RT solver coupled with the Malkmus SNB model. Coelho [175] used these data as a benchmark to compare numerical results by DOM and DTM combined with a variety of spectral models when simulating the same test cases.

RTE solutions given by the RT method are exact since they do not contain the error due to spatial discretization. Moreover, the SNB parameters used in the work [172] are from the EM2C data set [83]. These parameters are based on the adjustment of the curves of growth and the error inherent to the SNB model assumptions is thus reduced. Since the medium is homogeneous and isothermal, the CGA was not applied to this particular problem. For other problems, where the medium is inhomogeneous and/or nonisothermal, the CGA is similar to the correlated assumption of the CK method. Consequently, the solutions obtained in [172] will also be used as benchmark ones in the present work.

A uniform spatial grid of $11 \times 11 \times 16$ was adopted for the simulations by the FVM. The grid is identical to that used in [172] and [175]. In order to show the effect of angular discretization, the solid angle grids of 2×4, 10×8, and 10×12 were used yielding, respectively, 8, 80, and 120 discretized directions that cover the total range of solid angles 4π. Note that the T_4 quadrature set [64] (128 directions) was applied to the calculations performed in [172, 175].

Fig. B.1 shows the heat flux incident on the enclosure's walls along (x, 1 m, 4 m) and (2 m, 1 m, z), and the divergence of the heat flux along (x, 1 m, 0.375 m) and along the centerline (1 m, 1 m, z). The benchmark data by Liu [172] and the results by Coelho [175] obtained with the DOM combined with the CK, SLW and WSGG models are also shown for comparisons. Due to the symmetry of this problem, the flux and divergence distributions along the z direction are presented for half of the enclosure.

The 2×4 discretization is equivalent to the DOM S_2-approximation that is known to be inaccurate [63]. When compared with the RT benchmark solutions, this discretization results in maximum percentage errors[1] of 8.3% and 17% for the flux along (x, 1 m, 4 m), Fig. B.1(a), and for the divergence along (x, 1 m, 0.375 m), Fig. B.1(b), respectively. The use of the 10×8 discretization decreases the flux maximum error along (x, 1 m, 4 m) up to 4.5% whereas the divergence maximum error along (x, 1 m, 0.375 m) is increased up to 22%. The mean absolute percentage error for the flux is decreased from 6.6% to 4% whereas that for the divergence is increased from 13% to 20%. Further angular grid refinements have a negligible influence on the simulation

[1] Errors are taken with the absolute value.

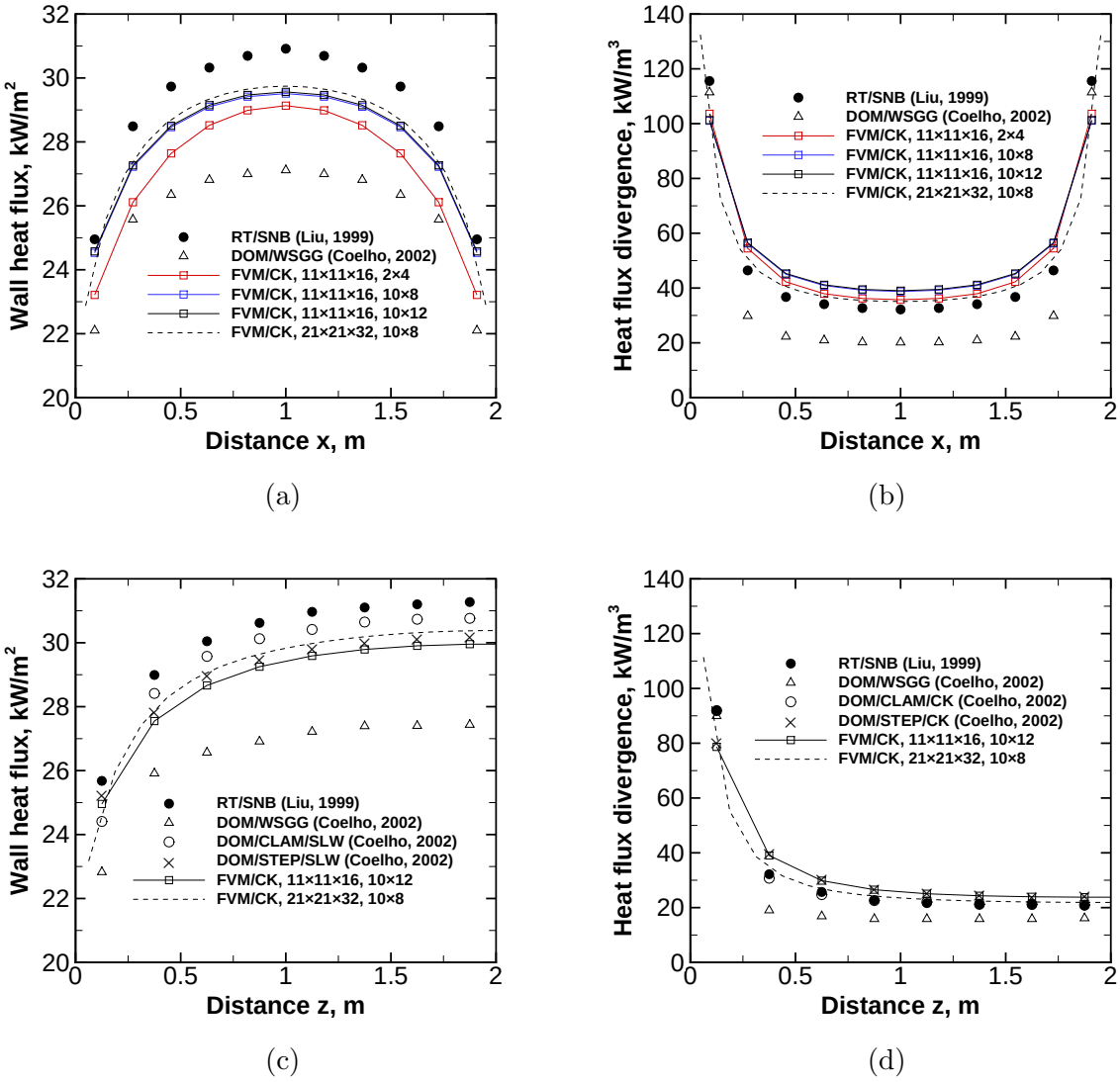

Figure B.1: Incident heat flux and divergence of radiative heat flux calculated by the FVM in comparison with the RT benchmark solutions [172] and DOM results [175] for test case 1: (a) wall heat flux along (x, 1 m, 4 m), (b) divergence of heat flux along (x, 1 m, 0.375 m), (c) wall heat flux along (2 m, 1 m, z), (d) divergence of heat flux along the centerline (1 m, 1 m, z)

results while significantly increasing CPU time, e.g., from 1043 s for the 10×8 FVM to 1983 s for the 10×12 FVM.[2]

The increase in solution error for the divergence of the heat flux along (x, 1 m, 0.375 m) with angular grid refinements is likely associated with the complex interaction between the spatial and directional discretization errors. According to the work [78], the spatial error (false scattering) effectively smears the radiation within each control solid angle,

[2]All computations except for test case 5 (see Section B.6 below) were run on one core of an Intel Xeon X7542 processor at 2.67 GHz. For test case 5, a parallel algorithm was employed to facilitate the computations. The algorithm is based on solid angle partition [169].

whereas the direction error (ray effect) effectively concentrates the radiation along the center of each control angle. This yields that the spatial and directional discretization errors tend to cancel.

It is often required to refine spatial and angular grids simultaneously in order to improve prediction accuracy. Not to do so can adversely affect error cancellation. This explains why the 10×8 FVM applying a finer spatial grid of $21 \times 21 \times 32$ yields better results than the FVM applying the coarse spatial grid even though the angular grid is much finer, as demonstrated in Fig. B.1. Note that this comparison is valid because the benchmark data in [172] are shown to be grid independent.

The solutions gained by DOM [175] are in better agreement with the RT benchmark solutions than the results of FVM, except for the DOM with the WSGG model. In particular, the average relative errors of 0.6% for the incident heat flux along (2 m, 1 m, z) and of 1.1% for the flux divergence along the centerline (1 m, 1 m, z) have been reported in [175] for the CK model. The flux and divergence distributions along these lines are shown in Figs. B.1(c) and (d), respectively, and the corresponding errors for the 10×12 FVM are 4.3% and 20%.

The DOM and FVM are very similar in orthogonal grids. Besides, the directional discretizations utilized by both methods are nearly equivalent with respect to the number of control angles, i.e. the ray effect is believed to be equally pronounced. However, in the work [175], the second-order CLAM scheme [69, 71] was used. In the current work, the step (upwind) scheme, which is only first-order accurate, is applied to all calculations. This means that the difference between the results of DOM and FVM is mostly attributed to the spatial differencing scheme.

The effect of discretization scheme is clearly seen in Figs. B.1(c) and (d) where the DOM predictions [175] using the step scheme are shown as well. The results for the wall heat flux along (2 m, 1 m, z), Fig. B.1(c), are based on the SLW model whereas those for the divergence of the heat flux along the centerline are based on the CK method (Fig. B.1(d)). When the step scheme is used, the DOM average relative error in Fig. B.1(c) increases from 2.2% to 3.4%, whilst the error in Fig. B.1(d) increases from 1.1% to 19% [175]. Therefore, the DOM and FVM predictions match each other very well despite the fact that different gas radiative property models were employed.

B.3 Test Case 2: Inhomogeneous Medium

In the second test case, the medium is isothermal at 1000 K, but the gas is now an inhomogeneous mixture of H_2O and N_2. The H_2O mole fraction varies according to

$$x_{H_2O} = 4\frac{z}{L_z}\left(1 - \frac{z}{L_z}\right), \tag{B.1}$$

where $L_z = 4$ m.

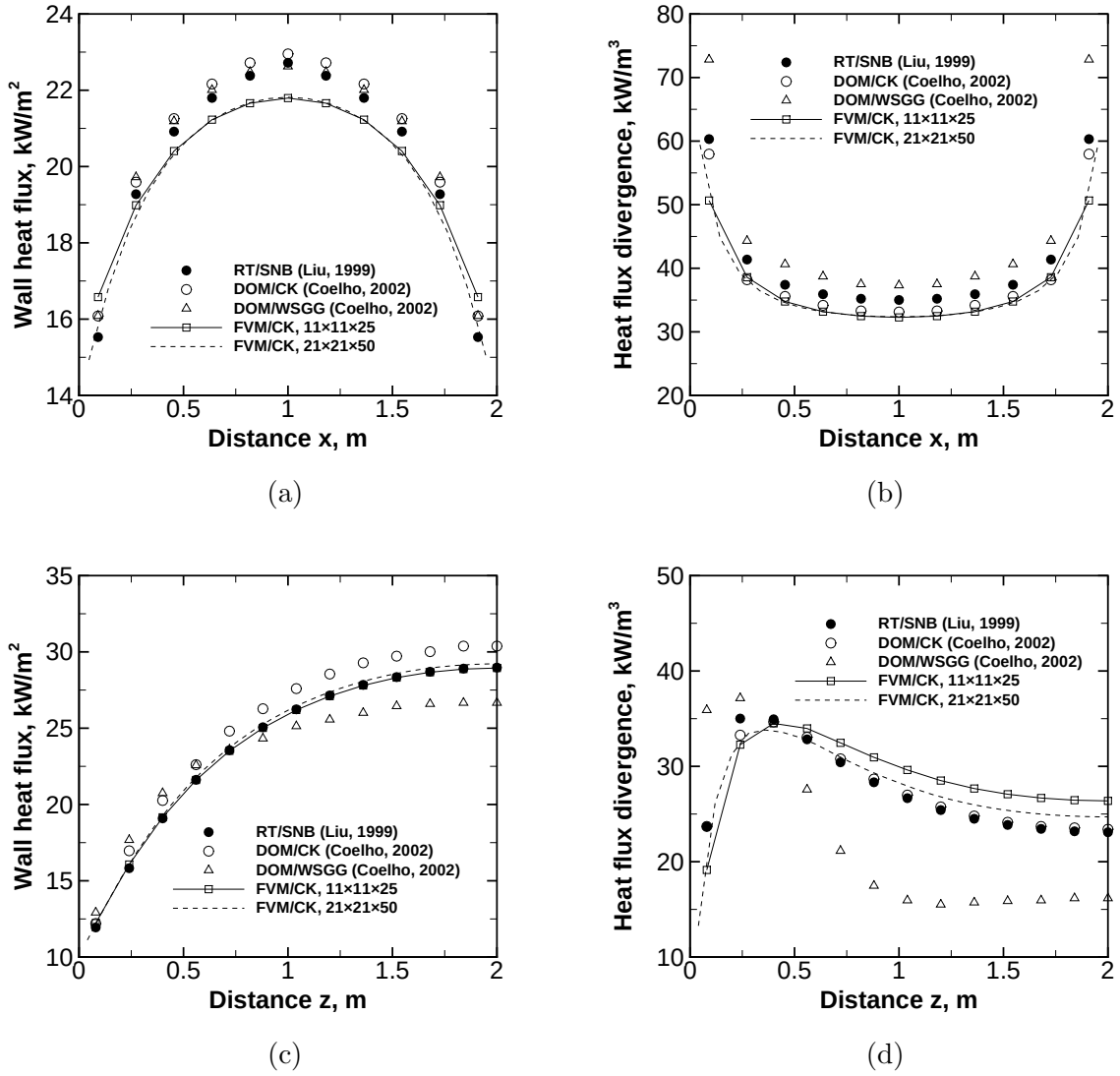

Figure B.2: Incident heat flux and divergence of radiative heat flux calculated by the 10×12 FVM in comparison with the RT benchmark solutions [172] and DOM results [175] for test case 2: (a) wall heat flux along (x, 1 m, 4 m), (b) divergence of heat flux along (x, 1 m, 0.24 m), (c) wall heat flux along (2 m, 1 m, z), (d) divergence of heat flux along the centerline (1 m, 1 m, z)

A $11 \times 11 \times 25$ uniform grid was used to perform FVM simulations. This is the same grid used to obtain both the benchmark and DOM solutions [172, 175]. Additionally, a finer grid of $21 \times 21 \times 50$ was used to demonstrate the effect of grid refinement for this particular case. The solid angle grid of 10×12 rather than that of 10×8 was adopted. The 10×12 discretization yields 120 directions so that it closer matches the T_4 quadrature used in [172, 175].

The FVM predictions alongside with those of RT [172] and DOM [175] are presented in Fig. B.2. As for test case 1, the quantities along the z direction are shown for half of the enclosure.

In comparison with the benchmark solutions, the mean absolute error for the wall fluxes in Figs. B.2(a) and (c) does not exceed 3%. If the DOM is used in conjunction with the CK model, the maximum value of the average error is 4.9% [175]. That is, the FVM and DOM are of equal accuracy when applied to the flux calculations even through the CK method implemented in the work [175] differs from that of the present work with respect to the quadrature scheme and CK parameters used (see [83] for detail).

The flux divergence errors associated with the FVM predictions are however higher than those associated with the CK based DOM predictions. Indeed, the FVM maximum mean error for the divergence values in Figs. B.2(b) and (d) is 10% whereas that for the DOM is only 5.3% [175]. This difference is attributed to using the first-order step scheme that has already been mentioned in Section B.2. As can be seen in Fig. B.2(d), the grid refinement reduces the spatial discretization error associated with the step scheme and significantly improves the accuracy of the flux divergence prediction along the centerline of the enclosure.

The WSGG model data obtained in the work [175] are also shown in Fig. B.2 for comparisons. The model was employed in [175] with the coefficients determined by Smith et al. [88], with the nongray implementation, and with three gray gases. The WSGG model gives high errors, namely up to 30% on average and 50% at maximum [175]. The so-called W-shaped source term profile (keeping in mind that the radiative heat source $S_r = -\nabla \vec{q}_r$), which also occurs in 1D problems [176], is predicted qualitatively wrong by the WSGG model, whereas the CK method predictions are in good agreement with the benchmark as demonstrated in Fig. B.2(d).

B.4 Test Case 3: Nonisothermal Medium

This test case can be thought of as modeling a furnace with one burner placed at the center of the wall at $z = 0$ m [175]. The medium is a uniform mixture of 10% CO_2, 20% H_2O and 70% N_2 on mole basis. The gas mixture temperature is essentially nonuniform but symmetric about the centerline and is prescribed as

$$T = (T_c - T_e)\, f\left(\frac{r}{R}\right) + T_e, \tag{B.2}$$

where T_e is the exit temperature at $z = 4$ m and T_c is the temperature along the centerline of the enclosure. The centerline temperature increases linearly from the inlet temperature of 400 K at $z = 0$ m to the maximum temperature of 1800 K at $z = 0.375$ m, and then decreases linearly to $T_e = 800$ K. In Eq. (B.2), r is the distance from the centerline, $R = 1$ m, and $f(r/R) = 1 - 3(r/R)^2 + 2(r/R)^3$ if $r/R \leqslant 1$, and $f(r/R) = 0$ otherwise. The temperature distribution is shown in Fig. B.3.

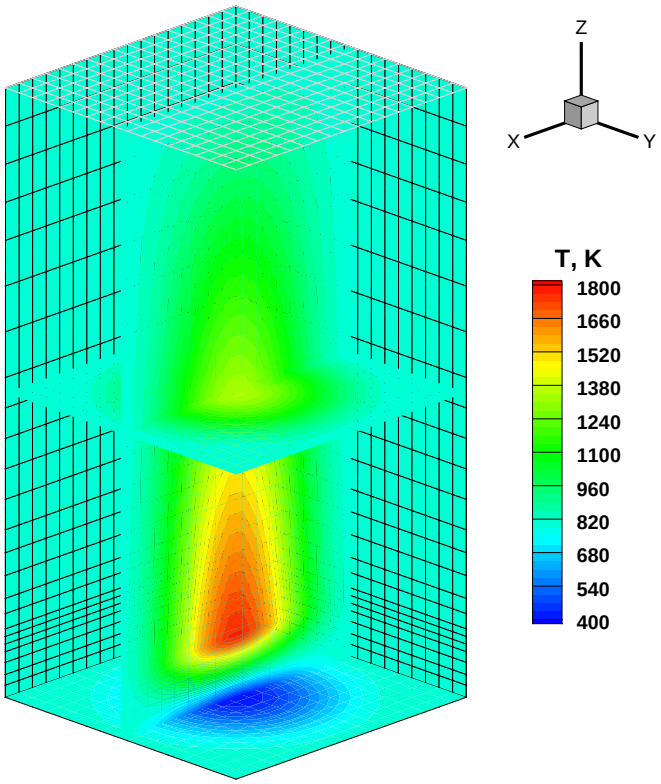

Figure B.3: Gas temperature and the nonuniform surface grid of $17 \times 17 \times 24$ for test case 3

Basic calculations for this test case were carried out using a spatial grid of $17 \times 17 \times 24$ which is nonuniform in the z direction (see Fig. B.3). The directional discretization is 10×12. Alongside with the use of the CK method, two gray-band models, namely the CKG and SNBG models, were applied to this test problem. The FVM results are displayed in Fig. B.4 where they are compared with those of RT [172] and DOM coupled with the SLW model [175]. The DOM computational data obtained using the SNBCK method are shown as well. These data are taken from the work [82] for the SNBCK method implemented with the 1-point and 7-point Gauss quadratures which are referred to as SNBCK1 and SNBCK7, respectively.

As can be seen in Fig. B.4(a), the CK method predictions for the radiative heat flux incident on the wall along (2 m, 1 m, z) show very good agreement with those given by the benchmark and DOM. When compared with the benchmark, the maximum error of 6.4% occurs at $z = 0.725$ m.

The radiative fluxes calculated using the gray-band approximations are overestimated by up to 37% for the CKG model and 42% for the SNBG model. Both the gray-band models ignore the fine structure of rotational lines by replacing the rapidly oscillating absorption coefficient with an average value over each narrow band. This approximation corresponds either to an optically thin medium or to a strong overlapping of the lines at high pressures. Neither of the conditions is true for the given problem so that using the average absorption coefficient makes the gas opaque within the entire narrow band.

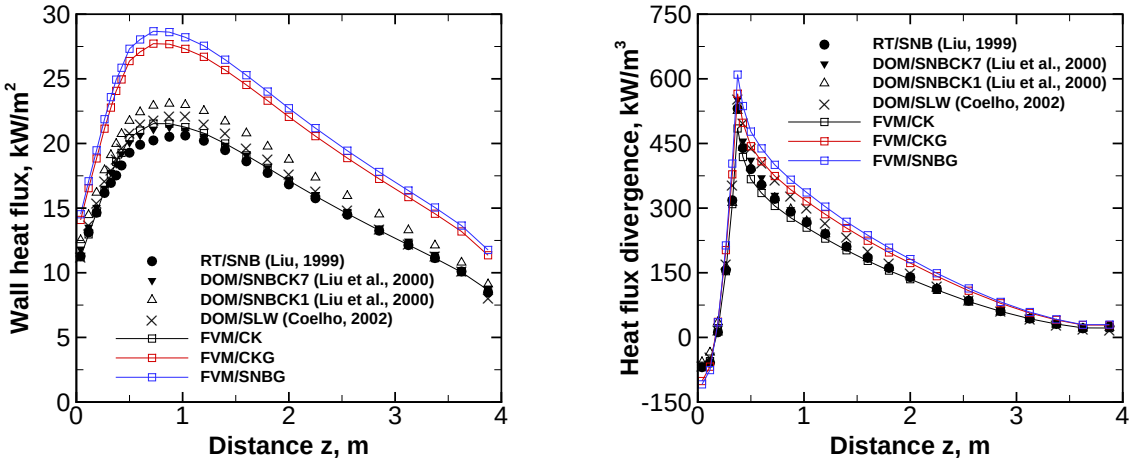

(a) (b)

Figure B.4: Incident heat flux and divergence of radiative heat flux calculated by the 10×12 FVM using the $17 \times 17 \times 24$ grid in comparison with the RT benchmark solutions [172] and DOM results [82, 175] for test case 3: (a) wall heat flux along (2 m, 1 m, z), (b) divergence of heat flux along the centerline of the enclosure (1 m, 1 m, z)

This leads to the wall fluxes to be overpredicted as both gas absorption and emission are enhanced. In other words, the use of the gray-band approximations results in the spectrally uncorrelated formulation of the RTE that gives significant errors [98, 137, 177]. The SNBCK1 method, which performs as a gray-band model, also overestimated the wall fluxes albeit by only 9% around the peak value [82].

It is worth mentioning that the mean absorption coefficient values used together with the SNBCK model were taken from the earlier EM2C data set on SNB model parameters [83] rather than from the updated one [116]. The computation results based on the updated data were found to be nearly indistinguishable from those based on the earlier data and thus they are not shown in Fig. B.4.

Fig. B.4(b) shows the radiative flux divergence profiles as predicted by the FVM coupled with the three narrow-band models. Regardless of the model used, the divergence distribution along the centerline exhibits a qualitatively correct shape which is expected from the temperature field. The minimum value of the divergence occurs at the inlet of the enclosure where the temperature reaches its minimum indicating the dominant influence of gas absorption. The maximum value of the divergence occurs where the temperature reaches its maximum at $z = 0.375$ m so that gas emission prevails. Note that the heat flux incident on the wall along (2 m, 1 m, z), Fig. B.4(a), reaches its peak value further downstream at nearly $z = 0.725$ m, indicating that the thermal radiation is a long-range phenomenon [172].

The radiative divergence profile predicted by the CK agrees well with that of the benchmark except for the peak value at $z = 0.375$ m where the divergence is underpredicted

by 8.7%. This is believed to be a consequence of using the first-order step scheme. The errors given by the gray-band models are however significantly larger than those of the CK model. The divergence value is underpredicted by up to 58% near the inlet of the enclosure and overpredicted by up to 40% further downstream. Therefore, the use of the gray-band approximations overestimates both gas absorption and emission, as expected.

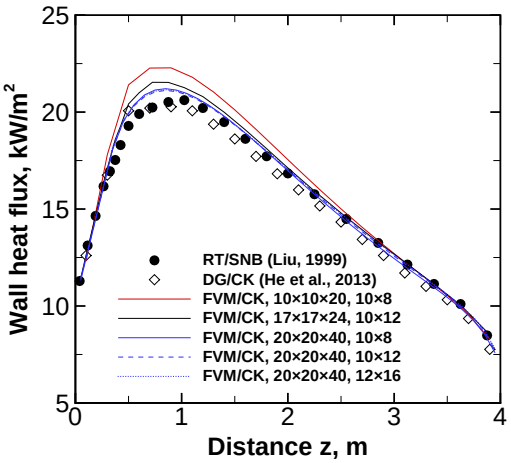

Figure B.5: Comparison of the predicted radiative heat flux incident on the wall along (2 m, 1 m, z) with the RT benchmark solutions [172] and DG method results [178] for test case 3

Fig. B.5 shows the FVM results for the wall flux along (2 m, 1 m, z) as compared with the data due to He et al. [178]. In the work [178], the discontinuous Galerkin (DG) method (see, e.g., [179, 180]) was applied to the given test case. The DG method results corresponding to the P-5 DG order and S_8 (80 directions) angular quadrature set are shown in the figure. Note that the simulations performed in [178] are narrow-band based with the CK model parameters tabulated by Soufiani and Taine [83].

A uniform spatial grid of $10 \times 10 \times 20$ was however adopted in [178]. Therefore, the basic FVM simulation was performed using the same $10 \times 10 \times 20$ grid and the 10×8 solid angle discretization. Also shown in Fig. B.5 are the predictions by the 10×12 FVM using the $17 \times 17 \times 24$ grid (as in Fig. B.4) as well as the results obtained using a finer uniform grid of $20 \times 20 \times 40$ with angular discretizations of 10×8, 10×12, and 12×16.

In general, the DG solution closely matches the SNB based benchmark, whereas the FVM resulted in an overprediction of the wall heat flux. The difference between the computational results of these two methods is about 6% on average. It is readily seen that refinements of both the spatial and angular grids are needed to improve the FVM accuracy.

B.5 Test Case 4: Nonisothermal Medium

This test case was proposed by Trivic [173]. The temperature distribution within the enclosure is given by Eq. (B.2) as for test case 3, but the water mole fraction is reduced by a factor of 2 so that the gas mixture is now 10% CO_2, 10% H_2O and 80% N_2.

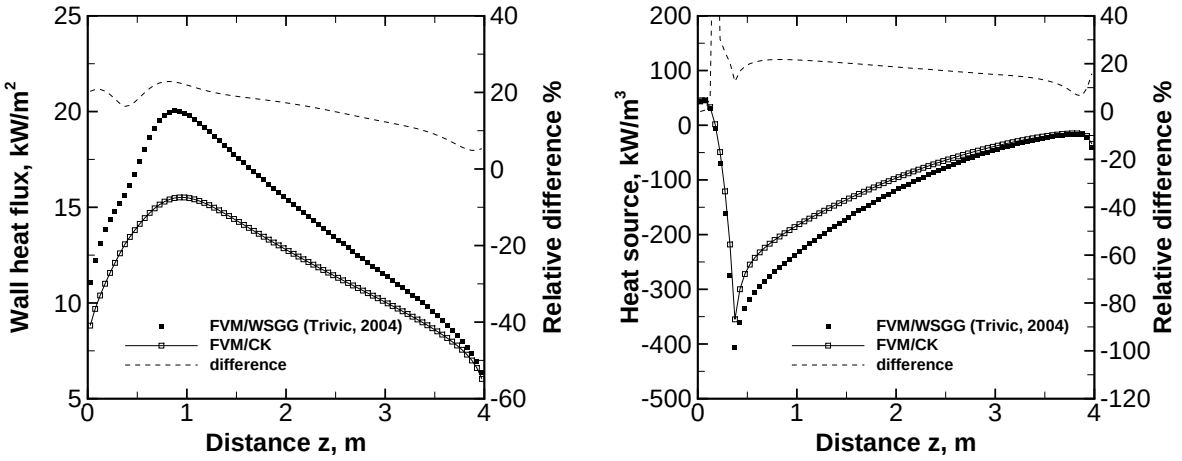

(a) (b)

Figure B.6: Predicted incident heat flux and radiative heat source for test case 4 in comparison with the WSGG based FVM solutions reported in [173]: (a) wall heat flux along (2 m, 1 m, z), (b) radiative heat source along the centerline of the enclosure (1 m, 1 m, z)

A benchmark solution of this test problem is not available. In the work by Trivic [173], however, numerical simulations for the radiative heat flux incident on the wall along (2 m, 1 m, z) and for the radiative heat source along the centerline of the enclosure (1 m, 1 m, z) have been performed using the FVM. Trivic used a uniform angular discretization and the step scheme. This implies that a direct comparison between data reported in [173] and results obtained in the present work can be done. Any discrepancies in the predictions will be attributed solely to the difference between the global WSGG model adopted in [173] and the narrow-band CK method implemented here.

The CK based computational results obtained using a uniform grid of $41 \times 41 \times 80$ and the 4×20 angular discretization are demonstrated in Fig. B.6. The finite volume and solid angle discretizations are identical to those employed by Trivic for the WSGG based FVM computations [173]. Trivic's results are shown in Fig. B.6 as well. Also shown in the figure is the relative percent difference between the data defined as

$$\text{Relative difference } \% = 100 \times \frac{|q_{\text{WSGG}} - q_{\text{CK}}|}{\max\big(|q_{\text{WSGG}}|, |q_{\text{CK}}|\big)}, \tag{B.3}$$

where $q \equiv q^{in}_{r,w}$ and $q \equiv S_r$ for the wall flux and the heat source, respectively.

When compared to the WSGG solution [173], the radiative heat flux indecent on the wall along (2 m, 1 m, z) seems to be underpredicted by using the CK model, Fig. B.6(a). Likewise, the radiative source along the enclosure's centerline (1 m, 1 m, z) is underestimated, Fig. B.6(b). The local difference for the heat source reaches a maximum of 128% at around $z = 0.175$ m. Since the source values are close to zero at that location, the absolute difference is insignificant. With the exception of previously mentioned maximum, the relative difference between the predictions is less than approximately 20% for both the wall flux and the heat source.

The WSGG model due to Smith et al. [88] implemented with 4 gray gases (plus one clear gas) was used in the paper [173]. Except for the number of gray gases, the implementation is similar to that adopted by Coelho in the work [175]. As demonstrated in Figs. B.1 and B.2, the WSGG model resulted in significant errors when incorporated into DOM computations performed in [175].

The WSGG model parameters, i.e. the gray gas absorption coefficients and weights, are generally found from adjustments of total emissivity data [94, 98]. For instance, Smith et al.'s parameters [88] were derived to give the best fit to the emissivities obtained using the exponential wide-band model of Edwards [87]. The parameters are simply numbers without clear physical interpretation. Therefore, the application of the WSGG model to nonuniform media is mostly empirical and it can lead to very important errors [94]. It follows that the difference between the predictions mentioned above is most likely due to inaccuracy of the WSGG model.

The CK method and other global models, such as the SLW and FSK models, use the absorption coefficient as the basic radiative property. In particular, the absorption coefficient values for the CK method were obtained from the CDSD-1000 and HITEMP spectroscopic databases for CO_2 and H_2O, respectively. This ensures accurate numerical solutions of radiative heat transfer in nonisothermal and nonhomogenous media.

B.6 Test Case 5: Gas-Soot Mixture

The last test case was borrowed from the recent work of Trivic [170], where numerous simulations of radiative heat transfer in gas mixtures containing various gray anisotropically scattering particles had been carried out.

In the test case, the temperature distribution and the gas mixture composition are identical to those of case 3 described in Section B.4. Now the medium contains soot uniformly distributed with $f_v = 2.001 \times 10^{-6}$. Soot particles are at the same temperature as gas. The particles are considered to be nongray with the absorption coefficients evaluated invoking the assumption of small particles [23] (scattering is therefore neglected). The soot's complex index of refraction was determined using the polynomial expressions given by Chang and Charalampopoulos [141].

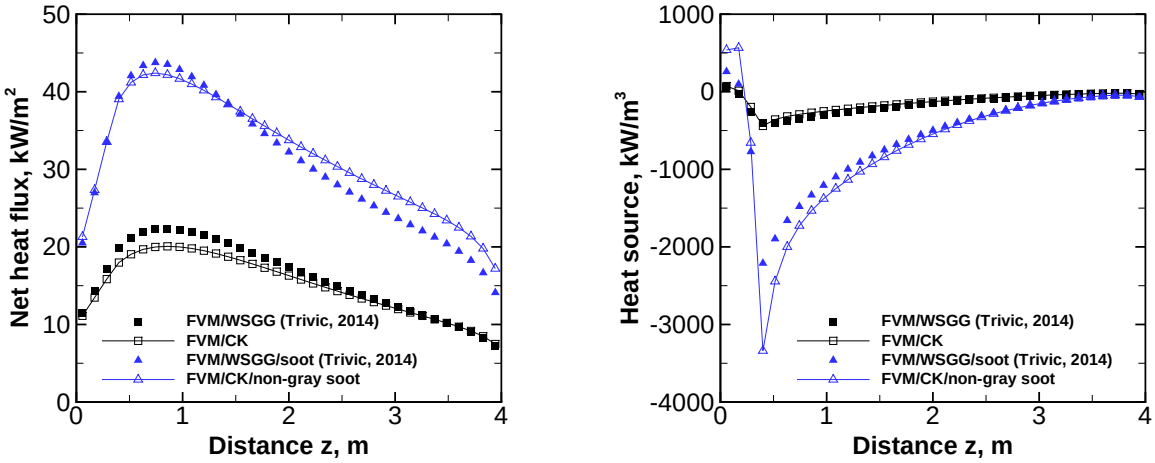

(a) (b)

Figure B.7: Predicted net heat flux and radiative heat source for test case 5 in comparison with the FVM solutions for gas and gas-soot mixtures reported in [170]: (a) net heat flux at the side wall at $y = 0$ along (1 m, 0 m, z), (b) radiative heat source along the centerline of the enclosure (1 m, 1 m, z)

The predicted radiative heat flux at one side wall along (1 m, 0 m, z) and radiative heat source along the centerline of the enclosure (1 m, 1 m, z) are depicted in Fig. B.7. Note that the net heat flux rather than the incident heat flux is shown. The computational results are compared to the FVM data kindly provided by Trivic.[3] In order to show the effects of soot on both the radiative flux and radiative source, the predictions for pure gas medium are also demonstrated in the figure. All results presented were obtained by uniformly subdividing the enclosure into $35 \times 35 \times 35$ control volumes. An angular discretization of 12×20 was used.

The maximum values of relative percent difference, Eq. (B.3), between Trivic's results and those obtained in the present work for the gas-soot mixture are 18% and 83% for the net heat flux and for the heat source, respectively. The latter occurs near the inlet, whereas the difference at the peak gas temperature ($z = 0.375$ m, see Eq. (B.2)) is 34%.

Taking into account that discretization errors encountered in both simulations are of the same magnitude, the differences reported above are attributed to how the gas-soot mixture radiative properties were modeled. The results obtained in the present study are believed to be more accurate. Indeed, the CK method has been shown in Section B.5 to be superior to the WSGG model used in [170]. It is obvious that considering soot as nongray further improves the simulation accuracy. It should also be noted that although Mie scattering theory applied in Trivic's work is the most general method, it is not the

[3]D. N. Trivic. Personal communication, November 4, 2014.

best approach for all material types and particle parameters [170]. Soot particles, in particular, obey the Rayleigh limit leading to negligible scattering [23].

With the given soot volume fraction, soot radiation is a significant contributor to the overall medium emission along with gas radiation (or even prevails over it). It is readily seen from Fig. B.7 that the net wall heat flux is enhanced by a factor of approximately 2 when compared to the pure gas case. Similarly, the heat source absolute values along the enclosure's centerline are significantly higher than those for the soot-free medium, especially around the peak gas temperature.

The FVM implemented in the current work has been validated against computational data available in the literature. The validity of the method was demonstrated by performing numerical simulations of radiative heat transfer in a 3D rectangular enclosure with specified temperature and species concentration fields. Five test cases involving homogeneous and inhomogeneous, isothermal and/or nonisothermal participating media containing CO_2 and H_2O as well as a gas mixture loaded with soot particles were considered. In all test cases, the radiative heat flux incident on the enclosure walls and the radiative heat source within the medium were predicted using various spatial and angular discretizations. Comprehensive analysis of the simulation results has been carried out. It was shown that by comparing the results with the RT method SNB based benchmark solutions, the FVM coupled with the CK method performs fairly accurately. The mean errors were found to be less than 5% for the radiative heat flux and 10 to 20% for the radiative heat source. Higher errors for the radiative source are likely to be associated with the use of the first-order step scheme. The use of the gray narrow-band models such as CKG and SNBG resulted in significant overestimations of the wall radiative fluxes and in inaccurate predictions of the radiative sources. Since these models provide reasonable computational time when compared to the CK method, they are recommended for use if the error up to 50% is acceptable. The FVM based solutions compared favourably with those given by other methods such as DOM used together with the global SLW model. For the gas-soot mixture case, the benefit of using nongray absorbing soot particles has been demonstrated.

Appendix C

Total Radiative Quantities

Relevant total radiative quantities were calculated and discussed in Appendix B. The derivations of these quantities are given in this appendix with a focus on the use of the FVM in conjunction with the CK model.

The total radiative heat flux vector is obtained from the solution of the intensity field, I_η, by [23]

$$\vec{q_r} = \int_0^\infty \int_{4\pi} I_\eta(\vec{s})\, \vec{s}\, d\Omega\, d\eta, \tag{C.1}$$

where the integrations are performed over the total solid angle of 4π and over the spectrum. Based on Eq. (C.1), for 3D geometries in Cartesian coordinates, the radiative fluxes $q_{r,x}$, $q_{r,y}$ and $q_{r,z}$ in the x, y and z directions can easily be calculated by multiplying $\vec{q_r}$ with $\vec{e_x}$, $\vec{e_y}$ and $\vec{e_z}$.

The net heat flux at a wall surface can be expressed as

$$q_{r,w}^{net} = \vec{q_r} \cdot \vec{n} = \int_0^\infty \int_{4\pi} I_\eta(\vec{s})\, \vec{s} \cdot \vec{n}\, d\Omega\, d\eta, \tag{C.2}$$

where $\vec{n}$ is the surface normal pointing into the medium.

In order to get the heat flux incident on a wall, the angular integration in Eq. (C.2) should be carried out over the hemisphere above the wall surface, i.e.

$$q_{r,w}^{in} = \int_0^\infty \int_{\vec{s}\cdot\vec{n}<0} I_\eta(\vec{s}) |\vec{s} \cdot \vec{n}|\, d\Omega\, d\eta. \tag{C.3}$$

The incident radiation, G, can be expressed in terms of the spectral radiation energy density, u_η, as

$$G = c \int_0^\infty u_\eta \, d\eta = \int_0^\infty \int_{4\pi} I_\eta(\vec{s}) \, d\Omega \, d\eta, \tag{C.4}$$

where c is the speed of light.

The divergence of the total heat flux assumes the form

$$\nabla \vec{q}_r = \int_0^\infty \kappa_\eta \left(4\pi I_{b\eta} - G_\eta\right) d\eta, \tag{C.5}$$

where κ_η and $I_{b\eta}$ are, respectively, the spectral absorption coefficient (dimensions 1/m) and blackbody intensity.

The radiative heat source is

$$S_r = -\nabla \vec{q}_r. \tag{C.6}$$

This quantity provides the link with the energy equation in CFD problems involving combined-mode heat transfer (combined diffusion, convection and radiation).

If the FVM implemented with uniform angular discretization is used to solve the RTE and the CK method is used to model gas radiative properties, then the quantities given by Eqs. (C.1)–(C.5) are approximated as follows:

$$\vec{q}_r = \sum_{i=1}^{N_{nb}} \Delta\eta_i \quad \sum_{j=1}^{N} \omega_j \sum_{l \in [1,\, N_\theta \times N_\varphi]} I_{i,j}^l \int_{\Delta\Omega^l} \vec{s} \, d\Omega, \tag{C.7}$$

$$q_{r,w}^{net} = \sum_{i=1}^{N_{nb}} \Delta\eta_i \quad \sum_{j=1}^{N} \omega_j \sum_{l \in [1,\, N_\theta \times N_\varphi]} I_{i,j}^l \int_{\Delta\Omega^l} \vec{s} \cdot \vec{n} \, d\Omega, \tag{C.8}$$

$$q_{r,w}^{in} = \sum_{i=1}^{N_{nb}} \Delta\eta_i \quad \sum_{j=1}^{N} \omega_j \sum_{l',\, \vec{s}\cdot\vec{n}<0} I_{i,j}^{l'} \int_{\Delta\Omega^{l'}} |\vec{s} \cdot \vec{n}| \, d\Omega, \tag{C.9}$$

$$G = \sum_{i=1}^{N_{nb}} \Delta\eta_i \quad \sum_{j=1}^{N} \omega_j \sum_{l \in [1,\, N_\theta \times N_\varphi]} I_{i,j}^l \, \Delta\Omega^l, \tag{C.10}$$

$$\nabla \vec{q}_r = \sum_{i=1}^{N_{nb}} \Delta\eta_i \quad \sum_{j=1}^{N} \omega_j (k_{i,j} + \bar{\kappa}_{p,\Delta\eta_i})(4\pi \bar{I}_{b,\Delta\eta_i} - G_{i,j}). \tag{C.11}$$

In the above equations, N_{nb} is the number of narrow bands, each of width $\Delta\eta_i$, N is the number of quadrature points with respective weight ω_j (as an example, the calculations of Appendix B were carried out with $N_{nb} = 221$ and $N = 8$), and N_θ and N_φ are, respectively, the number of solid angle elements in θ and φ directions. The index l runs over all 4π directions associated with the angular discretization, whereas the index l' in Eq. (C.9) runs over all 2π incoming directions. The integral in Eq. (C.7) represents a vector that points into an average direction within control solid angle $\Delta\Omega^l$ and can be evaluated analytically. In Eq. (C.11), which is formulated for a gas-particle mixture to preserve generality, $\bar{\kappa}_{p,\Delta\eta_i}$ and $\bar{I}_{b,\Delta\eta_i}$ are the particle absorption coefficient and blackbody intensity averaged over $\Delta\eta_i$, $k_j \equiv k_{mix}(g_j)$, and $\sum_{j=1}^{N} \omega_j = 1$.

Computational procedure based on Eqs. (C.7)–(C.11) has been implemented in the radiation package JERAD (Appendix D). The radiative flux $\vec{q}_r = (\, q_{r,x},\, q_{r,y},\, q_{r,z}\,)$, its divergence $\nabla \vec{q}_r$ and incident radiation G are calculated locally at the cell center locations. The wall heat fluxes $q_{r,w}^{net}$ and $q_{r,w}^{in}$ are evaluated at the midpoints of the boundary cell faces.

Appendix D

JERAD Software Overview

Name:	JERAD (JEt RADiation)
Version:	3.03 (June 2015)
Developer:	Alexander Sventitskiy
Objective:	3D radiative heat transfer modeling in emitting, absorbing and scattering media at high temperature
Operating system:	Linux
Programming languages:	C, Fortran
Run modes:	Serial, parallel
Parallelization:	OpenMP API
User's input:	– Input file for the calculation and solver settings – Input file for the computational grid with pressure and temperature distributions[a] – Input file for species distributions – Input file for atmospheric conditions[b]
Output data:[1]	– Total radiative heat flux vector – Radiative heat flux incident on domain boundaries – Divergence of the radiative heat flux – Incident radiation – Radiant (total) intensity – Spectral radiant intensity – Spectral radiance
Spatial grid:	Structured (hexa), non-orthogonal, non-uniform
Angular grid:	Uniform of $N_\theta \times N_\varphi$

[a] Arbitrary CFD solver output.
[b] Optional input for IR signature predictions.

[1] Tecplot ASCII file format.

RTE solvers:	– Integration of the RTE along lines-of-sight using a RT technique – FVM (both in space and direction, cell-centred, explicit in each direction with global iterations to take account of scattering and/or nonblack wall effects)
Discretization scheme for FVM:	Step (upwind)
Interpolation schemes:	– Nearest-neighbour vertex – Simple averaging over neighbouring vertices – IDW
Algorithms:[2]	– Mesh bypass – Coordinate descent
Radiative species:	H_2O, CO_2, CO, CH_4
Particles:	Soot (nongray)
Spectral models:	– WLA – SNB (Goody, Malkmus, NASA SLG) – CK – Gray narrow-band (CKG, SNBG)
Medium inhomogeneity effects:	– CGA (for SNB) – Correlated-k approximation (for CK)
SNB parameters data sets:	– NASA 1973 – EM2C 1997 – ONERA 2007/2012 – EM2C 2012
Species mixing:	Uncorrelated narrow-band mixing model due to Modest and Riazzi (for CK)
CK method support:	SRCS (The Pennsylvania State University, 2008) Note: The source code of SRCS is written in Fortran; that is, to call SRCS routines from JERAD, a C/C++ wrapper function interface has been developed using concepts of mixed-language programming. In addition, the original SRCS code has been modified to provide a more efficient use in conjunction with JERAD

[2]Techniques that are employed when discretizing LOS.